Toward a fundamental understanding of scalar iso-surface kinematics in turbulent flows

Brandon Blakeley

A dissertation
submitted in partial fulfillment of the
requirements for the degree of

Doctor of Philosophy

University of Washington

2022

Reading Committee:

James Riley, Chair

Duane Storti, Chair

Alberto Aliseda

Program Authorized to Offer Degree:
Mechanical Engineering

University of Washington

Abstract

Toward a fundamental understanding of scalar iso-surface kinematics in turbulent flows

Brandon Blakeley

Co-Chairs of the Supervisory Committee:
James Riley
Mechanical Engineering

Duane Storti
Mechanical Engineering

Understanding the behavior of scalar iso-surfaces in turbulent flows is of particular interest for many problems in turbulent mixing that contain sharp interfaces between regions of the flow. Common examples include combustion, where the chemical reactions occur in thin regions within the flow, and the turbulent/non-turbulent interface in shear flows, where a thin region separates the rotational, turbulent motions from the irrotational, non-turbulent background. These interfaces can be described by an iso-surface of a scalar field, e.g., the flame surface is defined by an iso-value of a progress variable (usually temperature or species concentration) in premixed combustion, the stoichiometric value of the mixture fraction in non-premixed combustion, and the turbulent/non-turbulent interface is defined by a suitably 'small' value of the vorticity magnitude. Experimental and computational limitations have previously made investigations of iso-surface kinematics difficult to quantify, but recent advances in computing power and numerical algorithms allow for in-depth diagnostics of iso-surfaces interacting with three-dimensional, turbulent velocity fields.

This dissertation is comprised of a series of studies focused on gaining a deeper, fundamental understanding of the kinematics of iso-surfaces, with the intent that the

results can be applied and extended to a wide range of turbulent mixing problems in the field. First, direct numerical simulations of two differently initialized scalar fields evolving in homogeneous, isotropic turbulence are discussed, in which the iso-surface area density Σ and the terms in the evolution equation of Σ are evaluated as a function of time for a wide range of iso-values. In particular, the terms governing production of Σ, related to the fluid strain-rate, and destruction, related to the surface curvature and molecular diffusion, are considered. It is found that, because the fluid strain-rate is constant for both scalar fields, the production term behaves similarly for the two different scalar fields, but the behavior of the destruction term depends significantly on the initial condition of the scalar field.

In the following chapters, the iso-surface area density and the terms in its evolution equation are considered for a passive scalar field in the direct numerical simulation of a turbulent, temporally developing mixing layer. A novel approach has been taken to calculate surface averages as a function of the cross-stream direction, which allows for a more nuanced understanding of how iso-surface area is produced, destroyed, and transported (via turbulent and molecular diffusion) within the turbulent flow. A notable finding is that the profiles of Σ develop in a self-similar manner when scaled by the Taylor scale of the scalar field, λ_ϕ. Remarkably, the scaling appears to hold for a wide range of iso-values. A rough scaling argument based on the formal definition of Σ and properties of a temporal mixing layer is presented which also exposes a dependence on λ_ϕ. Based on these results, a possible scaling for the iso-surface area is presented as $A_{\text{iso}}/A_0 \sim (ReSc)^{1/2}$, where Re and Sc are local Reynolds and Schmidt numbers, respectively.

The terms in the evolution equation for Σ are also found to evolve in a self-similar manner, although there are significant differences in the scalings between several of the terms. Based on data from the direct numerical simulations, it is suggested that

the rate of change of Σ and the turbulent flux terms scale with $h\lambda_\phi/\Delta U$, where h is the width of the mixing layer and ΔU is the velocity difference across the mixing layer. In contrast, the production and destruction terms are found to scale with an additional factor of $(ReSc)^{1/2}$ compared to $\partial\Sigma/\partial t$, which is easily observed in previous studies as a significant discrepancy in the magnitude of the production and destruction terms compared to $\partial\Sigma/\partial t$ [36, 8, 46]. Importantly, the net effect of the production and destruction terms, sometimes referred to as net surface 'stretch' [11], is found to scale with $\partial\Sigma/\partial t$. The molecular diffusion term is found to scale with a factor of $(ReSc)^{-1/2}$ compared to $\partial\Sigma/\partial t$, which suggests that molecular diffusion is negligible for $ReSc \gg 1$.

TABLE OF CONTENTS

LIST OF FIGURES

LIST OF TABLES

ACKNOWLEDGMENTS

When I began this journey towards a PhD, I found it all too easy to focus simply on the end result of a study, without considering the inherent individuality that exists behind each and every scientific discovery and publication. I am extremely grateful to my advisor, Jim Riley, for helping me understand not only the technical side of my project, but also the uniquely *human* aspect of science. I would also like to thank him for his unwavering commitment and dedication to meet with me every single week during an unprecedented global pandemic.

I am also very grateful to Alberto Aliseda for adopting me into his laboratory group and his mentorship throughout my years at UW. I am looking forward to catching up at the APS conference each year. Duane Storti was a key figure during the early years of my PhD, and I am grateful for our many ad-hoc, after hours discussions about iso-surfaces and for his guidance on my project.

I was incredibly fortunate to share not only an office with Brad Perfect, but also a strong frienship and many adventures during my PhD. I am looking forward to many more adventures in the future! I would also like to thank each of my adopted labmates for their comraderie and support throughout the years; Arshiya, Mike, Alicia, Kurt, Laurel, Angela, Sari and Marissa. A huge thanks to Nathanael Machicoane, who has been an office partner, friend, and committee member, and hopefully soon a collaborator.

Finally, it goes without saying that I would not be where I am today without the support of my wife and family. I would like to thank my incredible wife, Dr. Darrian Bugg, who stood by my side throughout the ups and down of the PhD. And I would

like to thank my brother and my parents for their unwavering confidence in me.

I had an incredible opportunity to collaborate with Lawrence Livermore National Laboratory for my research, and I am grateful to my mentors Bill Cabot, Britton Olson, and Andy Cook for their mentorship and guidance on the project. I would also like to thank Perry Chodash and Kim Rivera for managing the internship and fellowship opportunities. Lawrence Livermore National Laboratory is operated by Lawrence Livermore National Security, LLC, for the U.S. Department of Energy, National Nuclear Security Administration under Contract DE-AC52-07NA27344.

DEDICATION

To Nirni.

Chapter 1

INTRODUCTION

1.1 Turbulent mixing

Turbulent mixing is ubiquitous in both the natural and engineered environments, from pollutants in the atmosphere, to the reaction of fuel and oxidizer in an internal combustion engine, or to the growth and development of a turbulent region of fluid in a jet or wake. A defining characteristic of turbulent flows is a significantly increased rate of mixing compared to laminar flows. This is true both for simple systems, such as turbulence hastening the mixing of cream into coffee, and extremely complex systems, such as the increased rate of vertical mixing in the abyssal ocean from the turbulent wake of flow past seamounts [69]. Engineers utilize this increased rate of mixing by inducing turbulence into a variety of systems, such as inside engines to accelerate the rate of chemical reactions, in heating and cooling applications to increase the rate of heat transfer, or inside the boundary layer of an aircraft wing which mixes momentum into the low velocity region and delays flow separation. In some cases, however, this increased rate of mixing is undesirable. For example, turbulent mixing due to the Rayleigh-Taylor instability is thought to be responsible for fuel quenching during inertial confinement fusion (ICF) experiments at the National Ignition Facility (NIF) [77]. Whether or not the turbulent mixing is advantageous or deleterious to system performance, it is crucial to understand and control the rate of mixing in a wide variety of applications.

The dynamics of turbulent mixing are typically considered in terms of the interaction between a turbulent velocity field and a scalar field. In the most simple case, there is a one-way coupling between the velocity and scalar fields, which might be called

'level 1' mixing [27], exemplified by a streak of dye mixing in water. In this relatively simple scenario, the dynamics of the dye concentration are determined exclusively by the turbulent velocity field, and the concentration of the dye has no bearing on the velocity field. In 'level 2' mixing, there is a two-way coupling between the scalar field and the turbulent velocity field. For example, when fluids with two different densities mix, the turbulent velocity field will dictate the scalar mixing, but the local variation in density will subsequently affect the turbulent flow field. The most complicated form of mixing is 'level 3', which is when the result of mixing modifies physical properties in the fluid. The best example of level 3 mixing is turbulent combustion, where the turbulent velocity field acts to mix oxidizer and fluid together, resulting in a chemical reaction that releases heat and subsequently changes the physical properties of the fluid near the reaction zone. For example, a candle flame simultaneously sustains and is sustained by mixing; buoyant, hot air produced from the combustion reaction rises from the flame, causing fresh air to mix with the fuel and release additional heat, causing the hot products to rise and entrain fresh air, and so on (or until all of the fuel is consumed).

In this work, only the first level of mixing will be considered, though it will be seen that there is no lack of complexity and nuance in even the most 'simple' case. The earliest proposals of this dissertation intended to examine a flow with variable density and heat release due to chemical reactions, but it was quickly discovered that there were already too many open questions in the literature, and a thorough examination necessitated a return to the fundamentals.

1.2 Interfaces in turbulence

Many turbulent mixing problems can be characterized by a sharp interface separating two regions of flow, e.g., the flame surface in both premixed and non-premixed flames, which separates fresh from burnt fuel (premixed) and fuel from oxidizer (non-premixed), or the turbulent/non-turbulent (T/NT) interface which separates turbu-

lent, rotational flow from the irrotational, quiescent background in turbulent shear flows. An important similarity between these seemingly disparate problems is that the interface can be described by an iso-surface of a scalar field. For example, the flame surface in premixed combustion can be described by an iso-surface of a progress variable (typically temperature or species mass fraction) coinciding with the peak reaction rate [11], while the flame surface in a non-premixed reaction is typically described by an iso-surface of the mixture fraction corresponding to the stoichiometric mixture of fuel and oxidizer [70]. Moreover, the T/NT interface can be typically demarcated by a 'small' value of the vorticity magnitude [23].

This abstraction allows for a more fundamental investigation of scalar iso-surface behavior in turbulent flows. The geometry of such scalar interfaces are known to be extremely complex and composed from a wide range of scales. Indeed, the passive scalar interface was found to exhibit fractal-like behavior, with a fractal dimension of $\approx$2.35 [86, 75, 76]. Fractal scaling was observed in these studies all the way from the largest (integral) scales to the smallest (Kolmogorov) scales of the flow [87]. These small-scale structures can be directly linked to the interaction of the scalar field and the fluid strain-rate [34], demonstrating the effect of turbulence on the interface structure. Both experimental and simulation data suggest that the predominant small-scale geometry of scalar iso-surfaces are flat, sheet-like surfaces with localized regions of high curvature [100, 29]. Interface geometry is also strongly affected by the diffusivity of the scalar field (more precisely, the ratio of the scalar diffusivity to momentum diffusivity, such as the Schmidt or Prandtl numbers). Decreasing diffusivity of the scalar is associated with an increase in interfacial area between the mixed and un-mixed fluid [82, 64].

Along with previous investigations into passive scalar iso-surfaces, there have been a number of studies exploring the turbulent/non-turbulent interface in particular. As briefly mentioned above, the turbulent/non-turbulent interface is a thin region of fluid present in many common shear flows such as jets, wakes, mixing layers and

boundary layers that separates turbulent (rotational) fluid from ambient (irrotational) fluid. The existence of a sharp boundary between turbulent and non-turbulent fluid was first postulated by Corrsin and Kistler after noting that velocity measurements near the boundary of a turbulent jet alternated sharply between laminar and fully turbulent [21, 22]. This interface was numerically and experimentally confirmed by a number of researchers, noting a steep change in velocity and vorticity between the turbulent and non-turbulent regions of the flow [6, 106, 37, 24]. Because of the steep change in vorticity between the turbulent and non-turbulent regions, the T/NT interface is typically identified by an iso-surface of the vorticity magnitude. In reality, the T/NT interface has finite thickness, on the order of the Kolmogorov lengthscale [89, 84, 38, 96]. The T/NT interface is stretched and distorted by a wide range of length scales in the flow [23, 59], which results in fractal-like behavior similar to the passive scalar iso-surfaces above, with a fractal dimension between 2.3 and 2.4 [26]. More recently, researchers have examined how the interface thickness scales with Reynolds number [84], investigated the role of coherent structures on interface properties [60], and expanded the T/NT interface analysis to stratified [104] and compressible [112, 40] flows.

The flame surface has likewise received a significant amount of attention by researchers. In premixed combustion, the flame surface is typically identified by an iso-surface of the reaction progress variable, c, which takes on a value of 0 in the fresh gases and 1 in the burnt gases [71]. The definition of the progress variable depends somewhat on the chemical reaction mechanism used, although it often takes the form of a reduced temperature or species mass fraction [71]. This formulation differs from the simplest case of dye mixing in water, where the propagation of an iso-surface (relative to the velocity field) is related only to the diffusion of the scalar. Instead, flame surface propagation is inherently related to the rate of chemical reaction (at first approximation, the laminar flame speed [98]). Furthermore, variable density due to heat release from chemical reactions provides additional complexity. A number of studies

have examined the structure [80, 102] and topology [101, 28] of the flame surface in premixed combustion. Of particular interest are the DNS results from Dopazo et al., who demonstrate that the chemical reaction term affects both the propagation of an iso-surface as well as the interaction of that iso-surface with the fluid strain-rate, even for constant-density flows [28]. Significant focus has been placed on understanding how flame characteristics, such as curvature and propagation velocity, are affected by turbulence intensity [43], differential diffusion [15], and detailed chemistry [81, 44], among others.

While the above studies of the T/NT interface and premixed flame surface have been instrumental in gaining a better understanding of the internal structure and general behavior of these phenomena, very little is known about the temporal and spatial evolution of these interfaces. In particular, established techniques of studying the T/NT interface rely on surface normal averaging, which allows flow statistics to be computed in a line that is normal to the surface [6]. However, it appears that the majority of studies utilizing this technique (to the authors' knowledge) focus on a single, instantaneous snapshot of a shear flow, which are at all times developing in time and/or space. Of the numerical studies that have examined the premixed flame surface, a significant portion utilize a freely propagating flame in homogeneous turbulence. In combination with a common simplification known as the 'generalized' flame surface density, in which the flame statistics are integrated over a wide range of iso-values [9], the statistics of the flame surface necessarily become independent of time and space. There has only been a single study, to the authors' knowledge, that has presented both the spatial and temporal variation of the flame surface density [48]. In this study of spherically expanding premixed flames, the iso-surface area per unit volume of the iso-level $c = 0.8$ is plotted as a function of the radial direction and at several instances in time. This study demonstrates that the iso-surface area density of a single (infinitesimally thin) iso-level is actually distributed over a finite region of physical space, and that this distribution is expected to vary in time and

space, depending on the flow conditions.

The spatial and temporal variation of these interfaces are directly related to important quantities for engineering design and optimization. For instance, knowledge of the flame surface area allows the net fuel consumption to be computed [56]. Similarly, the entrainment rate of ambient fluid into the turbulent core of a jet or wake is proportional to the surface area of the T/NT interface [107, 87]. Clearly, a fundamental understanding of the kinematics of iso-surfaces embedded in turbulent flows is needed to properly characterize such systems with dynamic sources and sinks of iso-surface area. With proper characterization, it may be possible to improve predictive models of these interfacial systems. Recent efforts to quantify the evolution of these interfaces will be reviewed in the following section.

1.3 Quantifying iso-surface evolution

The coherent flame model, first postulated by Marble and Broadwell [56] in 1977, suggested that the mean reaction rate of a non-premixed flame is proportional to the product of the mean flame surface density and the local reaction rate per unit area (provided sufficiently high levels of turbulence) [71]:

$$\langle \dot{\omega}_k \rangle = \left\langle \dot{\Omega}_k(\chi_{st}) \right\rangle \Sigma. \tag{1.1}$$

This assumption greatly simplifies the problem of combustion by effectively separating the effects of turbulence, which is assumed to affect only the surface area of the flame (encapsulated by the surface area density Σ), from the effects of chemistry that govern the local burning rate (which is given by the local reaction rate per unit flame area $\left\langle \dot{\Omega}_k \right\rangle$). In addition to this hypothesis, Marble and Broadwell also proposed an evolution equation for the rate of change of the flame surface density based on phenomenological arguments, which was used to model interactions between the flame surface and turbulence. Following studies proposed exact formulations for Σ and its transport equation for arbitrary surfaces in turbulence [72], as well as

premixed flames [93, 92] and non-premixed flames [95, 94]. Interestingly, there is a strong mathematical relationship between the surface area of a level set (i.e., flame surface area) and the probability distribution of the scalar and its gradient [11, 45, 97]. Although the surface area density formalism was initially conceived for infinitesimally thin, coherent flames, the subsequent transport equation for the surface area of an iso-level of a scalar field is exact and does not require a coherent flame to be valid. Note, however, that real flames have a finite thickness in which the chemical reactions occur, whereas an iso-level of a scalar field is infinitesimally thin.

Early studies of the iso-surface area density established that the rate of surface area production is driven by the tangential strain-rate [33] and the preferential alignment of the scalar gradient with the most compressive eigenvector of the strain-rate tensor [2], provided the rate of heat release (and flow dilatation) is small [43]. The rate of surface area destruction was found to be due to the combined effects of the curvature and the propagation velocity of the surface; for passive scalars, the propagation velocity is due to molecular diffusion [34], whereas the propagation of a premixed flame is strongly influenced by chemical reactions [98]. The statistical behavior of the surface curvature and propagation term has received significant attention [13, 14]. Recent results from [28] suggest that the propagation velocity of the iso-surface affects both the destruction and the production terms, making the effect of chemical reactions on iso-surface transport difficult to isolate.

Studies on iso-surface area density transport equation provide valuable information regarding the spatial and temporal evolution of the individual terms. For instance, Han and Huh [36] examined a premixed flame evolving in homogeneous, decaying turbulence. Here, the temporal evolution of the flame surface area, as well as the production and destruction terms of the surface transport equation, were presented for a range of Lewis numbers. Blakeley *et al.* [8] performed a similar analysis for a passive scalar field evolving in decaying, isotropic turbulence. In this study, the evolution of iso-surface area and the transport terms were compared for two different

initial scalar distributions. Recently, a couple of studies examined the variation of flame surface area and transport along the axis of a premixed jet flame [102, 54]. One of the key findings that is consistent throughout these studies is that the net effect of the terms governing iso-surface production and destruction is significantly smaller in magnitude than both the production and destruction terms individually.

In a recent study of spherically expanding premixed flames, Kulkarni *et al.* [46] examined the transport of the peak value of Σ for several different Reynolds numbers, which is determined by a flux from the mean and turbulent velocities in addition to the net surface stretch. The results of this study suggest that the transport from the mean velocity field scales with the pressure rise in the flame, the transport from the turbulent flux scales with the integral scale of the turbulent velocity field, ℓ, and that the net surface stretch scales with the Kolmogorov scale, η.

1.4 Mathematical formulation of iso-surface transport

From the preceding discussion, it is clear that understanding how iso-surface area density is produced, destroyed, and transported in a turbulent flow is an important part of quantifying, and ultimately predicting, these interfacial systems. In this section, the mathematical description of iso-surfaces will be examined, including a discussion of iso-surface area density, Σ, and its evolution equation.

Consider the simplest case of mixing for a passive, conserved scalar field, $\Phi(x, y, z, t)$, that satisfies the advection-diffusion equation, given by equation (2.12). An iso-surface of Φ is defined by a two-dimensional surface on which the value of Φ is equal to a constant value, Φ_{iso}. This iso-surface is defined by a normal vector, n_i,

$$n_i = -\frac{1}{|\nabla\Phi|}\frac{\partial\Phi}{\partial x_i}, \tag{1.2}$$

and a diffusion velocity, w_{iso},

$$w_{\text{iso}} = \frac{D}{|\nabla\Phi|}\frac{\partial^2\Phi}{\partial x_i x_i}, \tag{1.3}$$

in the direction normal to the iso-surface, where D is the molecular diffusivity and summation is implied on repeated indices. The magnitude of the gradient of the scalar is given by

$$|\nabla\Phi| = \left(\frac{\partial\Phi}{\partial x_i}\frac{\partial\Phi}{\partial x_i}\right)^{1/2}. \tag{1.4}$$

The diffusion velocity refers to the propagation speed of an iso-surface normal to itself, relative to the surrounding fluid velocity. For a conserved scalar such as the mixture fraction in non-premixed combustion, the diffusion speed of an iso-surface is determined, in particular, by molecular diffusion (see figure 1.1 for the one-dimensional interpretation of the diffusion velocity). When chemical reactions are present in a premixed reaction, the diffusion speed will include, in addition, a reaction source term due to the chemical reaction.

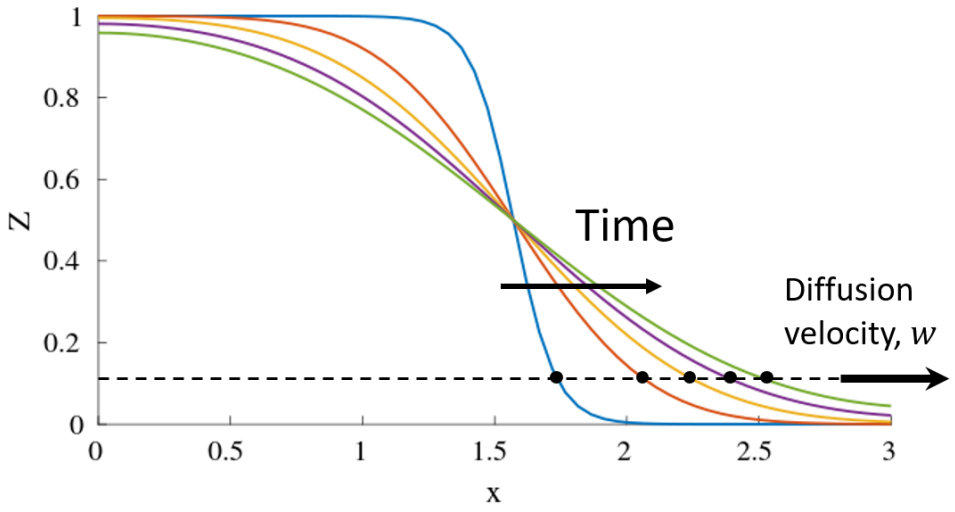

Figure 1.1: One-dimensional interpretation of the diffusion velocity. As molecular diffusion smooths gradients, position of the iso-Z levels will move in the x direction.

In addition to n_i and w_{iso}, The mean curvature of an iso-surface, H, is related to the surface normal vector through its divergence,

$$\frac{1}{2}\frac{\partial n_i}{\partial x_i} = \frac{1}{2}(\kappa_1 + \kappa_2) = H, \tag{1.5}$$

where κ_1 and κ_2 are the principal curvatures of the iso-surface. For convenience, $\partial n_i/\partial x_i$ will be referred to broadly as the surface curvature, noting that it is proportional to the mean curvature of the surface (and is also closely related to the Gaussian curvature). In this definition, an iso-surface has positive curvature if it is concave towards the 'oxidizer' ($Z = 0$) and negative curvature if it is concave towards the 'fuel' ($Z = 1$). A diagram of a representative iso-surface of a passive scalar field is shown in Figure 1.2.

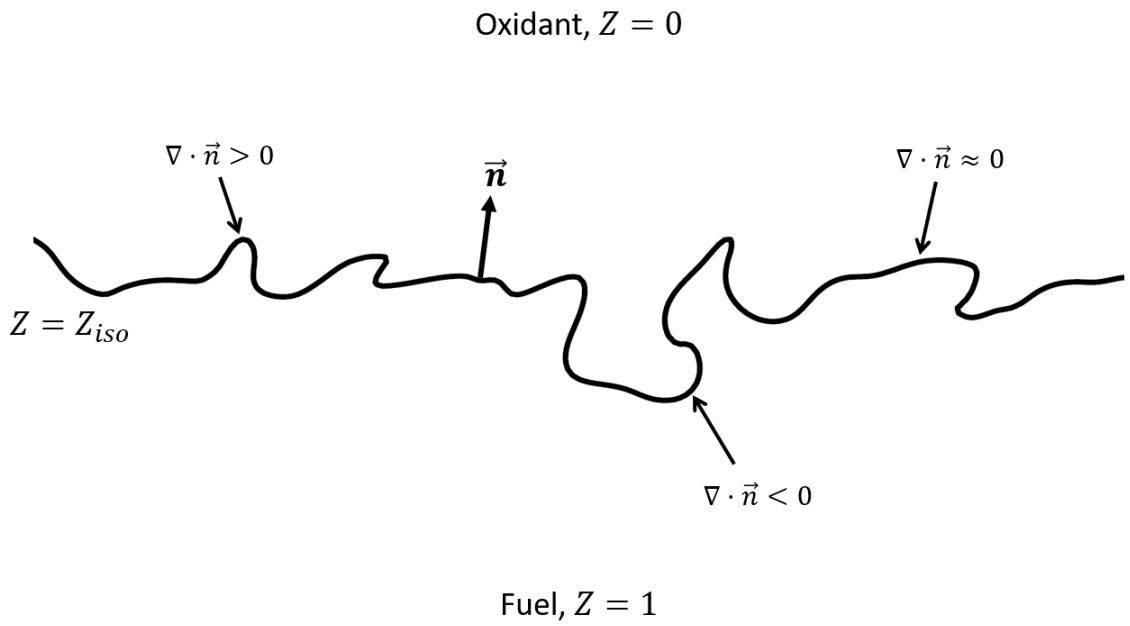

Figure 1.2: Diagram of iso-surface properties. The unit normal vector is defined as positive towards $Z = 0$. Surface mean curvature is positive (negative) when the surface is convex towards the fuel (oxidizer).

The area of an iso-surface is defined by [72] as

$$A_{\text{iso}} = \int_{\mathcal{V}} \Sigma' \mathrm{d}\mathcal{V}, \tag{1.6}$$

where $\mathcal{V}$ is an arbitrary volume and Σ' is the iso-surface area density (sometimes

called the *fine-grained* surface area density [97]),

$$\Sigma' = |\nabla\Phi|\delta(\Phi - \Phi_{\text{iso}}). \tag{1.7}$$

Here, Φ_{iso} is the iso-value of Φ pertaining to the surface, and $\delta()$ is the Dirac delta function [97, 71]. The mean iso-surface area density, Σ, is defined as

$$\Sigma = \langle|\nabla\Phi|\delta(\Phi - \Phi_{\text{iso}})\rangle = \left\langle|\nabla\Phi|\middle|\Phi = \Phi_{\text{iso}}\right\rangle \mathcal{P}_{\Phi_{\text{iso}}}, \tag{1.8}$$

where $\langle\cdot\rangle$ denotes a probability average, $\langle Q|Q'\rangle$ represents the average of quantity Q conditioned on Q', and $\mathcal{P}_{\Phi_{\text{iso}}}$ is the value of the probability density function of Φ corresponding to $\Phi = \Phi_{\text{iso}}$.

Based on (1.8), a transport equation for the mean surface area density Σ can be derived [93, 94],

$$\frac{\partial\Sigma}{\partial t} + \underbrace{\frac{\partial}{\partial x_i}\left(\langle U_i\rangle_s \Sigma\right)}_{\mathcal{T}_U} = \underbrace{\left\langle \frac{\partial U_i}{\partial x_i} - n_i n_j \frac{\partial U_i}{\partial x_j}\right\rangle_s \Sigma}_{\mathcal{P}} + \underbrace{\frac{\partial}{\partial x_i}\left(\langle w_{\text{iso}} n_i\rangle_s \Sigma\right)}_{\mathcal{T}_D} + \underbrace{\left\langle w_{\text{iso}} \frac{\partial n_i}{\partial x_i}\right\rangle_s \Sigma}_{\mathcal{D}}. \tag{1.9}$$

The operator $\langle\cdot\rangle_s$ refers to a surface average, defined for an arbitrary property $Q(x, y, z, t)$ by

$$\langle Q\rangle_s = \frac{\langle Q\Sigma'\rangle}{\Sigma}. \tag{1.10}$$

The terms in (1.9) have been labeled and refer, in order, to the rate of change of the mean surface area density, turbulent convective flux of Σ, $\mathcal{T}_U$, rate of production of Σ due to the fluid strain-rate, $\mathcal{P}$, flux of Σ due to molecular diffusion, $\mathcal{T}_D$, and the rate of destruction of Σ due to the combined effects of molecular diffusion and surface curvature, $\mathcal{D}$. Note that although this formulation assumes a passive scalar field that propagates via molecular diffusion, the effects of an active scalar field, such as a premixed flame surface, can be accounted for by including an additional chemical reaction term in (1.3).

1.5 Research Objectives

The focus of the present work is on a fundamental understanding of iso-surface behavior in turbulent flows, of which few studies exist. Despite the popularity of flame surface modeling in turbulent combustion, the models are primarily developed using statistically planar, freely propagating flames with detailed chemistry that experience relatively moderate levels of turbulence. While these studies clearly have considerable value in the combustion modeling community, they are not necessarily translatable to other interfaces, e.g., the turbulent/non-turbulent interface. Furthermore, the additional complexity of the chemical reactions makes it difficult to separate the effects of molecular diffusion from chemistry on the curvature, propagation, and even strain-rate terms [28].

In this author's opinion, a return to the fundamentals is warranted. Without a firm grasp on the essential behavior of iso-surfaces in turbulence, it will be difficult to interpret the effects that arise from physically realistic scenarios of, e.g., premixed flames. With the continued improvement of high-performance computing hardware and software, more realistic simulations of turbulence are possible than ever before, which give an unparalleled amount of insight into the dynamics of the flow. Coupled with the iso-surface integration methodology described herein, there is opportunity to expand our fundamental understanding of how iso-scalar surfaces evolve in time and space in turbulent flows and the mechanisms responsible for producing, destroying, and transporting them. To this end, a primary objective of this thesis is to quantify, in exhaustive detail, the evolution of passive scalar iso-surfaces in turbulence.

In the following dissertation, the temporal and spatial evolution of iso-surfaces are presented, based on results from direct numerical simulation of passive scalar fields evolving in turbulent flows. Two separate flows are considered, the first of which is decaying homogeneous, isotropic turbulence (HIT) in a periodic cube, in which the evolution of two distinct scalar fields are examined; one is distributed

homogeneously throughout the domain, whereas the other is initially planar. The second flow described herein is of a turbulent, temporally developing mixing layer, with an initial passive scalar field that coincides with the mean velocity field. The two flows were simulated using two different numerical codes and methods, which will be presented in Chapter 2, including a discussion of the numerical methods, computational resources, and validation of the results compared to previous studies. In Chapter 3, the temporal evolution of the iso-surface area density in HIT, for a wide range of iso-values of the passive scalar field, will be presented. Chapters 4 and 5 will present the results from the turbulent mixing layer, including the self-similar behavior of Σ and each of the terms in its transport equation. Finally, Chapter 6 will summarize the key results from this work and propose directions for future research.

Chapter 2

COMPUTATIONAL METHODS

Based on the above discussion, it can be seen that an investigation of the spatial and temporal development of an iso-surface embedded in a turbulent flow field is an important step toward understanding the behavior of a broad class of turbulent mixing problems. Unfortunately, experimental measurement of iso-surfaces in turbulent flows is both difficult and expensive. Advances in experimental technology have allowed for impressive measurements of both the T/NT interface and flame surface, such as recent experiments by [3] and [85]. However, even state of the art experiments typically measure only two-dimensional statistics, which cannot recover the fully three-dimensional behavior of iso-surfaces embedded in a turbulent flow [102]. Direct numerical simulation (DNS), on the other hand, coupled with recent advances in computing power and numerical algorithms, allow for in-depth investigation into high-resolution, three-dimensional velocity and scalar fields. Despite being restricted to relatively simple geometries, DNS is a valuable tool for studying fundamental properties of turbulence.

DNS has become a common tool for studying turbulent flows due to the unparalleled amount of information produced by the simulation [74]. As the name implies, direct numerical simulation numerically solves the governing equations for fluid flow for all scales of flow, from the largest energy containing motions down to the smallest length scales, where turbulent kinetic energy is dissipated into heat by molecular viscosity. Although DNS provides a huge amount of information about the turbulent flow, the computational cost of simulating even simple flows is extreme, and requires the use of high-performance computing (HPC) facilities. In contrast, a Reynolds-

Averaged Navier-Stokes (RANS) simulation or Large Eddy Simulation (LES) are less computationally demanding, but introduce unclosed terms that must be approximated by various turbulence models.

The following chapter will introduce the numerical methods and computational resources utilized in this work. In § 2.1, the methodology of the DNS of decaying, homogeneous isotropic turbulent will be presented, including a discussion of the two distinct scalar fields that are simulated along with the turbulent velocity field. The methodology of the second DNS will be presented in §§ 2.2 and 2.3, which will give a brief overview of the 'Miranda' code, developed by Andy Cook at Lawrence Livermore National Laboratory (LLNL) [18], and also some mixing layer results compared to previous studies used to validate the code. Finally, the chapter will conclude in § 2.4 with an examination of the algorithm used to extract iso-surface quantities, such as surface area, from the implicit scalar fields that are generated via DNS.

2.1 DNS of homogeneous, isotropic turbulence

The DNS data presented in Chapter 3 was simulated on the Amazon Web Services Elastic Compute Cloud (AWS EC2) platform, using an in-house code designed to operate exclusively on graphics processing units (GPUs). The work was funded by the AWS Cloud Credits for Research program as an effort to study the feasibility of performing DNS on cloud-based GPU resources. This section will describe the approach to numerical integration of the governing equations, present initial parameters of the DNS, and discuss algorithm development for use on cloud-based GPUs.

2.1.1 Numerical methods

The fluid motion is assumed to satisfy the incompressible form of the Navier-Stokes equations and, for this study, these equations are solved in the following form:

$$\frac{\partial \mathbf{u}}{\partial t} = -\nabla\left(P - \frac{|\mathbf{u}|^2}{2}\right) - \boldsymbol{\omega} \times \mathbf{u} + \frac{1}{\mathrm{Re}}\nabla^2\mathbf{u}, \tag{2.1}$$

and

$$\nabla \cdot \mathbf{u} = 0, \tag{2.2}$$

where P is the dynamic pressure, $\boldsymbol{\omega}$ is the vorticity vector $\nabla \times \mathbf{u}$, and Re is the Reynolds number. Equation 2.1 is non-dimensionalized by the initial values of the rms velocity $u'(t=0)$ and the integral length scale $\ell(t=0)$, such that the turbulent Reynolds number is defined as $\mathrm{Re} = u'\ell/\nu$, with ν as the (constant) kinematic viscosity of the fluid. The advective (integral) time scale $t_{\mathrm{adv}} = \ell/u'$ is also used in the non-dimensionalization. In addition to the momentum balance and the conservation of mass, the advection-diffusion equation is solved for a conserved passive scalar, Z:

$$\frac{\partial Z}{\partial t} + \mathbf{u} \cdot \nabla Z = \frac{1}{\mathrm{Re}\,\mathrm{Sc}} \nabla^2 Z, \tag{2.3}$$

where $\mathrm{Sc} = \nu/D$ is the Schmidt number and D is the (constant) molecular diffusion coefficient of the scalar Z.

The above equations are solved directly in a cubic domain of length $L = 2\pi$ using a Fourier pseudo-spectral algorithm based on Canuto [12], with $N = 1024$ grid points in each direction. Boundary conditions are periodic in all three directions. A spherical filter of radius $(15/32)N$ is applied to the Fourier coefficients to remove the most egregious aliasing errors, while maximizing resolution [67]. To ensure that the smallest scales of the flow are adequately resolved, the product of the maximum wavenumber and the Kolmogorov lengthscale, $k_{\mathrm{max}}\eta_k$, is approximately 2 at the initial time [32, 25]. Here $\eta_k = (\nu^3/\epsilon)^{1/4}$, where ϵ is the kinetic energy dissipation rate. Time integration is performed in Fourier space (treating the viscous terms implicitly) using a second order Adams-Bashforth scheme with an initial Courant number of 0.043.

2.1.2 Simulation parameters

The velocity field is incompressible, homogeneous, and isotropic, with an initial Reynolds number based on the Taylor microscale, λ, of $Re_\lambda = u'\lambda/\nu = 140$. The velocity field is initialized in a multi-step procedure designed to roughly simulate

laboratory experiments of grid turbulence. First, Fourier coefficients are assigned randomly, following a typical laboratory energy spectrum. Once the coefficients are determined, the velocity field is allowed to evolve until a) all of the turbulent length scales increase and b) the velocity-derivative skewness settles near a value of -0.5. Once this has occurred, the energy spectrum is re-energized and allowed to evolve once again until both conditions a) and b) have been met and the velocity statistics have reached the desired values [57].

Two different initial conditions are explored for the passive scalar. In Case A, the scalar field is initialized according to the procedure outlined by Eswaran and Pope [31] to create initially isotropic 'blobs' distributed throughout the domain with integral length scale similar to that of the velocity field. This configuration is visualized in Figure 2.1a for the iso-surface $Z_{\text{iso}} = 0.5$. Case B is a planar configuration, defined by $Z = 0.5[1 + \tanh{(y - y_o)/h}]$, where h is the initial mixing layer width and y_o is used to shift the midpoint of the mixing layer to the center of the computational domain. The initial value of the mixing layer width is $h = 0.18\ell$, resulting in a steep gradient between the 'fuel' ($Z = 1$) and the 'oxidizer' ($Z = 0$). Because the domain is periodic, there are effectively two planar iso-surfaces present in the domain at the initial condition. This is visualized in Figure 2.1b for an iso-surface $Z_{\text{iso}} = 0.5$. Both of the passive scalar fields are defined such that $0 \leq Z \leq 1$.

Once the turbulent velocity field has been initialized, the scalar field is injected into the domain. This causes the scalar field to undergo a period of rapid adjustment at early times. This rapid adjustment to flow conditions does not necessarily represent a physical process of interest, and will be largely ignored in the following analysis. Both initial scalar fields were chosen to have a mean value $\overline{Z} = 0.5$ with a thin mixing layer between the fuel and oxidizer. Here the $\overline{(\cdot)}$ represents a probability average, which is approximated as a volume average from homogeneity. Because the scalar field is conserved, $\overline{Z}$ is invariant in time. The Schmidt number $Sc = \nu/D$ is set to a constant value of 0.7. Note that, because the scalar fields are passive, the

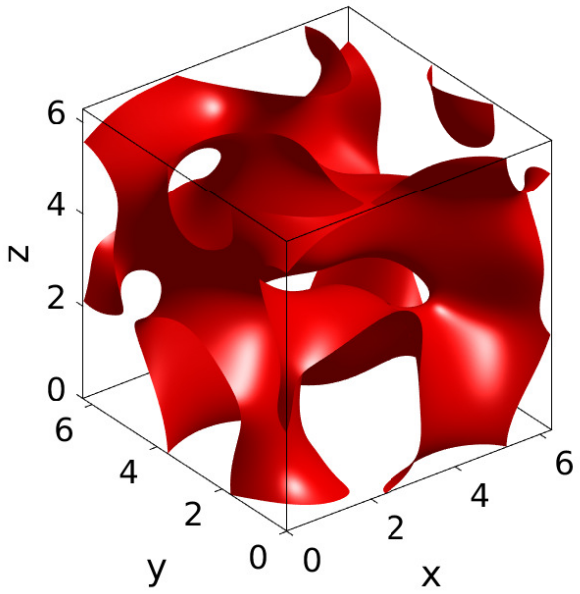

(a) Case A

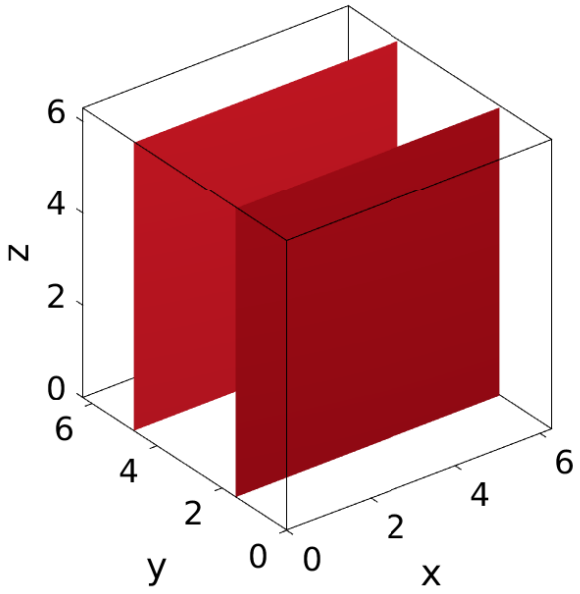

(b) Case B

Figure 2.1: Visualization of the iso-surface corresponding to $Z_{\text{iso}} = 0.5$ at $t = 0$ for the a) initially isotropic scalar field (Case A) and b) the initially planar scalar field (Case B).

N^3	Re_λ	u'	$k_{\max}\eta_k$	l	$\overline{Z}$	Sc
1024^3	140	0.8938	2.02	0.883	0.5	0.7

Table 2.1: Velocity and scalar field statistics for the DNS performed for this study.

velocity field statistics are identical for both scalar fields throughout the simulations; only the statistics of the scalar fields are different. Additional information regarding the initial velocity and scalar fields is given in Table 2.1.

2.1.3 DNS algorithm development

Due to the extremely high computational cost of simulating even simple flows with direct numerical simulation, high-performance computing on supercomputing clusters, such as those at DOE facilities (e.g. Summit at Oak Ridge or Sierra at Lawrence Livermore) and other government laboratories, has become commonplace. Recently, cloud computing services offered through commercial providers such as Amazon, Google, or Microsoft have been gaining attention as a potential alternative to traditional supercomputing facilities. One example in the fluid dynamics community is the work by Mesnard and Barba using Microsoft's cloud service, Azure, to simulate the dynamics of a flying snake on a total of 144 CPU cores and 24 GPUs [58].

Although some early forays into cloud computing demonstrated less than promising results, modern technology is rapidly improving and companies are constantly updating their services. A study by Zaspel and Griebel suggested that small- to medium-scale companies that would typically struggle to afford an HPC cluster have the most to benefit from cloud computing resources [111]. In particular, cloud computing may prove to be a tremendous benefit to small universities or independent researchers without access to a local HPC cluster.

Another relatively recent innovation in high-performance computing is the graph-

ics processing unit. For many years, GPUs were exclusively used in video technology to compute and display pixels on a screen. Since the public release of the CUDA language in 2007, which allows for direct programming of GPU kernels, researchers have been exploring the use of GPU's for scientific computing.

GPU technology is based around a massively parallel structure of central processors. In current technology, a central processing unit (CPU) has anywhere from 4 (home computer) to 40 (server) CPU cores, which are able to process tasks simultaneously. In contrast, a modern GPU will contain anywhere between 250 and 5,000 CUDA cores. In some ways, it is unfair to compare CUDA cores to regular CPU cores; CUDA cores have slower clock speeds compared to CPU cores and a smaller number of operations available to them. The primary benefit from GPU computing is the ability to perform a great deal of simple calculations in parallel, such that the speedup from running many jobs simultaneously offsets the slower clock speed of an individual core. GPUs are quickly being adopted by the high-performance computing community at large, including several researchers working in fluid dynamics [17, 113, 35, 68].

The program used for this simulations described above was was initially written in C, and then translated to CUDA (the proprietary language for interfacing with Nvidia's GPU hardware), first for single-GPU systems and then for systems with multiple GPUs connected to a single CPU. The simulation was performed on Amazon Web Services Elastic Compute Cloud (EC2) and utilized a single node that linked eight Nvidia V100 GPUs to a single CPU, with 256 GB of available RAM. The code was designed to store all of the variables required for the DNS on GPU memory, to reduce the latency experienced when transferring data from the CPU to GPU. However, this limits the RAM available to the simulation to 128 GB (16 GB $\times$ 8 GPUs). The data was distributed in a 'slab' formation, consisting of eight x, y slabs split in the z direction.

The Nvidia library 'cuFFT' was utilized for the Fast Fourier Transforms, which

is based on the widely used Fastest Fourier Transform in the West (FFTW). However, multi-GPU support was not widely available (at the time), and cuFFT required contiguous arrays on a single device to perform FFTs. This necessitated a two-part approach to the FFT, in which a two-dimensional FFT was performed on each GPU in the x, y directions, and then a matrix transpose operation would rearrange the slabs to allow for the final FFT in the z direction. To do this, a custom matrix transpose subroutine was required, which unfortunately is challenging to optimize for GPU architecture due to non-contiguous array structure. This caused the performance of the multi-GPU software to suffer significantly compared to the single-GPU version.

The simulations described in § 3 took approximately 58 hours to complete on the AWS EC2 nodes with eight Nvidia V100 GPUs. The on-demand price of these nodes is approximately \$24/hour. However, clever use of the SPOT market (essentially the AWS version of a backfill queue), allows users to bid for time when there are idle resources. This allowed the present simulations to be performed for less than a third of the on-demand price at \$7.20/hour. For the two realizations described here, the cost is approximately $\$1,420$ using on-demand resources, or approximately \$420 using the backfill queue. Note that the SPOT market fluctuates depending on user bids, and a value this low is not guaranteed.

Overall, the experience of building a custom program for direct numerical simulation was extremely beneficial, and working with CUDA allowed for a good understanding of GPU architecture and performance. However, in subsequent years the support for multi-GPU and high-performance computing has increased significantly, making many of the challenges discussed above obsolete. In the quickly-changing realm of software, the program described above is not sufficient. In addition, the recent availability of source transformation solutions, such as OpenMP and HIP, have reduced the utility of programming in CUDA. The benefit of source transformation is that high-perfomance codes, originally written for CPUs, can be (relatively) easily transferred to GPUs. While the transformation is not always as optimal as user-

written GPU code, the automatic process allows the program to be used on multiple architectures (CPU or GPU) without required forked or duplicated code.

2.2 DNS of a temporal mixing layer

For the DNS data presented in Chapters 4 and 5, a custom version of the code base Miranda is used. The software was developed at Lawrence Livermore National Laboratory (LLNL) and can perform both DNS and large eddy simulation (LES) in high energy density applications. Miranda has been validated extensively and used for several other novel research cases such as the Rayleigh-Taylor, Kelvin-Helmholtz and Richtmeyer-Meshkov instabilities [20, 63, 91]. The particular version utilized for this study is part of an ongoing effort to port Miranda to heterogeneous architectures, which contain both traditional CPUs as well as novel graphics processing units (GPUs).

This section will briefly outline the governing equations and numerical methods of Miranda and then present the simulation parameters and initial conditions used for this study. A brief discussion of the approach to porting the software to GPUs is included at the end. Additional information regarding the initial algorithm development and the 'artificial large eddy simulation' (AFLES) approach can be found in references [18, 19].

2.2.1 Governing equations

Miranda solves the three-dimensional, compressible Navier-Stokes equations:

$$\frac{\partial \rho}{\partial t} + \frac{\partial \rho U_i}{\partial x_i} = 0, \tag{2.4}$$

$$\frac{\partial \rho U_i}{\partial t} + \frac{\partial \rho U_i U_j}{\partial x_j} = -\frac{\partial P}{\partial x_i} + \frac{\partial \tau_{ij}}{\partial x_j}, \tag{2.5}$$

$$\frac{\partial E}{\partial t} + \frac{\partial (E+P) U_i}{\partial x_i} = \frac{\partial \tau_{ij} U_j}{\partial x_i} + \frac{\partial q_i}{\partial x_i}, \tag{2.6}$$

where ρ is the fluid density, U_i is the velocity, P is pressure, τ_{ij} is the viscous stress tensor, E is the total energy (internal plus kinetic), and q_i is the conductive heat flux. For a Newtonian fluid, invoking Stokes' hypothesis, the viscous stress tensor is given by

$$\tau_{ij} = 2\mu\left(S_{ij} - \frac{1}{3}\frac{\partial U_k}{\partial x_k}\delta_{ij}\right), \tag{2.7}$$

where δ_{ij} is the Kronecker delta, μ is the dynamic viscosity and S_{ij} is the strain-rate tensor [49]

$$S_{ij} = \frac{1}{2}\left(\frac{\partial U_i}{\partial x_j} + \frac{\partial U_j}{\partial x_i}\right). \tag{2.8}$$

The total energy E is given by

$$E = \rho(e + U_i U_i/2), \tag{2.9}$$

where e is the internal energy per unit mass, and the heat flux q_i is given by Fourier's Law

$$q_i = \kappa\frac{\partial T}{\partial x_i}, \tag{2.10}$$

with κ as the thermal conductivity. To close the above equations, the gases are assumed to be perfect, i.e., the ratio of specific heats $\gamma = c_p/c_v$ is constant and equal for all species such that

$$P = (\gamma - 1)\rho e. \tag{2.11}$$

Finally, the advection-diffusion equation is solved for a passive scalar Φ, with molecular diffusivity D,

$$\frac{\partial \rho\Phi}{\partial t} + \frac{\partial \rho\Phi U_i}{\partial x_i} = -\frac{\partial}{\partial x_i}\left(D\frac{\partial \rho\Phi}{\partial x_i}\right). \tag{2.12}$$

In subsequent sections, fluid velocities U_1, U_2, U_3 in the x_1, x_2, x_3 directions will be freely interchanged with U, V, W, which represents velocities in the x, y, z directions, respectively.

2.2.2 Numerical methods

Spatial derivatives in Miranda are estimated by a tenth order, compact finite difference scheme [51]. A five stage, fourth order, low storage Runge Kutta scheme is used for temporal integration of the governing equations [42]. The conserved variables are de-aliased each timestep with an eighth order compact filter designed to remove the top 10% of wavenumbers. An adaptive timestep is used to ensure numerical stability, determined by

$$\Delta t_{\mathrm{CFL}} = \min\left(\frac{|U|}{\Delta x} + \frac{|V|}{\Delta y} + \frac{|W|}{\Delta z} + c_s\left[\frac{1}{\Delta x^2} + \frac{1}{\Delta y^2} + \frac{1}{\Delta z^2}\right]^{1/2}\right)^{-1}, \tag{2.13}$$

where $c_s = (\gamma RT)^{-1/2}$ is the speed of sound in the fluid, and $\Delta x, \Delta y, \Delta z$ represents the grid spacing in the x, y, z directions. For the simulation results presented here, the CFL number is set to 0.95.

Miranda was designed to be used in either a DNS or LES configuration; if no physical fluid diffusivities, i.e., μ, κ, D, are defined, then a 'hyper-diffusivity' is included in the relevant equations of motion [18]. For the results presented here, the hyper-diffusivity has been disabled for all fluid properties, and constant parameters for μ, κ, and D have been defined explicitly (discussed in the following section).

2.2.3 Simulation parameters

A turbulent, planar, temporal mixing layer is simulated for this study, which is a useful tool for analyzing turbulence and mixing due to its relative simplicity, while also retaining many fundamental characteristics of turbulent mixing. As opposed to its spatial equivalent, the temporal mixing layer evolves in time, in which the mixed region of fluid grows outward towards the boundaries, ultimately in a self-similar manner. The computational domain is a rectangular prism that consists of $4096 \times 1536 \times 1024$ (6.4 billion) grid points in the x, y, z directions, respectively. The

lengths of each dimension, L_x, L_y, and L_z, are $1600\delta_0$, $600\delta_0$, and $400\delta_0$, respectively, where δ_0 is the momentum thickness of the mixing layer (defined in equation 2.24) at $t = 0$. Boundary conditions are periodicity in the streamwise (x) and spanwise (z) directions, with free-slip conditions at the top ($y = L_y/2$) and bottom ($y = -L_y/2$) boundaries, i.e., $V|_{y=L_y/2} = V|_{y=-L_y/2} = 0$, in addition to 0 gradients in y of horizontal velocities at these boundaries.

The computational domain used for the present study is displayed in figure 2.2, along with a snapshot of the passive scalar field at $t\Delta U/h_0 = 462$. The mixing width h_0 refers to the visual thickness of the velocity field, defined in equation (2.25), evaluated at the initial state, $t = 0$. The blue (dark) color represents $\Phi = 1$, and the white represents $\Phi = 0$. Arrows represent direction of the mean flow. The x, y plane shown is extracted at $z = 0$, with the positive z direction oriented out of the page.

The initial mean streamwise velocity, $\langle U_0 \rangle (y)$ is given by

$$\langle U_0 \rangle (y) = \frac{\Delta U}{2} \tanh\left(\frac{y}{2\delta_0}\right), \tag{2.14}$$

where the upper and lower stream velocities are given by U_+ and $U_- = -U_+$, and the velocity difference $\Delta U = U_+ - U_-$. Initial mean velocities in the cross-stream and spanwise directions are set to zero, where the mean and fluctuating velocities are given by the Reynolds decomposition (see § 2.3.1). The initial momentum thickness, δ_0, is 0.01.

Three-dimensional, homogeneous, isotropic velocity fluctuations are imposed on the initial mean velocity field. The fluctuating velocity field is initialized by randomly assigning Fourier coefficients based on a model kinetic energy spectrum

$$E_0(k) = k^4 \exp(-(k - k_p)^2/k_b^2), \tag{2.15}$$

where k corresponds to the wavenumber magnitude, and k_p and k_b are constants to adjust the peak and effective width of the energy spectrum in wavenumber space. For this study, $k_p = 4$ and $k_b = 1/\delta_0$. Further details of the velocity initialization

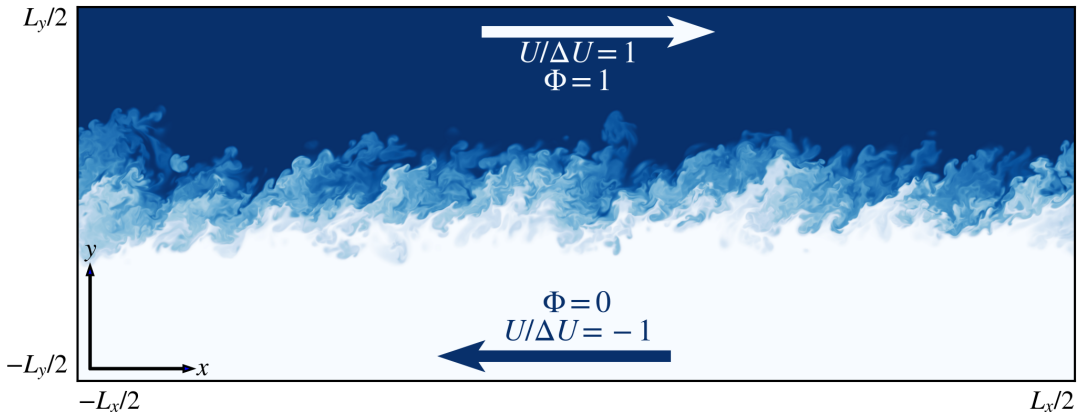

Figure 2.2: Simple two-dimensional schematic of the mixing layer configuration, showcasing a snapshot of the scalar field at $t\Delta U/h_0 = 462$, during the self-similar evolution. Dark blue represents a value of $\Phi = 1$ and white represents $\Phi = 0$.

procedure can be found in Ref. [57]. A spatial filter is applied to the resulting velocity fluctuations to confine the initial turbulent motions to be near the region of shear. The maximum value of the streamwise fluctuating velocity autocorrelation, $\langle uu \rangle$, at $t = 0$ is approximately $0.025\Delta U^2$, which is comparable to the magnitude of the velocity fluctuations during the self-similar evolution of the mixing layer. This relatively strong disturbance is used to facilitate a shortened transition period to achieve fully developed turbulent flow. The Reynolds number based on the initial momentum thickness is $Re_0 = \rho \Delta U \delta_0 / \mu = 120$. Details regarding the turbulent flow field during the shear layer evolution are provided in § 2.3.3.

The passive scalar field is initialized to coincide with the mean velocity field at $t = 0$,

$$\langle \Phi_0 \rangle (y) = \frac{1}{2} + \frac{1}{2} \tanh \left(\frac{y}{2\delta_0} \right), \tag{2.16}$$

where the upper stream takes on a value of $\Phi = 1$, the lower stream is $\Phi = 0$, and $\Delta\Phi = 1$. No fluctuations were imposed on the mean scalar concentration, rather it was allowed to evolve with the turbulent flow field. The Schmidt number of the passive scalar, $Sc = \nu / \rho D$, is set to a constant value of 0.7 for the simulation.

Although Miranda solves the equations of motion for a compressible fluid, the simulation reported here is carefully designed to simulate an effectively incompressible flow. Based on the speed of sound in the fluid, the convective Mach number, $\mathrm{Ma} = \Delta U / c_s$, is approximately 0.15. This is well under the accepted threshold of $\mathrm{Ma} = 0.3$, below which compressible effects on flow dynamics become negligible. To further verify that the flow is effectively incompressible, the root mean square (rms) of the velocity divergence is consistently found to be three orders of magnitude less than the tangential strain-rate throughout the simulation. This demonstrates that it is safe to neglect the effects of compressibility on the flow dynamics. In addition, a thermal conductivity must be specified for the fluid in order to close the governing equations. The Prandtl number, $Pr = c_p \mu / \kappa$ is set to a constant value of 0.7 to approximate atmospheric conditions. Despite the presence of thermal conduction in the governing

equations, temperature deviations throughout the flow are less than 0.2%, indicating that the flow is effectively isothermal and incompressible.

2.3 Validation of the temporal mixing layer

In this section, several canonical results from the temporal mixing layer simulation are presented and compared to previously published results; in particular these results come from the self-similar period of the mixing layer evolution.

2.3.1 Reynolds-averaged equations for a temporal mixing layer

Consider the turbulent flow field in a temporally developing shear layer with velocities $U(x,y,z,t)$, $V(x,y,z,t)$, $W(x,y,z,t)$ and passive scalar $\Phi(x,y,z,t)$. In this configuration, the flow is statistically homogeneous in the x,z directions, which implies that for any quantity Q, $\partial\langle Q\rangle/\partial x = \partial\langle Q\rangle/\partial z = 0$, where $\langle Q\rangle$ is a probability average of Q. From ergodic theory, the probability averages are estimated by spatial averaging over the two homogeneous directions, i.e.

$$\langle Q\rangle(y,t) = \frac{1}{L_x L_z}\int_{-L_x/2}^{L_x/2}\int_{-L_z/2}^{L_z/2} Q(x,y,z,t)dxdz\,, \tag{2.17}$$

and the Reynolds decomposition is used to define the fluctuating quantity $q(x,y,z,t) = Q(x,y,z,t) - \langle Q\rangle(y,t)$. With the simplifications provided by incompressible flow and statistical homogeneity in the streamwise and spanwise directions, the following equations for the mean momentum, $\langle U\rangle$, turbulent kinetic energy $k = 1/2\langle u^2+v^2+w^2\rangle$, mean scalar concentration $\langle\Phi\rangle$, and mean scalar fluctuation $\langle\phi^2\rangle$ can be obtained:

$$\frac{\partial\langle U\rangle}{\partial t} = -\frac{\partial\langle uv\rangle}{\partial y}, \tag{2.18}$$

$$\frac{\partial k}{\partial t} = -\frac{\partial\langle pv\rangle}{\partial y} - \frac{\partial\langle vk\rangle}{\partial y} - 2\langle uv\rangle\frac{\partial\langle U\rangle}{\partial y} - \varepsilon, \tag{2.19}$$

$$\frac{\partial\langle\Phi\rangle}{\partial t} = -\frac{\partial\langle v\phi\rangle}{\partial y}, \tag{2.20}$$

$$\frac{1}{2}\frac{\partial \langle \phi^2 \rangle}{\partial t} = -\frac{1}{2}\frac{\partial \langle v\phi^2 \rangle}{\partial y} - \langle v\phi \rangle \frac{\partial \langle \Phi \rangle}{\partial y} - \chi. \tag{2.21}$$

The dissipation-rate of turbulent kinetic energy is given by $\varepsilon = 2\nu \langle s_{ij} s_{ij} \rangle$, where $\nu = \mu/\rho$ is the kinematic viscosity and s_{ij} is the strain-rate tensor of the velocity fluctuations. The scalar dissipation-rate is $\chi = 2D \langle \nabla\phi \cdot \nabla\phi \rangle$. An important consequence of statistical homogeneity in the temporal shear layer is that the mean velocity in the cross-stream direction y is equal to zero. From conservation of mass, using homogeneity in x and z and incompressibility, then

$$\frac{\partial \langle V \rangle}{\partial y} = 0, \tag{2.22}$$

which implies that $\langle V \rangle$ is equal to a constant. Because the cross-stream velocity goes to zero at the free-slip boundaries, then $\langle V \rangle = 0$ everywhere (note that the fluctuations are not zero, i.e., $v \neq 0$).

2.3.2 Identification of self-similar region

A key characteristic of the shear layer is the emergence of a self-similar period of evolution in which the flow varies continuously in time and space, but does so in such a way that the characteristic *shapes* of the flow variables are preserved. For the temporal mixing layer discussed here, the existence of self-similarity requires that quantities which depend on the two independent variables (y, t) can be expressed in terms of a single similarity variable. For the quantity $Q(y, t)$ to be self-similar, there must exist a quantity $\hat{Q}(\xi)$, such that

$$\frac{Q(y,t)}{Q_0(t)} = \hat{Q}(\xi), \tag{2.23}$$

where $\xi = y/h(t)$ and $Q_0(t)$ is a reference quantity used to scale Q. The quantity $h(t)$ is a measurement of the thickness of the mixed region of fluid, which is known to increase over time due to turbulent entrainment.

The momentum thickness, δ_m, is most commonly used to describe the width of the mixing layer, which for constant density flows is

$$\delta_m = \int_{-\infty}^{\infty} \left(\frac{1}{4} - \frac{\langle U \rangle^2}{\Delta U^2} \right) dy. \tag{2.24}$$

The 'visual thickness' h can also be used to denote the width of the mixing layer, which is defined here as

$$h = y\big|_{\langle U \rangle = U_+ - 0.1\Delta U} - y\big|_{\langle U \rangle = U_- + 0.1\Delta U}, \tag{2.25}$$

i.e., the distance between y values corresponding to the upper and lower 10% of the mean velocity profile. This definition is not common in the literature, but it is arguably a better estimate of the integral scales of the flow [4]. As such, the visual thickness is used herein as the characteristic lengthscale of the mixing layer width.

Mixing lengthscales can also be defined for the passive scalar field that are analogous to the definitions for the velocity field above for both the 'scalar visual thickness' h_Φ and the 'scalar width' δ_Φ, that is:

$$h_\Phi = y\big|_{\langle \Phi \rangle = 0.9} - y\big|_{\langle \Phi \rangle = 0.1} \tag{2.26}$$

and

$$\delta_\Phi = \int_{-\infty}^{\infty} \langle \Phi \rangle \left(1 - \langle \Phi \rangle \right) dy. \tag{2.27}$$

The temporal evolution of the scalar is displayed in Figure 2.3, in which a spanwise slice of the scalar concentration is displayed for a) $t\Delta U/h_0 = 261$, b) $t\Delta U/h_0 = 462$ and c) $t\Delta U/h_0 = 546$. It is clear from this sequence that the width of the mixed region of fluid, whether defined by the visual or integrated thicknesses, increases significantly in time.

An important consequence of self-similarity is that the growth rate of the mixing layer width must be constant, i.e., $dh/dt = \text{const}$. This results in the well-established finding that the width of the mixing layer increases proportionally with time during the self-similar period of the temporal mixing layer [90]. Because both δ_m and

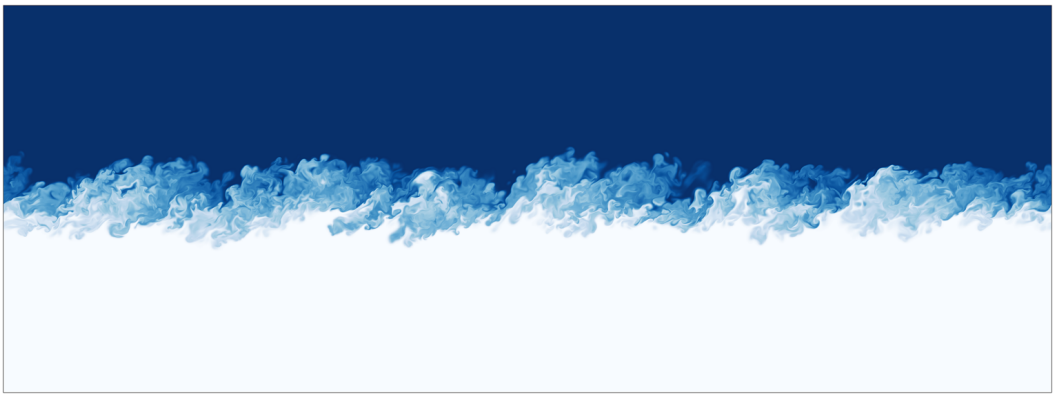

(a) $t\Delta U/h_0 = 261$

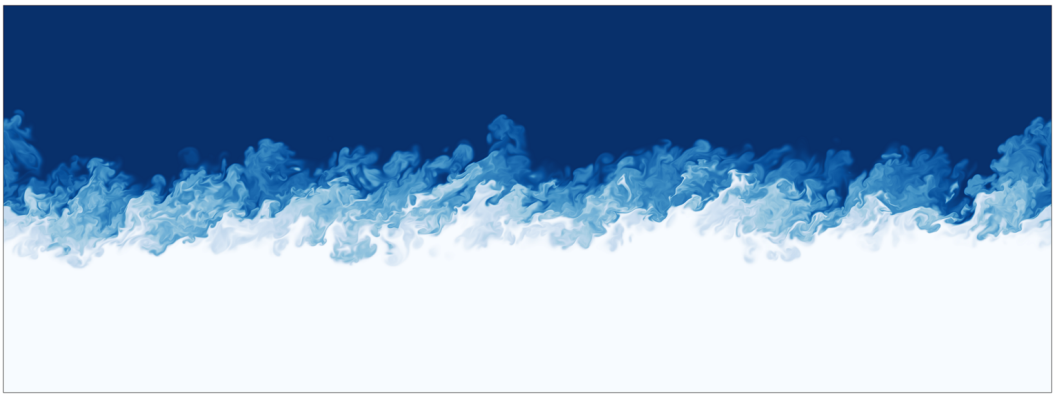

(b) $t\Delta U/h_0 = 462$

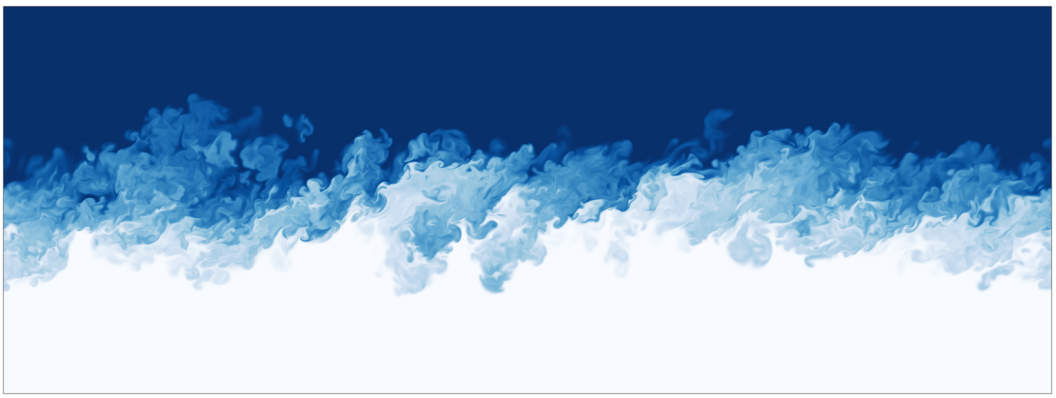

(c) $t\Delta U/h_0 = 546$

Figure 2.3: Temporal evolution of the scalar field in the mixing layer, displayed as two dimensional pseudocolor plots of scalar concentration. The color scale is linear, with blue corresponding to values of $\Phi = 1$ and white corresponding to $\Phi = 0$.

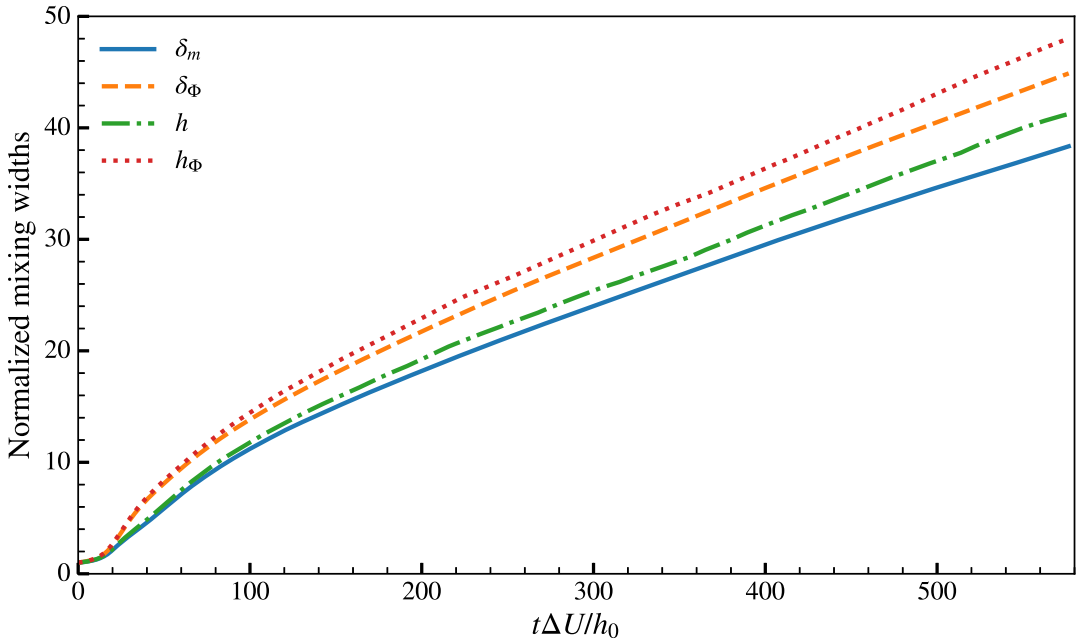

Figure 2.4: Evolution of mixing layer widths δ_m, δ_Φ, h, and h_Φ, as defined in equations 2.24 - 2.27. Widths are normalized by their respective values at $t = 0$. The mixing layer widths are expected to be proportional and to increase linearly with time during the self-similar period.

h characterize the width of the mixing layer, the two widths are proportional and increase linearly in time, e.g., $h \sim t^1$. Furthermore, from a self-similar analysis of equation (2.20), it can be shown that the scalar mixing widths are proportional to the velocity mixing widths, e.g., $h \sim h_\Phi$. The mixing widths for both the velocity and scalar fields, normalized by their initial values, are shown in figure 2.4 as a function of the non-dimensional time $t\Delta U/h_0$, where h_0 is the visual thickness at $t = 0$. The mixing widths demonstrate a clear linear trend after $t\Delta U/h_0 \approx 200$, indicating the emergence of the self-similar regime in the flow.

Another consequence of self-similarity is that the dissipation rates of turbulent kinetic energy, ε, and scalar variance, χ, attain a constant value when integrated

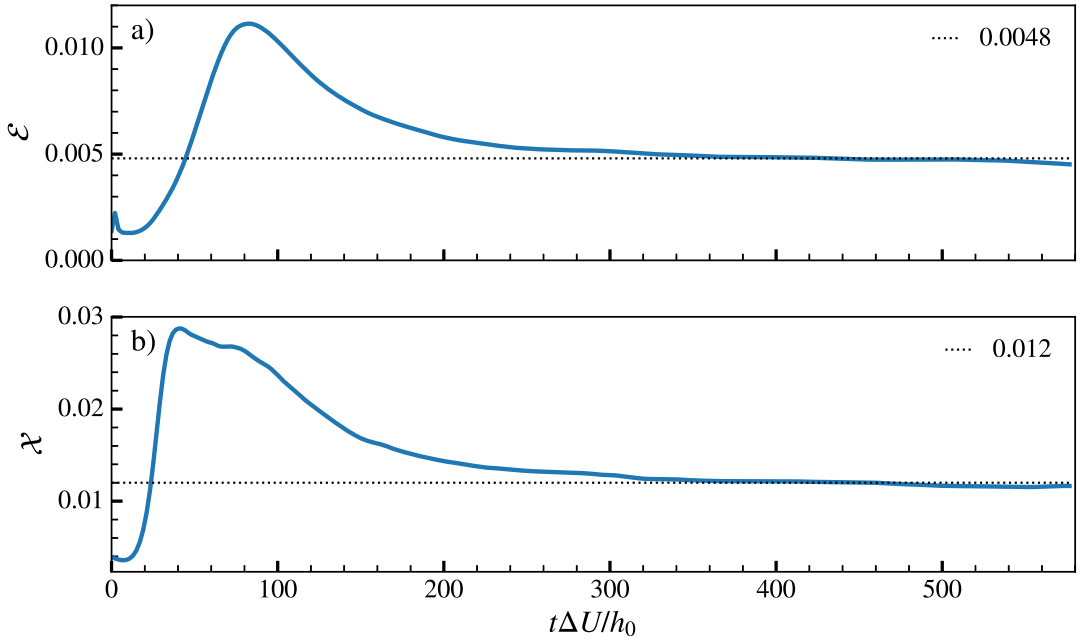

Figure 2.5: Time history of the integrated dissipation-rate of a) turbulent kinetic energy, $\mathcal{E}$, and b) scalar variance, $\mathcal{X}$. Dotted lines of constant value are included as reference.

across the shear layer. The integrated dissipation rates $\mathcal{E}$ and $\mathcal{X}$ are given by

$$\mathcal{E} = \frac{1}{\Delta U^3} \int_{-\infty}^{\infty} \varepsilon(y,t) dy, \tag{2.28}$$

$$\mathcal{X} = \frac{1}{\Delta \Phi^2 \Delta U} \int_{-\infty}^{\infty} \chi(y,t) dy. \tag{2.29}$$

As shown by figure 2.5a, $\mathcal{E}$ does in fact reach an approximate steady state after the initial transient period associated with the transition to turbulence. The value of $\mathcal{E}$ during the self-similar period is found to be approximately 0.0048, which is consistent with previous studies that have obtained a value between 0.004 and 0.006 [79, 1, 4]. Similarly, $\mathcal{X}$ reaches an approximate steady state after the transition to turbulence, as shown by figure 2.5b. The steady state value for $\mathcal{X}$ is approximately 0.012.

From these results, it is expected that the mixing layer will develop in a self-

preserving manner over the range $250 \leq t\Delta U/h_0 \leq 580$, wherein the width of the mixed region of fluid increases linearly in time and the integrated rate of dissipation across the shear layer is constant. In the case of the present DNS, the simulation parameters were carefully tuned to achieve a significant increase in the mixing layer width during the self-similar period. A large increase in h makes the self-similar scaling patterns more easily distinguishable from the inherent variation of the flow statistics. For the DNS presented here, the mixing layer width is found to increase by approximately 86%, from $h/h_0 \approx 22$ to ≈ 41, during the self-similar period.

Note that this identification of the self-similar region is unique to the simulation described here; initial conditions have a significant impact on the early growth of unstable modes in the shear layer, based on the initial spectrum and magnitude of the background perturbations. As such, it is not expected that the onset of self-similarity will occur at the same non-dimensional times for two simulations with sufficiently distinct initial conditions.

It should also be noted that self-similar growth will not continue indefinitely in the simulations since, once the lengthscales of the flow become large enough, the flow will interact with the boundaries and break self-similarity. For the results presented here, self-similarity is found to hold for the entirety of the simulation, except for a small deviation in the spanwise velocity fluctuations, $\langle w^2 \rangle$, at later times. However, the dissipation-rate and streamwise velocity correlations continue to demonstrate excellent self-similar behavior up to the end of the simulation at $t\Delta U/h_0 = 580$.

2.3.3 Turbulence characterization

To ensure that all of the relevant lengthscales in the DNS are properly resolved, the grid spacing should be, at maximum, 2.1 times the Kolmogorov lengthscale [74], defined as

$$\eta = \left(\frac{\nu^3}{\varepsilon} \right)^{1/4}. \tag{2.30}$$

The value of ε is taken at the centerline of the mixing layer, corresponding to the peak of the turbulence fluctuations and dissipation rate. The ratio $\Delta x/\eta$ throughout the present simulation is plotted in figure 2.6a as a function of the non-dimensional mixing layer time ($t\Delta U/h_0$), with a dotted line representing the value of 2.1. The peak of the curve, which obtains a value of approximately $\Delta x/\eta = 1.9$, occurs during the transition of the mixing layer into turbulence, where the smallest scales in the flow are formed. During the self-similar evolution of the velocity field ($t\Delta U/h_0 > 250$) $\Delta x/\eta$ is < 1.3, indicating a well-resolved velocity field consistent with other simulations reported in the literature [4, 1, 65, 79]. The Batchelor scale, $\eta_B = \eta \mathrm{Sc}^{-1/2}$, associated with the dissipation scales for the passive scalar, will be larger than the Kolmogorov scale η since the Schmidt number is slightly less than unity. This ensures that the scalar field is always similarly (or more) resolved than the velocity field.

Turbulent flows are commonly characterized by the transverse Taylor lengthscale, λ_g, defined by [74] as

$$\lambda_g = \sqrt{15\nu/\varepsilon}u' \,, \tag{2.31}$$

where the rms velocity is given by $u' = \langle (u^2 + v^2 + w^2)/3 \rangle^{1/2}$ and the flow is assumed to be isotropic. Due to the strong inhomogeneity of the shear layer, the longitudinal Taylor scale, λ_1, may differ somewhat from the transverse scale. The longitudinal Taylor length scale is defined as

$$\left\langle \left(\frac{\partial u_1}{\partial x_1} \right)^2 \right\rangle = 2\frac{\langle u_1^2 \rangle}{\lambda_1^2}. \tag{2.32}$$

Additionally, a Taylor lengthscale associated with the passive scalar field, λ_ϕ, can be defined as

$$\left\langle \frac{\chi}{6D} \right\rangle = \frac{\langle \phi^2 \rangle}{\lambda_\phi^2}, \tag{2.33}$$

assuming isotropy. Directional Taylor scales were also calculated for the passive scalar, but were found to be almost invariant with direction. As such, the definition in (2.33) will be used to characterize λ_ϕ. As in (2.30), the Taylor lengthscales are evaluated at

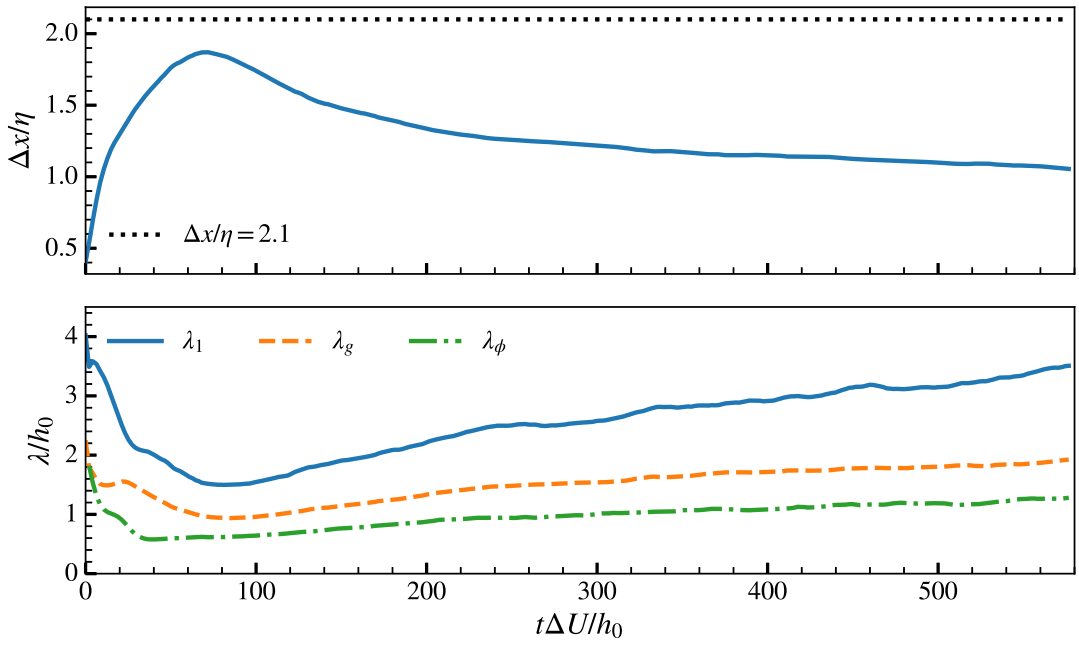

Figure 2.6: a) Grid spacing of the DNS compared to Kolmogorov scale, η. b) Evolution of the longitudinal, transverse, and scalar Taylor length scales $\lambda_1, \lambda_g, \lambda_\phi$, normalized by the initial mixing layer width, h_0.

the centerline of the shear layer corresponding to the maximum values of turbulence and scalar fluctuations and dissipation rates.

The evolution of the relevant Taylor lengthscales are displayed in figure 2.6b, which are shown to increase throughout the development of the shear layer as expected. However, due to Reynolds number scaling, the increase in the Taylor lengthscale is not as notable as the increase in the mixing layer width over the self-similar period. The Taylor Reynolds number, $\mathrm{Re}_\lambda = u'\lambda_g/\nu$, increases from a value of roughly 130 to 168 during the self-similar period of the simulation, while the turbulent Reynolds number based on the mixing layer width, $Re = \Delta U h/\nu$, increases from approximately $12,000$ to $22,000$.

Because the Schmidt number in the present DNS is approximately unity, the Taylor lengthscales of the velocity and scalar fields are expected to be proportional during the self-similar period, i.e., $\lambda_1 \sim \lambda_\phi$. This is validated in the present DNS by the fact that the ratio $\lambda_1/\lambda_\phi \approx 2.7$ throughout the self-similar region.

2.3.4 Self-similar statistics

In the following analysis, the self-similar forms for $\langle U \rangle$, $\langle u_i u_i \rangle$, $\langle uv \rangle$ and ε are assumed to be:

$$\langle U \rangle (y,t) = \Delta U \hat{U}(\xi), \tag{2.34}$$

$$\langle u_i u_i \rangle (y,t) = \Delta U^2 \hat{R}_{ii}(\xi); \quad \text{no sum on } i,\ i = 1, 2, \text{or } 3, \tag{2.35}$$

$$\langle uv \rangle (y,t) = \Delta U^2 \hat{R}_{uv}(\xi), \tag{2.36}$$

and

$$\varepsilon(y,t) = \frac{\Delta U^3}{h(t)} \hat{\varepsilon}(\xi). \tag{2.37}$$

To verify that the temporal mixing layer is developing as expected, self-similar profiles of the fluctuating velocities and the Reynolds stress from the present simulation are compared against several data sets from the literature in figure 2.7. Normalized, instantaneous profiles are averaged over the self-similar period (defined in § 2.3.2) to

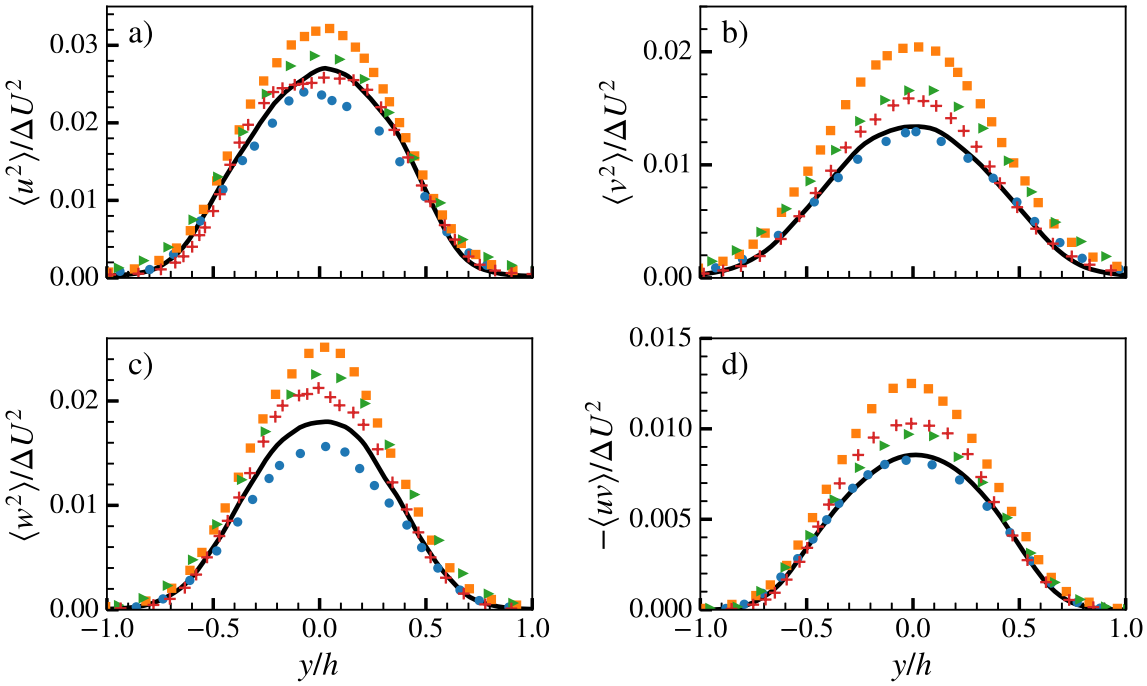

Figure 2.7: Self-similar profiles of a) - c) fluctuating velocities, and d) Reynolds stress, compared to published data sets. Solid lines represent time-averaged data over the self-similar period from the present DNS, and symbols represent profiles from previous studies, as follows: [4] are circles, [1] are squares, [5] are triangles and [79] are plus signs.

create the solid black curve, with self-similar results from previous studies represented as colored symbols. Profiles of the mean square fluctuating velocities, $\langle u_i u_i \rangle$ are plotted in figures 2.7a-c, respectively, with the Reynolds stress, $\langle uv \rangle$, plotted in figure 2.7d, all as functions of the normalized cross-stream direction, y/h. Data from the present DNS compare favorably with previous studies, agreeing most closely with the temporal mixing layer simulation performed by Rogers and Moser [79]. Overall, the results of this comparison demonstrate that the self-similar development of the present simulation is comparable to established experimental and numerical simulation data.

In addition to the velocity field, the passive scalar field also evolves in a self-similar manner. The self-similar forms of the scalar field statistics $\langle \Phi \rangle$, $\langle \phi^2 \rangle$, and χ are assumed to be:

$$\langle \Phi \rangle (y,t) = \Delta\Phi \hat{\Phi}(\xi), \tag{2.38}$$

$$\left\langle \phi^2 \right\rangle (y,t) = \Delta\Phi^2 \hat{\phi}^2(\xi), \tag{2.39}$$

and

$$\chi(y,t) = \frac{\Delta\Phi^2 \Delta U}{h(t)} \hat{\chi}(\xi). \tag{2.40}$$

The self-similar forms of the fluctuating scalar concentration, $\langle \phi^2 \rangle$, and the scalar dissipation-rate, χ, are plotted in figure 2.8a and 2.8b, respectively. Colored, dashed lines represent normalized, instantaneous profiles of the scalar field statistics at several time points during the self-similar period. The solid black curve is the time averaged profile over the self-similar period. The agreement between the time-averaged profile and the instantaneous profiles demonstrate that $\langle \phi^2 \rangle$ and χ evolve in a self-similar manner.

2.4 Estimating iso-surface properties

Despite the wealth of data available from modern DNS, there exist significant challenges to accurately and efficiently extract iso-surface properties, such as surface area,

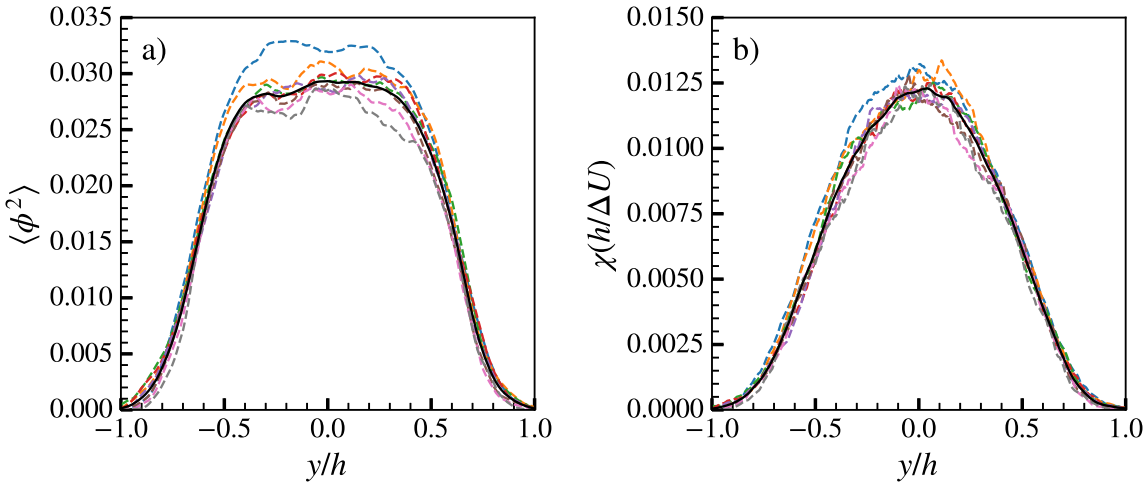

Figure 2.8: Self-similarity of fluctuating scalar concentration, ϕ, and scalar dissipation-rate, χ, for a) $\Phi_{\text{iso}} = 0.5$ and b) $\Phi_{\text{iso}} = 0.95$. Dashed lines represent instantaneous averages throughout the self-similar region, and solid lines represent the time-averaged value over the self-similar period.

from DNS data. Indeed, this challenge exists not only in the fluid dynamics communities, but in many other disciplines as well. There are many methods to estimate iso-surface area or other such integrals such as surface polygonization or Monte Carlo methods [83], although significant drawbacks exist [66, 50].

To address these issues, Storti and Yurtoglu *et al.* have developed a novel numerical algorithm to directly evaluate surface integrals from a scalar field sampled on a discrete grid [109, 88]. It is important to note that this method does not rely on interpolation to, or reconstruction of, the iso-surface. In essence, the methodology provides an approach for estimating the instantaneous iso-surface area density, Σ', in a manner that is consistent with equation 1.7 in § 1.4. Then, the mean iso-surface area density, Σ, is calculated according to

$$\Sigma(t) = \frac{1}{L^3} \int_{\mathcal{V}} \Sigma' d\mathcal{V} = \frac{A_{\text{iso}}}{L^3}, \tag{2.41}$$

for the homogeneous, isotropic turbulence described in Chapter 3, or

$$\Sigma(y,t) = \frac{1}{L_x L_z (m\Delta y)} \int_{-L_x/2}^{L_x/2} \int_{y}^{y+(m\Delta y)} \int_{-L_z/2}^{L_z/2} \Sigma'(x,y,z,t) dx dy dz, \tag{2.42}$$

for the inhomogeneous mixing layer described in Chapters 4 and 5. Here, m is an integer value that denotes the number of grid points included in the average for the y direction. For $m = 1$, this average reduces to the two-dimensional average defined in equation (2.17). The y profiles of Σ were compared for several values of m, which were found to be insensitive of the value of m as long as $m\Delta y$ is small compared to typical length scales of the mean flow; for the present study, a value of $m = 20$ is used.

Although the iso-surface average defined in (1.10) is utilized often in the literature, it can be poorly defined unless integrated over the entire iso-surface. In the case of the present DNS, it was found that the iso-surface area density, $\Sigma(y,t)$, takes on a Gaussian-like profile that decays to zero away from its peak (refer to Chapter 4). This means that, as given by equation (1.10), the iso-surface average, $\langle Q \rangle_s$, is undefined near the edges of the mixing layer because $\Sigma \to 0$ as $y \to \pm L_y/2$. While the surface average is an intuitive concept, it is more practical to consider instead the *weighted* surface average,

$$\langle Q \rangle_s \Sigma = \langle Q\Sigma' \rangle = \frac{1}{L_x L_z (m\Delta y)} \int_{-L_x/2}^{L_x/2} \int_{y}^{y+(m\Delta y)} \int_{-L_z/2}^{L_z/2} Q\Sigma' dx dy dz. \tag{2.43}$$

In fact, from inspection of (1.9), it can be seen that each of the terms on right right-hand side of the equation makes use of the weighted iso-surface average, $\langle Q\Sigma' \rangle$, rather than the iso-surface average, $\langle Q \rangle_s$. As discussed above, the value of m in the present study is set to 20, which provides good statistical convergence. In addition, the data have been averaged in time to reduce statistical fluctuations, with an averaging width of approximately 8 non-dimensional time units, $t\Delta U/h_0$. As will be shown below, the terms in (1.9) are expected to vary smoothly in time and space such that the averaging process described accurately retains the characteristic features of the flow.

In some cases, it is helpful to understand a quantity that has been averaged over the entire iso-surface contained in the computational domain. In these cases, the quantity can be evaluated by integrating the averaged quantity in the cross-stream direction. For example, the surface area of an iso-surface, A_{iso}, can be evaluated by

$$\frac{A_{\text{iso}}}{A_0} = \int_{-L_y/2}^{L_y/2} \Sigma \, dy, \tag{2.44}$$

where $A_0 = L_x L_z$ is the surface area at $t = 0$.

Advantages to using this algorithm are twofold. First, Resnikoff and Wells [78] have shown that, when using Daubechie's wavelets, the approximation of the iso-surface integral is guaranteed to converge to the true value, assuming that the grid can be refined to be arbitrarily small. This provides a distinct advantage over methods that reconstruct the surface using triangular patches, which may not always converge to the true answer even when the grid is refined [110]. Another advantage to this method is that the surface integral is converted to a volume integral, which can benefit significantly from parallelization via GPUs [109]. Use of this novel numerical method allows for greater confidence in the accuracy of results, and for surface properties to be evaluated for a large number of iso-values and time points, giving a better view of the iso-surface behavior. For further details regarding the direct surface integration used for this work, see Appendix A.

Although subtle, the distinction between the mean iso-surface area density $\Sigma(y,t)$, as defined in (2.42), and the volume-averaged iso-surface area density in (2.41) is crucial. Due to the inhomogeneity of the mixing layer configuration, $\Sigma(y,t)$ is an intrinsic quantity of the flow, whereas the volume average, $\Sigma(t)$, depends on the volume chosen for integration. This is easily demonstrated by considering two domains with equal L_x and L_z, but one is twice the length, $2L_y$, of the other in the cross-stream direction. For the temporal mixing layer presented here, the surface area A_{iso} would not change between the two cases, but the domain volume $L_x L_y L_z$ would double causing the 'total' iso-surface area density, $\Sigma(t)$, to differ by a factor of two. In

contrast, the $y-$dependent iso-surface area density, $\Sigma(y,t)$ would not differ between the two cases.

Chapter 3

ON THE KINEMATICS OF ISO-SURFACE AREA DENSITY IN DECAYING ISOTROPIC, HOMOGENEOUS TURBULENCE

This chapter focuses on gaining a better understanding of the fundamental behavior of the iso-surface transport equation, Equation (1.9), by examining iso-surface transport of a conserved, passive scalar mixing in decaying homogeneous, isotropic turbulence. This simplified turbulence problem isolates the effects of two important aspects of the behavior of an iso-surface: the growth of the surface area due to turbulence straining, and the destruction of surface area due to molecular diffusion and curvature effects. This chapter is organized as follows: § 3.1 will present primary results of the analysis, including the evolution of the iso-surface area density, Σ, and the terms in its evolution equation. This will lead into more detailed investigations of the strain-rate term in § 3.2 and the propagation/curvature term in § 3.3. Portions of this chapter are published in *Journal of Turbulence*, Reference [8].

3.1 General results

Figure 3.1 is a 3D visualization of the iso-surface given by $Z_{\text{iso}} = 0.5$ at $t = 0.5$ for the a) initially isotropic case (Case A) and b) the initially planar scalar field (Case B). The effect of the velocity field to strain and stretch the iso-surface, thereby increasing the surface area, is clearly demonstrated by the 3D visualization when compared to the initial state, shown in Figure 2.1. Despite significant differences between the two scalar fields at $t = 0$, the iso-surfaces at $t = 0.5$ are qualitatively similar. Large-scale differences remain between the two cases, which will be investigated by the

forthcoming analysis.

Using DNS results, the iso-surface area density is calculated for several values of Z_{iso}, and the surface density normalized by its initial value is plotted as a function of time for Case A (the initially isotropic scalar field) in Figure 3.2a, and Case B (the initially planar scalar field) in Figure 3.2b. The surface area density of all iso-surfaces is found to increase rapidly as the unperturbed scalar field adjusts to the turbulent motions (as discussed in § 2.1). This initial period of adjustment is influenced by the fact that the velocity and scalar fields are initially uncorrelated. After this initial growth (i.e., when $t > 0.5$), Σ becomes dependent on its iso-surface value, Z_{iso}; iso-surfaces with values close to $\overline{Z}$ continue to increase, while surfaces far from $\overline{Z}$ (near the values of 0 and 1) reach a maximum surface area density and then begin to decrease with time. As the scalar field is stirred by the turbulence and begins to mix, the area density of iso-surfaces far from $\overline{Z}$ is expected to tend towards zero with time, as molecular diffusion acts to destroy scalar gradients and create a homogeneous mixture equal to $\overline{Z} = 0.5$ throughout the domain. The following sections will further examine the behavior of various iso-surfaces in the following analysis.

There are some obvious differences in the evolution of the iso-surface area density between the two different scalar fields, despite their interaction with the same turbulent velocity field. The $Z_{\text{iso}} = 0.5$ iso-surface appears to asymptotically approach a maximum iso-surface density ($\partial\Sigma/\partial t = 0$) around $t = 2.5$ in Case A, whereas the surface area density is still increasing strongly ($\partial\Sigma/\partial t > 0$) at $t = 2.5$ in Case B. Furthermore, the normalized surface density is higher for Case B, indicating that the surface has stretched more than the surface in Case A compared to their respective initial states. It should be noted that the surface density in Case A demonstrates a high degree of symmetry about $\overline{Z}$. This symmetry about $\overline{Z} = 0.5$ is expected, and is highlighted in Figure 3.2a by symbol color. Symmetric iso-surfaces (such as $Z_{\text{iso}} = 0.05$ and 0.95) exhibit qualitatively similar behavior in Case B, although they do not display the same level of symmetry as iso-surfaces in Case A. The lack of total

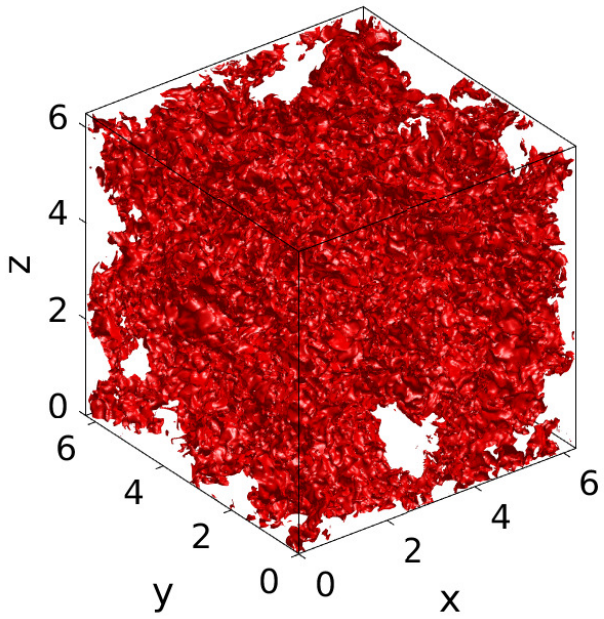

(a) Case A

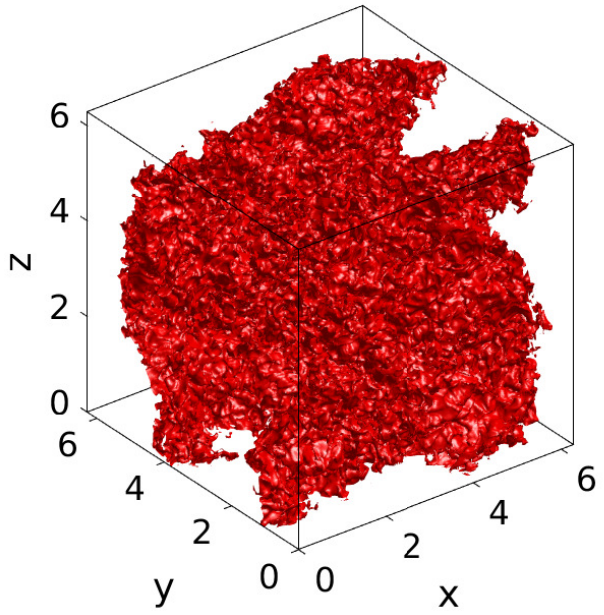

(b) Case B

Figure 3.1: Three-dimensional visualization of the $Z_{\text{iso}} = 0.5$ scalar iso-surface at $t = 0.5$ corresponding to the a) initially isotropic case and b) initially planar case.

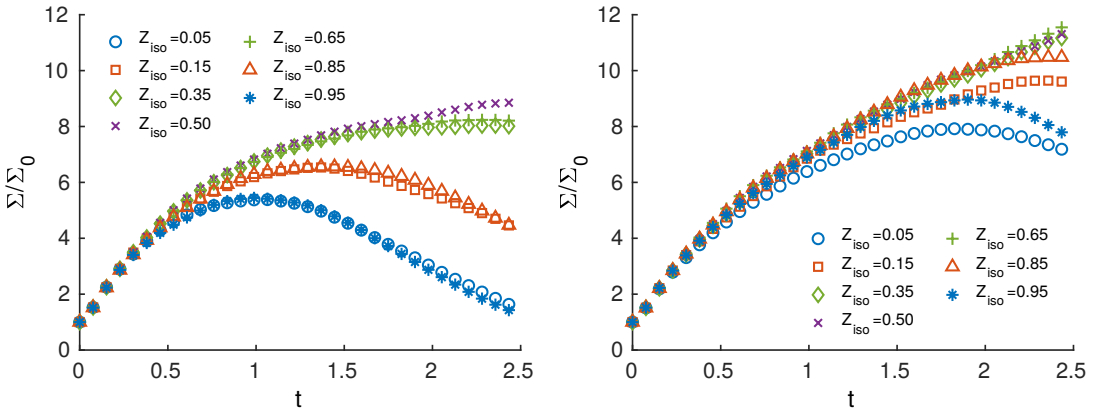

(a) Case A, Initially isotropic scalar field.

(b) Case B, Initially planar scalar field.

Figure 3.2: Evolution of iso-surface area density, Σ, normalized by the initial value, Σ_0, for a) Case A and b) Case B with $Z_{\text{iso}} = [0.05, 0.15, 0.35, 0.5, 0.65, 0.85, 0.95]$.

symmetry especially present in Case B is due to the error in volume averaging, with the limited domain volume and the fact that the planar initial condition is less volume filling; that is, especially in Case B, each iso-surface interacts with only a small portion of the velocity field which decreases the accuracy of the volume average.

The surface density balance equation can provide additional insight into the underlying physics of iso-surface evolution. For volume-averaged, incompressible turbulence and a passive, conserved scalar, Equation (1.9) simplifies to

$$\underbrace{\frac{1}{\Sigma}\frac{\partial \Sigma}{\partial t}}_{\text{Term I}} = \underbrace{-\langle \mathbf{nn} : \mathbf{S} \rangle_s}_{\text{Term III}} + \underbrace{\langle w \ \nabla \cdot \mathbf{n} \rangle_s}_{\text{Term V}}, \tag{3.1}$$

where $\mathbf{S}$ is the strain-rate tensor,

$$\mathbf{S} = \frac{1}{2}\left(\nabla \mathbf{u} + \nabla \mathbf{u}^T\right). \tag{3.2}$$

As will be discussed below, Term III, involving the strain-rate, increases the surface area density while Term V, involving iso-surface propagation and the local radius of curvature, decreases the surface area density.

Terms I, III, and V from Equation (3.1) have been computed for the two scalar fields and are plotted versus time in Figure 3.3. For clarity, the terms from only two

iso-surfaces are plotted, corresponding to $Z_{\text{iso}} = 0.5$ (circles) and $Z_{\text{iso}} = 0.05$ (squares). Due to the qualitatively symmetric behavior of iso-surfaces about the mean value of Z, these two values represent an upper and lower bound on the surface-averaged terms for iso-surfaces $0.05 < Z_{\text{iso}} < 0.95$. It is worth noting that, in computing all three terms from the DNS data, the sum of Terms III and V shows good agreement with Term I for the data presented below, with a maximum error of approximately 2%. This lends confidence to the accuracy of the numerical methods used in this study.

Initially for both cases, the surface area density increases rapidly due to flow straining (Term III), as demonstrated by the large positive values of Term I for $t < 0.5$. However, the effect of the strain-rate on the surface is compensated for quickly as the small scales developed from the straining motions increase the surface curvature, which then acts to destroy surface area in combination with diffusion (Term V). After this initial adjustment, the combination of these two terms determines the behavior of $\partial\Sigma/\partial t$ (Term I), which grows more slowly and ultimately decays.

The rate of change of Σ takes on large values early in the simulation as the initial scalar field adjusts to the turbulent flow, but decreases quickly with time. At late times, the rate of change of Σ appears to asymptotically approach zero for $Z_{\text{iso}} = \overline{Z}$, representing a balance between the production from straining motions and destruction from diffusion and curvature effects. In contrast, the rate of change of Σ becomes negative for iso-surfaces far from $\overline{Z}$, corresponding to a net destruction of iso-surface area (which is supported by the decreasing surface area density shown in Figure 3.2). As illustrated above in Figure 3.2, Case A displays a stronger dependence on Z_{iso} than Case B. Despite the fact that both simulations have identical velocity fields, there is clearly some 'memory' associated with the initial condition of the scalar field. This will be investigated further by examining the remaining terms in Equation (3.1) below.

The strain-rate term (Term III) is found to be a source of iso-surface area growth for all values of Z_{iso} and for all times. The rate of iso-surface area production decays

with time for both of the initial scalar fields, with iso-surfaces far from $\overline{Z}$ decaying more quickly than the surface with $Z_{\text{iso}} = \overline{Z}$. The magnitude of the strain-rate effects on the $Z_{\text{iso}} = 0.5$ iso-surface is nearly identical for both the isotropic and planar scalar fields, suggesting that the behavior of Term III depends only on the turbulent velocity field. However, the dependence of Z_{iso} on the value of Term III, especially at late times, may indicate that the velocity field interacts preferentially with certain iso-surfaces.

The effect of surface curvature and molecular diffusion (Term V) is found to be a sink of iso-surface area density for all iso-surfaces, both initial scalar fields, and for all times. Similar to Term III, the magnitude of Term V decreases in time for all iso-surfaces, although the rate of decay depends on the value of Z_{iso} and the initial scalar field. For iso-surfaces near $Z_{\text{iso}} = \overline{Z}$, Term V decays at a similar rate as Term III, such that the rate-of-change of surface area density (Term I) becomes approximately 0. Iso-surfaces far from $\overline{Z}$ demonstrate different behavior, depending on the initial scalar field used for the simulation. In Case A, the $Z_{\text{iso}} = 0.05$ iso-surface takes on a more negative value for Term V, which results in the net destruction of iso-surface area when combined with Term III. Interestingly, the $Z_{\text{iso}} = 0.05$ iso-surface does not follow the same trend in Case B , and instead agrees well with the value of Term V for $Z_{\text{iso}} = \overline{Z}$.

In summary, initial investigations into the source terms governing the evolution of surface area density have raised two points of interest. First, the behavior of Term III appears to be independent of the initial distribution of the scalar field, yet shows a slight dependence on the value of Z_{iso}. Second, Term V exhibits a dependence on both the initial scalar field as well as the the value of Z_{iso}. Additional physical insight into these processes will be gained by examining Terms III and V in further detail in §§ 3.2 and 3.3, respectively.

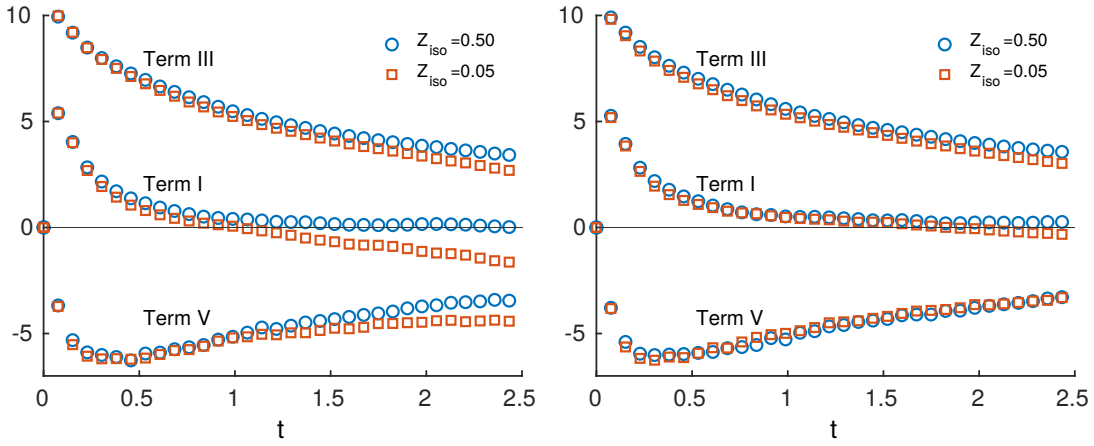

(a) Case A (b) Case B

Figure 3.3: Time evolution of Terms I, III and V in Equation (3.1), for $Z_{\text{iso}} = 0.5$ (circles) and 0.05 (squares) for a) Case A and b) Case B.

3.2 Term III

To examine Term III in more detail, note that the strain-rate tensor, $\mathbf{S}$, can be decomposed into its principal axes [43], such that

$$-\langle \mathbf{nn} : \mathbf{S} \rangle_s = \underbrace{-\langle \lambda_1 \psi_1^2 \rangle_s}_{\text{III}_\alpha} \underbrace{-\langle \lambda_2 \psi_2^2 \rangle_s}_{\text{III}_\beta} \underbrace{-\langle \lambda_3 \psi_3^2 \rangle_s}_{\text{III}_\gamma}, \tag{3.3}$$

where λ_i are the eigenvalues of the strain-rate tensor. The eigenvalues are ordered from largest to smallest, so that $\lambda_1 \geq \lambda_2 \geq \lambda_3$. Due to incompressibility, the eigenvalues must sum to zero. This formulation guarantees that λ_1 represents extensive motions, whereas λ_3 represents compressive motions of the strain-rate tensor. The scalar quantity ψ_i is the dot product of the scalar normal vector with the i^{th} eigenvector $\mathbf{e}_i$ of $\mathbf{S}$, i.e., $\psi_i = \mathbf{n} \cdot \mathbf{e}_i$. Physically, ψ_i represents the cosine of the angle between the iso-normal vector and the i^{th} principal axis of the strain-rate tensor. Defined in this way, the effect of the strain-rate on surface area density production can be split into contributions from motions that always act to stretch the fluid (Term III_α), always act to compress the fluid (Term III_γ), and an intermediate direction that may

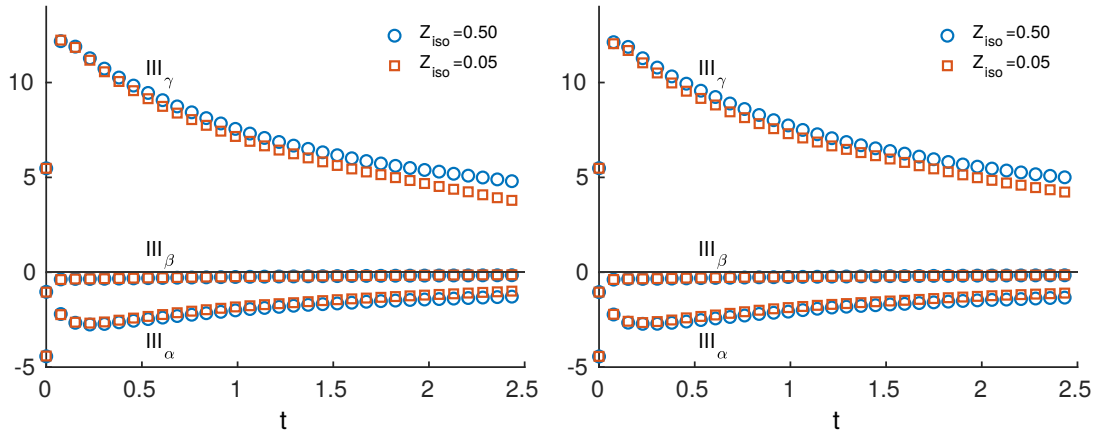

(a) Case A (b) Case B

Figure 3.4: Time evolution of Terms III_α, III_β and III_γ for $Z_{\mathrm{iso}} = 0.5$ (circles) and $Z_{\mathrm{iso}} = 0.05$ (squares) for a) Case A and b) Case B.

take on extension or compression to maintain incompressibility (Term III_β).

In Figure 3.4, the decomposition of Term III is plotted as functions of time and iso-surface level. From these data, it is found that the production of surface area is exclusively due to Term III_γ, which corresponds to the direction of the most compressive strain. This is expected from the sign convention in Equation (3.3). The contribution from Term III_α is found to be negative for the entire simulation time, suggesting that straining motions in the most extensive direction acts as a sink of iso-surface area density. Term III_β is also found to be negative throughout the simulation, but is small compared to the magnitude of the contributions from Terms III_α and III_γ. The magnitude of each term decays with time, which is consistent with previous results for Term III in Figure 3.3.

Interestingly, Terms III_α and III_γ display a weak dependence on Z_{iso} similar to Term III in Figure 3.3, where smaller magnitudes are associated with iso-surfaces far from $Z_{\mathrm{iso}} = \overline{Z}$. This dependence is explored further by examining the individual components of Term III, namely the alignment between the iso-surface normal vector, ψ_i, and the distribution of eigenvalues on the iso-surface.

The alignment between the scalar gradient and the principal axes of the strain-rate tensor was previously examined by Ashurst et al. [2] and Yeung et al. [108], who found that the scalar gradient was most likely to align in the direction with the most compressive strain. This analysis is extended by analyzing the alignment of the principal axes of the strain-rate tensor with individual iso-surfaces, rather than the entire scalar gradient field. In order to find the distribution of the alignment over the iso-surface, it is not sufficient to look at the distribution of $|\psi_i|$ conditioned on a particular value of Z_{iso}; rather, it is necessary to take into account the local surface area. In particular, consider a surface-weighted probability density function (pdf) such that the integral over the sample space yields the surface-averaged value (defined in Equation (1.10)). In other words, given the quantity Q, calculate its surface-weighted pdf, f_s, such that

$$\langle Q \rangle_s = \int_{-\infty}^{\infty} q f_s(q) \mathrm{d}q.$$

This is accomplished rather simply by weighting the bin counts of a histogram by the local value of $|\nabla Z|$.

Figure 3.5 displays the surface-weighted probability distributions of ψ_i at $t = 2.5$ for both of the initial scalar fields. The present results, as displayed in Figure 3.5, agree well with previous results [2, 108], suggesting that the iso-surface normal vector aligns preferentially with the most compressive strain. From Figure 3.5, this alignment appears to be independent of the iso-level and initial scalar distribution, indicating that the scalar iso-surfaces will tend to align similarly in response to straining motions, regardless of iso-value or initial condition. It is also worth noting that this alignment is expected to change in the presence of chemical reactions, i.e., the flame surface has been shown to align with the most extensive strain-rate due to thermal expansion from combustion reactions [16, 15, 55].

Next, the probability distributions of the principal strain-rates λ_1, λ_2, and λ_3 conditioned on scalar iso-surfaces are shown in Figure 3.6. It should be noted that

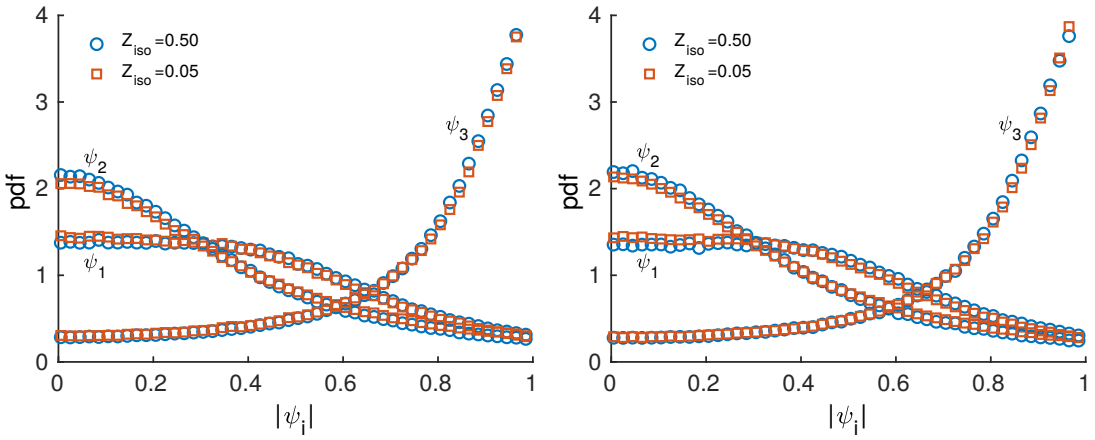

(a) Case A (b) Case B

Figure 3.5: Surface-weighted probability distributions of ψ_i at $t = 2.5$ for iso-surfaces $Z_{\text{iso}} = 0.5, 0.05$ in a) Case A and b) Case B.

the pdf has been weighted by the local surface area to create a surface-weighted pdf. The pdf's are calculated for $t = 2.5$, corresponding to the time when Term III exhibits the greatest dependence on Z_{iso}. Interestingly, the shapes of the pdf's are consistent between Cases A and B. The shape is also largely preserved between individual iso-surfaces, with a slight shift of the peak value to a lower magnitude for extreme values of Z_{iso}. This result is consistent with the results seen for Term III in Figure 3.3 above, which displayed somewhat lower rates of production for iso-surfaces far from $\overline{Z}$.

3.3 Term V

The diffusion speed, w, is commonly decomposed into normal and tangential components [94], defined as

$$w = \underbrace{D\frac{\nabla Z \cdot \nabla|\nabla Z|}{|\nabla Z|^2}}_{w_N} \underbrace{-D(\nabla \cdot \mathbf{n})}_{w_T}, \tag{3.4}$$

where w_N is related to diffusion normal to the iso-surface, and w_T is related to the iso-surface curvature. Using this definition, Term V in Equation (3.1) can also be

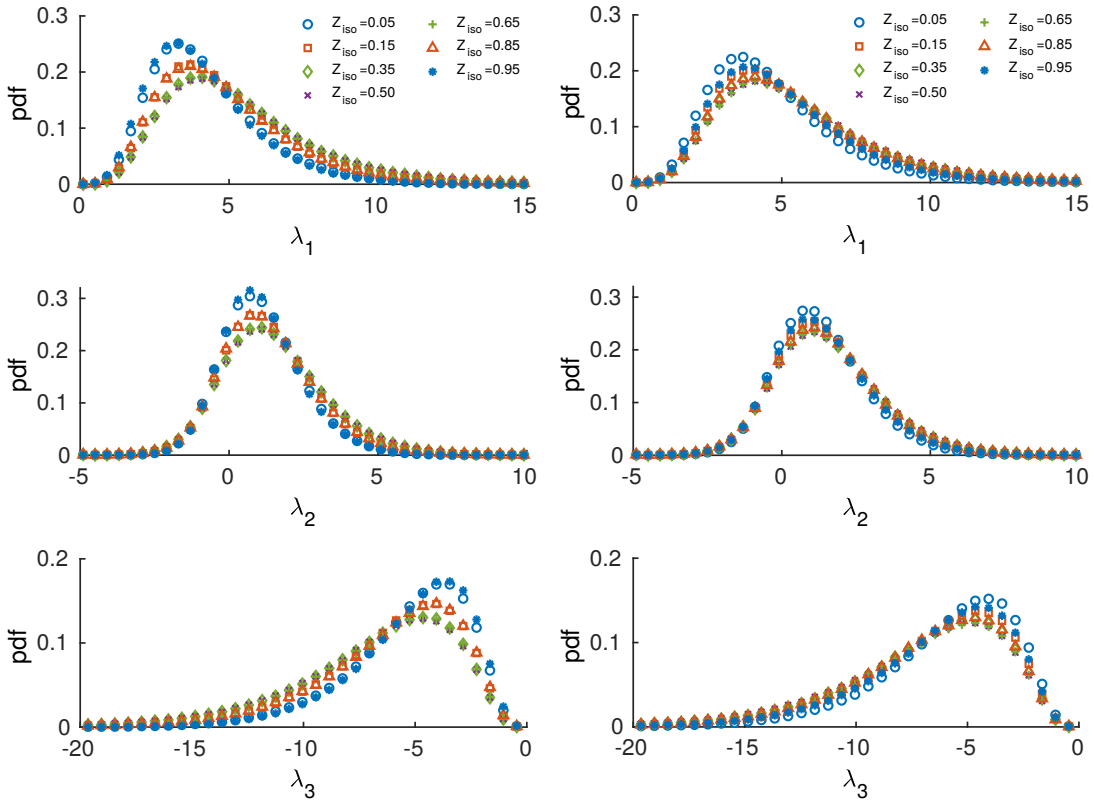

(a) Case A (b) Case B

Figure 3.6: Probability distributions of the principal strain-rates, conditioned on iso-surfaces $Z_{\text{iso}} = 0.5, 0.05$ at $t = 2.5$.

decomposed into normal and tangential components:

$$\langle w\ \nabla \cdot n \rangle_s = \underbrace{\langle w_N(\nabla \cdot \mathbf{n}) \rangle_s}_{V_N} \underbrace{-D \left\langle (\nabla \cdot \mathbf{n})^2 \right\rangle_s}_{V_T}. \tag{3.5}$$

Note that the tangential component, V_T, is related to the curvature squared ($(\nabla \cdot \mathbf{n})^2$) and is always a sink of iso-surface area. V_N may take on both positive or negative values. Also note that Term V is zero for a flat surface, i.e., one whose principal curvatures are zero (see Equation (1.2)).

Figure 3.7 plots Term V along with the normal and tangential components for iso-surfaces $Z_{\text{iso}} = 0.5$ and $Z_{\text{iso}} = 0.05$ versus time for both initial scalar fields. Qualitatively, Terms V_N and V_T behave similarly to Term V throughout the simulation, exhibiting a steep increase in magnitude as the scalar field adjusts to the flow, and then decreasing when $t > 0.5$. Term V_N has a non-trivial, negative value for both initial conditions, indicating that w_N and $\nabla \cdot \mathbf{n}$ are negatively correlated. This result is consistent with Dopazo et al. [28] for a scalar iso-surface in homogeneous turbulence, but is somewhat contrary to Van Kalmthout et al., [94] who found that $\langle w_N \nabla \cdot \mathbf{n} \rangle_s \simeq \langle w_N \rangle_s \langle \nabla \cdot \mathbf{n} \rangle_s$ for non-premixed combustion in a 2D compressible mixing layer. It is possible that the normal component of the diffusion velocity is less correlated with the curvature when the iso-surface is subjected to a strongly anisotropic flow such as a mixing layer.

As observed in Figure 3.3 above, the behavior of Term V for iso-surfaces far from $\overline{Z}$ demonstrates a clear dependence on the initial condition. This behavior is present in both Terms V_N and V_T, which exhibit a similar dependence on the initial distribution of the scalar field. In order to gain additional insight, the individual components of Term V will be examined, specifically the diffusion velocity w and curvature $\nabla \cdot \mathbf{n}$, as well as their respective rms values.

First, the surface-averaged diffusion velocity, $\langle w \rangle_s$, is plotted in Figure 3.8 as a function of time and Z_{iso} for both initial scalar fields. Note that the mean diffusion velocity takes on both positive and negative values depending on the direction of iso-

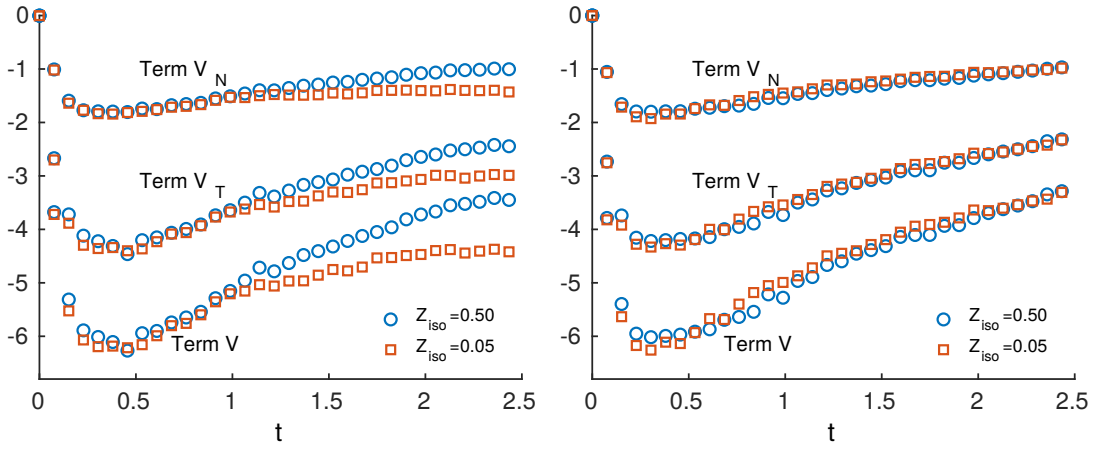

(a) Case A (b) Case B

Figure 3.7: Time evolution of Term V and its components in Equation (3.5), V_N and V_T, for iso-surfaces at $Z_{\text{iso}} = 0.5$ (circles) and $Z_{\text{iso}} = 0.05$ (squares).

surface motion (toward or away from the oxidizer, respectively); the sign of $\langle w \rangle_s$ for $Z_{\text{iso}} > \overline{Z}$ has been reversed in order to highlight the symmetric nature of the diffusion velocity about $\overline{Z}$ (denoted in Figure 3.8 with an asterisk).

For the iso-surfaces plotted in Figure 3.8 (except for $Z_{\text{iso}} = 0.5$), $\langle w \rangle_s$ increases sharply until $t \simeq 0.5$ as the scalar field adjusts to the flow. Once the scalar field has adjusted to the turbulent flow, the diffusion velocity appears to be relatively constant in time. The magnitude of $\langle w \rangle_s$ increases for iso-surfaces moving away from $\overline{Z}$, which is consistent with previous results [94, 28]. The distribution of the initial scalar field does not qualitatively affect the overall behavior of $\langle w \rangle_s$, although Case A exhibits greater values of the mean displacement speed, especially for $Z_{\text{iso}} = 0.05$ and 0.95.

For the iso-surface corresponding to $Z_{\text{iso}} = 0.5$, $\langle w \rangle_s$ is close to zero throughout the simulation. This behavior is consistent with a one-dimensional laminar mixing layer, where the point associated with $\overline{Z}$ is stationary throughout the diffusion process. In the presence of turbulent motions, however, it is expected that local fluctuations in the scalar field could cause the $Z_{\text{iso}} = 0.5$ iso-surface to propagate in response. This is demonstrated in Figure 3.9, where the rms value of the iso-surface averaged diffusion

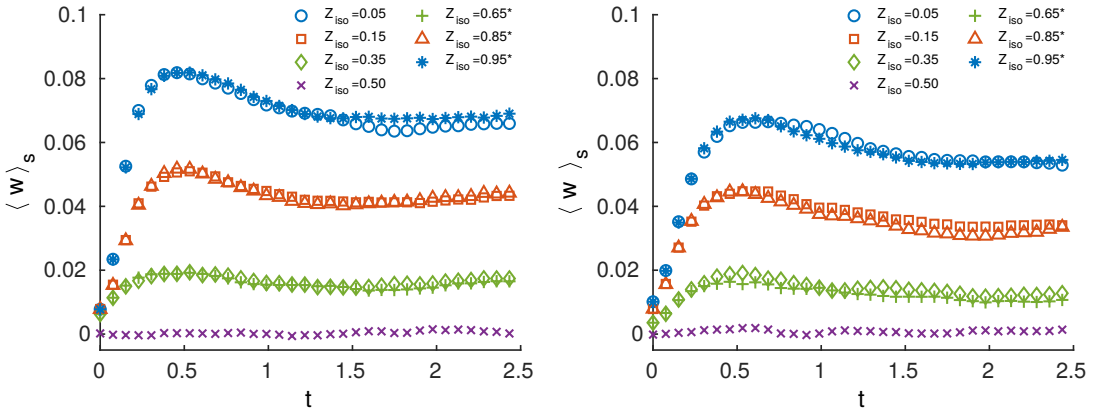

(a) Case A (b) Case B

Figure 3.8: Time evolution of the surface-averaged diffusion velocity, $\langle w \rangle_s$. Values of Z_{iso} with an asterisk have been reflected about 0 to highlight the symmetry.

velocity, $w_{\text{rms}} = \left(\langle w^2 \rangle_s \right)^{1/2}$, is plotted vs time. After a rapid increase during the adjustment period, w_{rms} peaks at $t = 0.5$ and then decays for all iso-surfaces. Clearly, the $Z_{\text{iso}} = \overline{Z}$ iso-surface takes on a non-zero diffusion velocity throughout the domain, but the direction of the diffusion is distributed equally towards the fuel or towards the oxidizer (i.e., equal amounts of positive and negative values) such that it averages to zero.

Extreme values of Z_{iso} are associated with larger values of w_{rms}, but all iso-surfaces exhibit similar behavior throughout the simulation time. It should be noted that the rms values are large compared to the average values. It is also observed that the shape of w_{rms} is similar for both Cases A and B, suggesting that both surfaces respond to local fluctuations of the scalar field in a similar manner.

In Figure 3.10, the surface-averaged mean curvature, $\langle \nabla \cdot \mathbf{n} \rangle_s$, is plotted as a function of time and Z_{iso}. The mean curvature can take on both positive and negative values if the iso-surface is convex towards the oxidizer or fuel, respectively. As in Figure 3.8, the mean curvature exhibits symmetry around $\overline{Z}$, which is highlighted by an asterisk in Figure 3.10. It should be noted that the mean curvature in Case A is

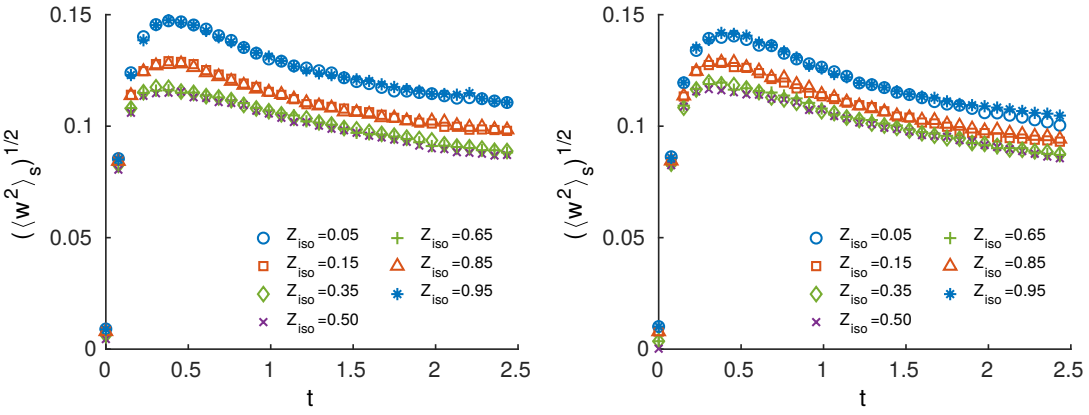

(a) Case A (b) Case B

Figure 3.9: Time evolution of $w_{\text{rms}} = \left(\langle w^2 \rangle_s \right)^{1/2}$ for different iso-surfaces for a) Case A and b) Case B.

non-zero at $t = 0$, but its initial value is trivial compared to the curvature produced by the turbulent motions. The initial field in Case B has zero curvature at $t = 0$ for all iso-surfaces.

Interestingly, the mean curvature increases gradually with time, rather than increasing sharply at the beginning of the simulation (as was found for most other quantities thus far). The variation of the mean curvature with Z_{iso} is consistent with previous studies [94, 36]. For $Z_{\text{iso}} = \overline{Z}$, the curvature fluctuates around zero throughout the simulation, whereas the values of Z_{iso} farthest from $\overline{Z}$ have the largest values of curvature. Qualitatively, both Case A and Case B behave similarly with time, but Case A takes on significantly larger values of $\langle \nabla \cdot \mathbf{n} \rangle_s$ during the simulation, especially the iso-surfaces far from $\overline{Z}$.

The mean curvature of the $Z_{\text{iso}} = \overline{Z}$ iso-surface is approximately zero throughout the simulation, despite the surface exhibiting significant curvature (as demonstrated visually in Figure 3.1). This is explained by examining the rms values of the curvature for each iso-surface, $(\langle (\nabla \cdot \mathbf{n})^2 \rangle_s)^{1/2}$, which are plotted in Figure 3.11. Notably, the $Z_{\text{iso}} = 0.5$ iso-surface experiences significant fluctuations in curvature due to the

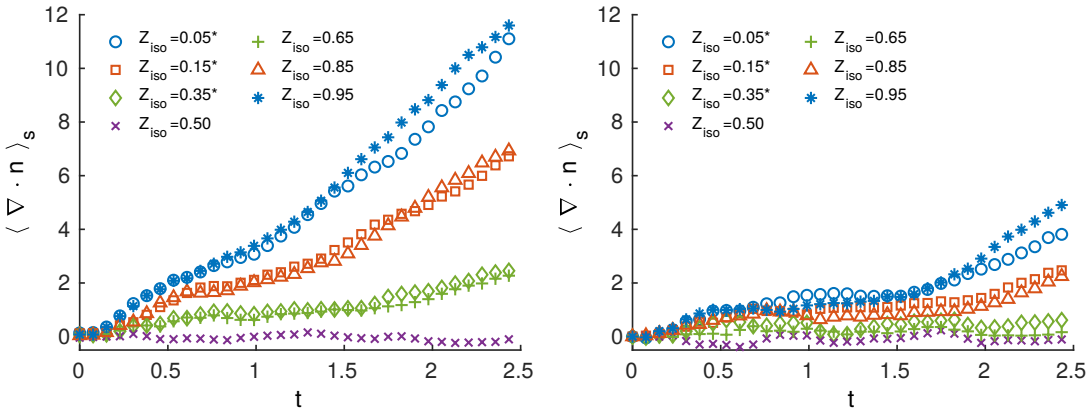

(a) Case A

(b) Case B

Figure 3.10: Time evolution of $\langle \nabla \cdot \mathbf{n} \rangle_s$ for a) Case A and b) Case B. Note that the values of Z_{iso} marked with an asterisk have been reflected about 0 to highlight symmetry.

turbulent velocity field, but the variations have no preferential orientation, resulting in a mean curvature of zero. It should also be noted that the values of the rms curvature are significantly larger than the mean values, indicating large variations of curvature across the iso-surface. This result is consistent with the pdf of surface curvature presented in Dopazo et al. [28] which exhibits significant variability in curvature magnitude.

Figure 3.11 is strongly tied to Term V_T in Equation (3.5) above, which is an important factor in the destruction of iso-surface density. The data presented here shows that the rms curvature increases steeply at early times, despite the mean curvature changing only slightly over this range. Once the flow has adjusted, the rms curvature decays in time at a similar rate as the rms velocity. It should also be noted that Case A and B exhibit similar behavior, particularly for the $Z_{\text{iso}} = \overline{Z}$ iso-surface. It is thought that when a turbulent eddy interacts with the scalar iso-surface, it generates surface curvature proportional to the lengthscale of the eddy; because the smallest eddies dissipate most quickly, the average lengthscale of turbulent eddies increases

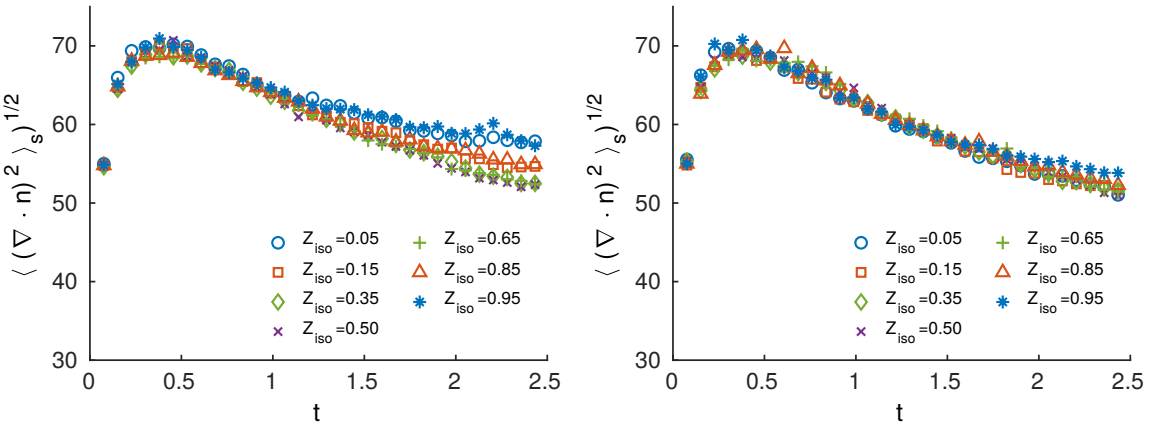

(a) Case A (b) Case B

Figure 3.11: Time evolution of rms curvature, $(\langle(\nabla \cdot \mathbf{n})^2\rangle_s)^{1/2}$, for a) Case A and b) Case B.

over time, therefore causing a reduction in the mean curvature.

Around $t = 1.25$ in Case A, the rms curvature of iso-surfaces far from $\overline{Z}$ begin to decay at a slower rate than for $Z_{\text{iso}} = \overline{Z}$. This suggests that there is an additional contribution to the rms curvature apart from the turbulent eddies distorting the surface. Dopazo et al. [28] derived a transport equation for surface curvature, and found that there are effects due to the velocity field as well as 'added' effects from molecular diffusion (or chemistry, for reacting flows), and that contributions from the added effects tend to dominate contributions from the flow field. In the present simulations, it seems that the flow effects dominate the rms curvature at early times, but the added effects become more dominant at later times as the scalar field mixes. This effect is not observed to the same extent in Case B, which shows very little dependence on Z_{iso}.

Chapter 4

ISO-SURFACE AREA DENSITY IN A TEMPORAL MIXING LAYER

In § 2.3, it was established that both the velocity and scalar fields of the temporal mixing layer simulated for this chapter exhibit a robust period of self-similarity beginning at $t\Delta U/h_0 \approx 250$. This chapter will explore the statistics of the passive scalar iso-surfaces embedded within the flow. Because the scalar field simulated here is passive and not coupled, for example, to the flow dynamics nor the fluid chemistry, there is no 'preferred' scalar iso-surface to analyze; rather than focus on a single iso-surface of chemical or dynamical importance (i.e., the flame surface or T/NT interface), a wide range of iso-surfaces available in the flow will be examined. This is intended to give a somewhat broad characterization of these iso-surface behaviors in this turbulent flow. In total, the statistics of 21 iso-surfaces have been examined, ranging from $0.01 \leq \Phi_{\text{iso}} \leq 0.99$. For clarity, the following figures will only contain data from a small but representative subset of these iso-surfaces, $\Phi_{\text{iso}} = (0.05, 0.25, 0.5, 0.75, 0.95)$. Note that the passive scalar in the temporal mixing layer is denoted as Φ in this chapter and the next, to delineate the temporal mixing layer from the homogeneous, isotropic turbulence discussed in the previous chapter.

4.1 Iso-surface area

The iso-surface area, A_{iso}, computed using the algorithm described in Appendix A and normalized by the initial iso-surface area, $A_0 = L_x L_z$, is shown in figure 4.1 as a function of time for five different values of Φ_{iso}. The iso-surface areas can be seen to increase steeply during the early simulation times, which is consistent with

the behavior of the scalar dissipation rate (figure 2.5) during the growth of unstable modes and subsequent transition to turbulence. In contrast to the scalar dissipation rate, however, the surface areas do not asymptote to constant values once the flow has transitioned to turbulence; on average, A_{iso} continues to increase throughout the self-similar period for all iso-surfaces examined. Iso-surface area is also shown to depend strongly on the value of Φ_{iso}, with the largest values of A_{iso} occurring for $\Phi_{\text{iso}} = 0.5$. This corresponds to the central region of the mixing layer where the peak values of fluctuating velocities exist (see figure 2.7). For iso-surfaces toward the outside of the mixing layer, where Φ_{iso} approaches values of 0 or 1, the surface area was found to be less than half of the surface area at $\Phi_{\text{iso}} = 0.5$. From the symmetry of the problem, the iso-surfaces should exhibit symmetry about $\Phi_{\text{iso}} = 0.5$, that is, the iso-surfaces of Φ_{iso} and $1 - \Phi_{\text{iso}}$ should have equivalent behavior. Therefore, the iso-surfaces for $\Phi_{\text{iso}} = 0.05$ and 0.95 should behave the same, as should the iso-surfaces for $\Phi_{\text{iso}} = 0.75$ and 0.25. Differences in the corresponding curves give some indication of the statistical scatter of the results.

Some qualitative insight into the temporal development of the iso-surface area can be achieved by visual inspection of the iso-surface. In figure 4.2 is shown the iso-surface $\Phi_{\text{iso}} = 0.95$ towards the beginning a) and end b) of the self-similar evolution of the flow. Several observations can be made regarding the development of the iso-surface. First, the surface can be seen to translate in the $+y$ direction, as expected from the linear increase in the mixing layer width, h, during self-similar development. Second, it might be observed that on average, the size of the 'bubbles' or protrusions that comprise the dominant features of the iso-surface have increased during the self-similar period. This is also expected, since the characteristic scales of the velocity and scalar field are known to increase over time (see figure 2.6b). A final observation, related to the increase in the characteristic size of surface features, is that the *extent* of the iso-surface has increased in the y direction. That is, the range of y values over which the surface is present has increased. This is thought to be due, once again,

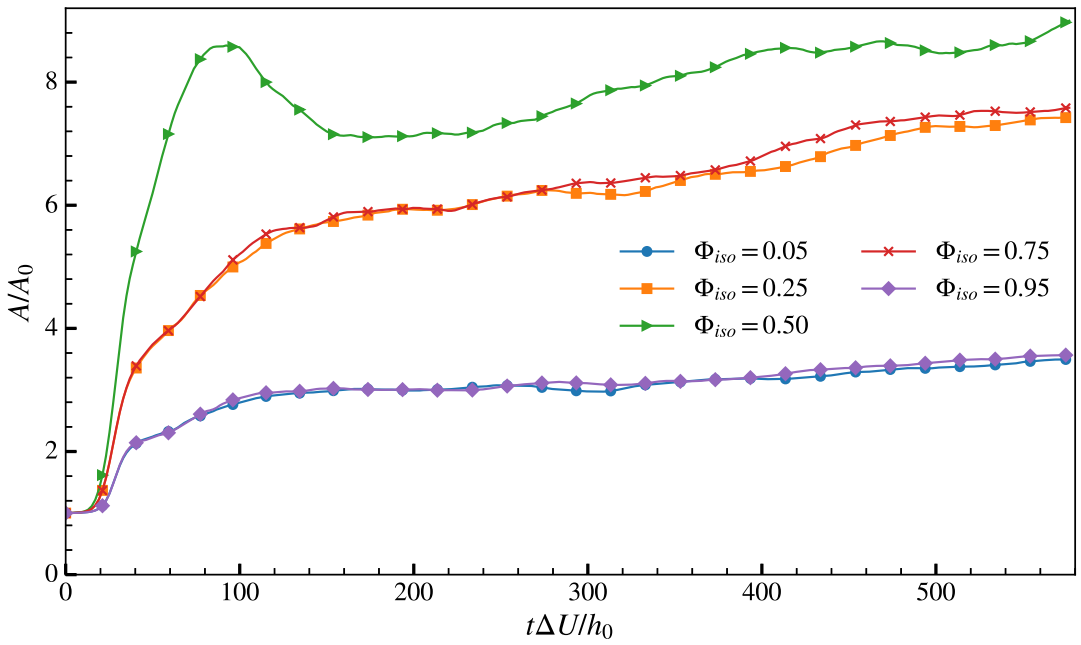

Figure 4.1: Temporal evolution of iso-surface area, A_{iso}, normalized by initial area, A_0, for several values of Φ_{iso}. Due to the problem symmetry, iso-surface evolution is mirrored around $\Phi_{\text{iso}} = 0.5$, i.e. $A_{\Phi_{\text{iso}}} = A_{1-\Phi_{\text{iso}}}$.

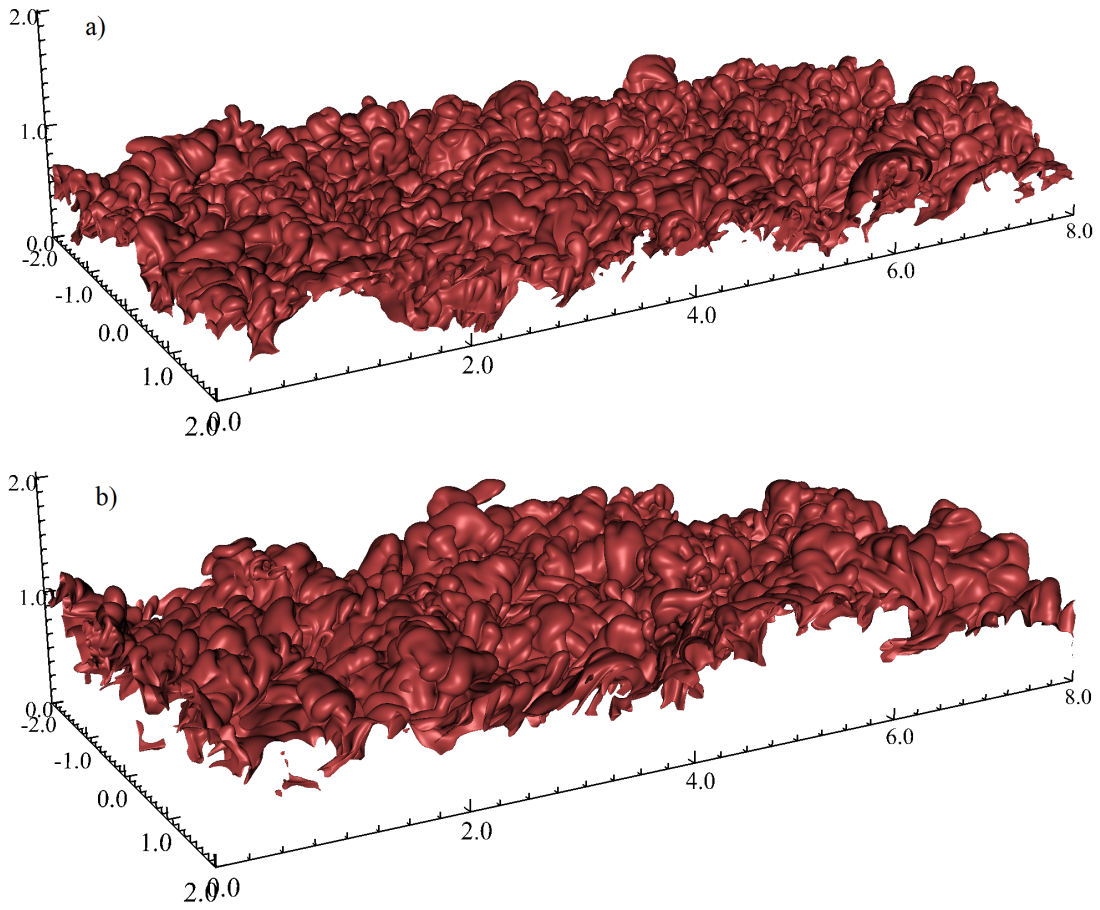

Figure 4.2: Three-dimensional visualization of the $\Phi_{\text{iso}} = 0.95$ iso-surface at (a) $t\Delta U/h_0 = 250$ and (b) $t\Delta U/h_0 = 580$.

to the increase of large scale motions that are on the order of the mixing width, h. In particular, fluid motions that are responsible for engulfing ambient fluid and transporting it to the center of the mixing layer create large surface features in the cross-stream direction on the order of the mixing layer width.

The above observations regarding the complexity and multi-faceted nature of the growth and development of A_{iso} during the self-similar period clearly require additional investigation to properly understand and characterize the temporal evolution. The aim of subsequent analysis of the iso-surface area is to consider both why the

surface area increases, and the rate at which the area increases during the self-similar period of the mixing layer.

4.2 Iso-surface area density

In this section, the evolution of the average iso-surface area density, $\Sigma(y,t)$ (as defined in equation 2.42), is considered during the period of self-similar development. Instantaneous, cross-stream profiles of Σ are shown in figure 4.3 at several times during the self-similar development for two separate iso-surfaces, $\Phi_{\text{iso}} = 0.5$ (4.3a) and $\Phi_{\text{iso}} = 0.95$ (4.3b). The iso-surface area density appears to take a roughly Gaussian shape and, for $\Phi_{\text{iso}} = 0.5$ in figure 4.3a, there is a monotonic trend for the peak value to decrease and the width of the curve to increase. This is true for figure 4.3b as well, with the added trend of the peak translating in the positive y direction. This translation in the y direction is expected to occur as the width of the mixing layer increases, and can also be observed as a slight translation in the $+y$ direction in figure 4.2.

Analysis of Σ is complicated by the fact that the characteristics of Σ (i.e., the peak value Σ_m, the location of the peak y_m, and the width σ) depend not only on time but also on the value of Φ_{iso}. The temporal development of these three characteristics during the self-similar period are plotted in figure 4.4 for the same values of Φ_{iso} as in figure 4.1.

A couple of important observations can be concluded from figure 4.4. First, despite the differences between the temporal development of $\Sigma(y,t)$ for distinct iso-surfaces, the temporal variation of their characteristics, Σ_m, y_m, and σ, are similar for all the surfaces computed. For example, in figures 4.4b and c, the values of y_m and σ evolve in an approximately linear fashion (neglecting statistical noise in the measurements) for the iso-surfaces shown, $0.05 \leq \Phi_{\text{iso}} \leq 0.95$. Additionally, the symmetry around $\Phi_{\text{iso}} = 0.5$ observed previously for the iso-surface areas (see figure 4.1) also holds for the iso-surface area density; values of Σ_m and σ are very similar between symmetric

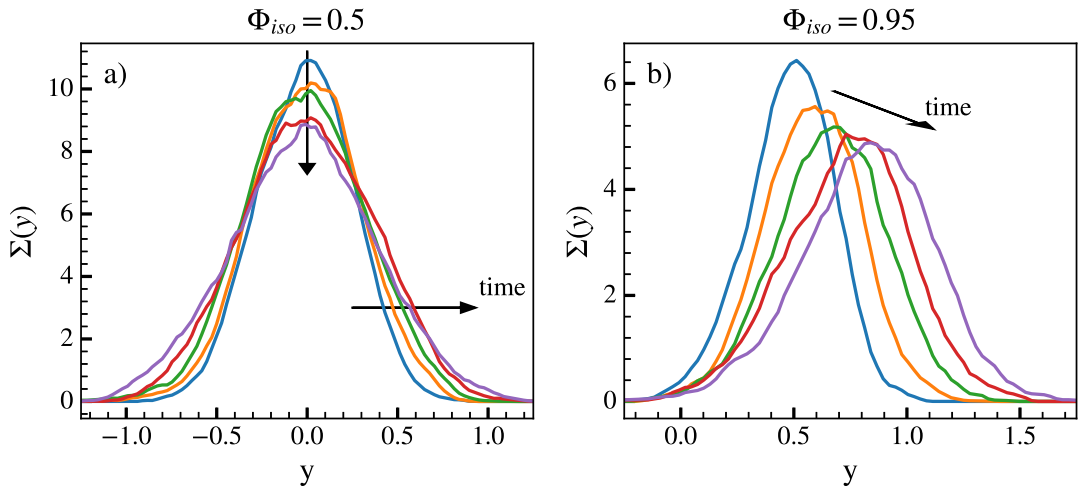

Figure 4.3: Unscaled cross-stream profiles of $\Sigma(y,t)$ throughout the self-similar period of the mixing layer for a) $\Phi_{\text{iso}} = 0.5$ and b) $\Phi_{\text{iso}} = 0.95$.

iso-surfaces (i.e., Φ_{iso} and $1-\Phi_{\text{iso}}$), and the location of the peak, y_m, is mirrored around the centerline for symmetric iso-surfaces. Understanding how these characteristics of $\Sigma(y,t)$ evolve in time and space is of central importance because their development is clearly linked to the temporal development of the mixing layer, which in turn affects the iso-surface area.

The peak location of an iso-surface y_m, shown in Figure 4.4b, is expected to translate in the $\pm y$ directions as the mixing layer widens over time, as observed in Figure 4.3. This translation is therefore related to the linear increase of the mixing layer width h, which is supported by the approximately linear increase of y_m during the self-similar period of evolution. The width of the Σ profiles, as shown in figure 4.4c, also increases linearly in time, suggesting that the profile width σ is also related to h. It is thought that, for any particular iso-surface, σ is related to the extent of the iso-surface in the y direction (as discussed qualitatively in § 4.1 above) and is created in part by large-scale engulfment events. These events, which are responsible for

entraining ambient fluid from outside the mixing layer towards its center, are capable of creating surface features on the order of the mixing layer width. This also helps to explain the area increase over time. Finally, the peak value, Σ_m, is shown to decrease in time during the self-similar period. This is an interesting finding due to the fact that the integral of Σ_{iso} (i.e., the surface area) was found to increase over this period. This suggests that Σ_m is decaying more slowly than σ is increasing, resulting in a net increase of A_{iso}. From a physical perspective, Σ_m is expected to be related to the complexity of the iso-surface; larger values of Σ_m correspond to smaller characteristic scales of the interface, resulting in a more complicated surface with increased area. There is some evidence that the lengthscale defined by Σ_m may be proportional to the wrinkling length in the Bray-Moss-Libby model for flame surface density [10, 46].

Based on the linear trend of y_m and σ, along with the linear growth rate of h, it was found that y_m/h and σ/h are essentially constant during the self-similar period for the entire range of surfaces computed, with iso-values ranging between $0.01 \leq \Phi_{\text{iso}} \leq 0.99$. Additionally, it was determined empirically that the peak value of Σ, normalized by the scalar Taylor scale λ_ϕ, is approximately constant throughout the self-similar period for the entire range of iso-values. These empirical findings suggest that Σ develops in a self-similar manner along with the mixing layer such that

$$\Sigma(y,t) = \Sigma_0(t)\hat{\Sigma}(\xi), \tag{4.1}$$

where $\xi = y/h$ is the same similarity variable defined above for the velocity and scalar fields, and $\Sigma_0(t) \propto \lambda_\phi^{-1}$. Normalized cross-stream profiles of Σ, scaled with λ_ϕ, are displayed in figure 4.5a for $\Phi_{\text{iso}} = 0.5$ and 4.5b for $\Phi_{\text{iso}} = 0.95$. Dashed, colored lines represent instantaneous profiles throughout the self-similar region, with the solid black line corresponding to a time average of the instantaneous profiles. These data demonstrate an excellent collapse of the iso-surface area density profiles due to the considerable amount of overlap when plotted against the normalized coordinates, and indicate that the profiles evolve in a self-similar manner that is consistent with the

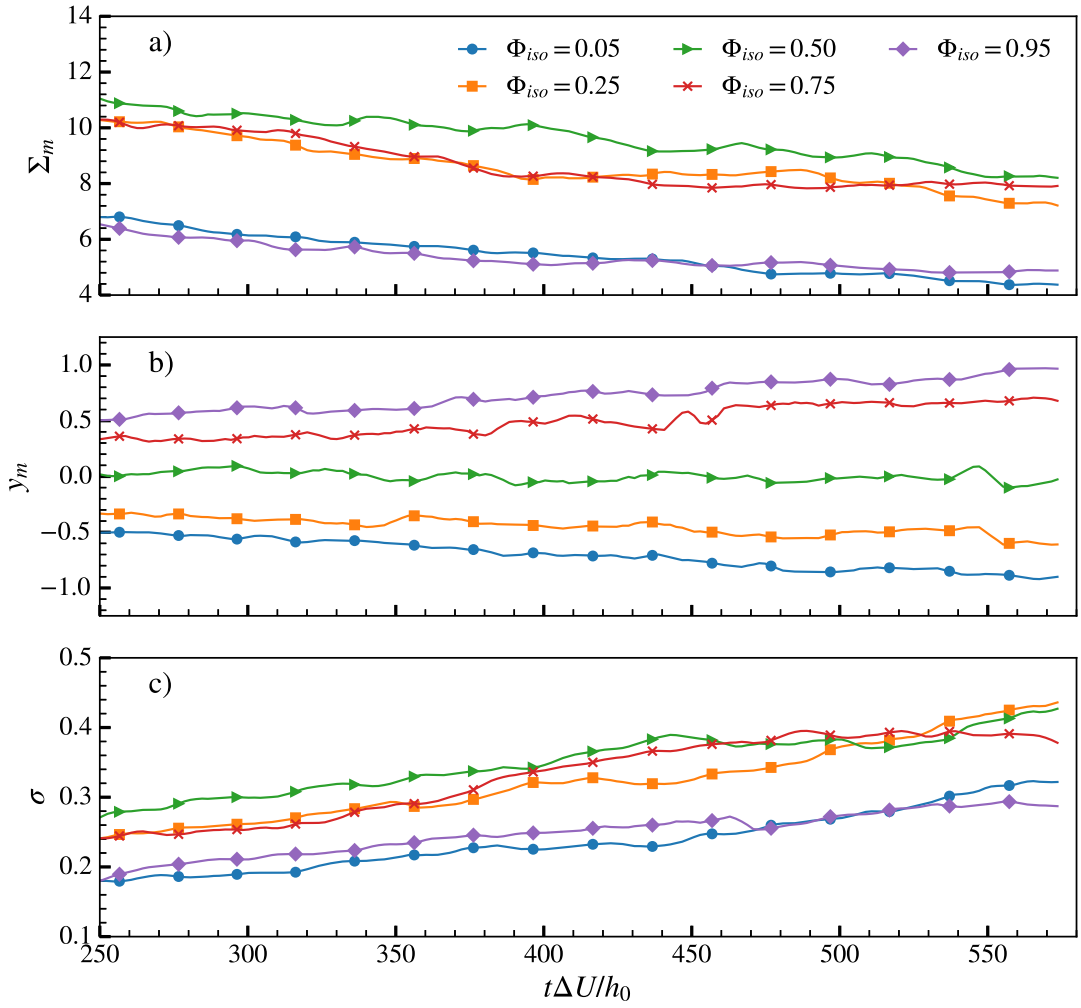

Figure 4.4: Temporal development of unscaled $\Sigma(y,t)$ characteristics during the self-similar period: a) peak value Σ_m, b) location of peak value, y_m, and c) characteristic width, σ, for several values of Φ_{iso} as in figure 4.1.

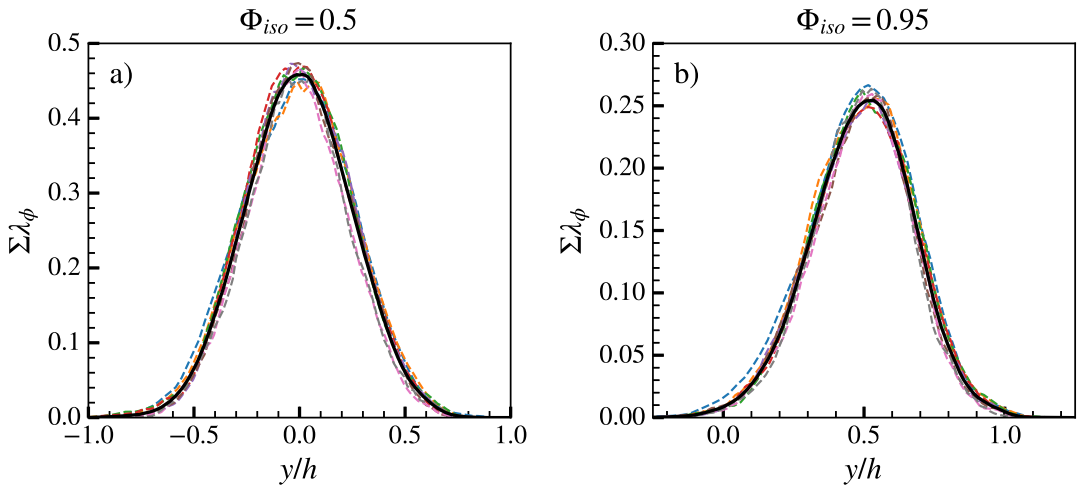

Figure 4.5: Instantaneous y profiles of Σ (dashed lines), normalized by λ_ϕ, for a) $\Phi_{\text{iso}} = 0.5$ and b) $\Phi_{\text{iso}} = 0.95$. Solid lines represent averages of $\Sigma\lambda_\phi$ over the self-similar period.

velocity field. It is particularly interesting to note that the scaling applies to a wide range of iso-values, despite the temporal variation of the peak location. As suggested by Figure 4.5b, the non-dimensional location of the peak value, y/h, is constant throughout the self-similar region.

The introduction of the Taylor length scale to the self-similar scaling of Σ is anomalous compared to typical scaling relations for the velocity and scalar fields (and the corresponding dissipation rates), which scale with the velocity difference, ΔU, scalar difference, $\Delta\Phi$, and mixing width, h. To gain a deeper understanding of the relationship between Σ and λ_ϕ, a rough, order-of-magnitude scaling argument is developed here that suggests a direct link between the two.

Consider again the definition of the mean iso-surface area density Σ from (1.8) as the probability average of $|\nabla\Phi|\delta(\Phi - \Phi_{\text{iso}})$. The following analysis can be simplified by neglecting the $\delta(\Phi - \Phi_{\text{iso}})$ term, which removes the iso-surface dependence from the scaling argument. It is clear that the properties of Σ depend strongly on Φ_{iso} (see

figure 4.4), yet the scaling of these parameters appears to be similar over a wide range of iso-values. This is demonstrated in figure 4.5 in that despite $\Sigma_{\Phi_{\text{iso}}=0.5}$ and $\Sigma_{\Phi_{\text{iso}}=0.95}$ taking on distinct profiles, they are both scaled similarly by λ_ϕ and h. Removing $\delta(\Phi - \Phi_{\text{iso}})$ from Σ' yields the following result for Σ,

$$\Sigma \sim \langle |\nabla \Phi| \rangle \,, \tag{4.2}$$

which is a common simplification when considering the premixed flame surface (referred to as the *generalized* surface area density [9]). Σ can be related to the scalar dissipation rate (Equation (2.40)) by noting that

$$\Sigma \sim \left\langle \frac{\chi}{2D} \right\rangle^{1/2} \tag{4.3}$$

when χ follows a log-normal distribution [103]. From the definition of the Taylor scale in equation (2.33),

$$\Sigma \sim \left\langle \frac{\chi}{2D} \right\rangle^{1/2} \sim \frac{\phi'}{\lambda_\phi}, \tag{4.4}$$

where $\phi' = \langle \phi^2 \rangle^{1/2}$ is the rms of the fluctuating scalar field. For the mixing layer configuration, ϕ' takes on a self-similar form, and is relatively constant over the width of the shear layer (see figure 2.8a). Based on these observations, it can be argued that the mean iso-surface area density of a passive scalar field in a turbulent mixing layer should scale with the inverse of the scalar Taylor scale,

$$\Sigma \sim \lambda_\phi^{-1}. \tag{4.5}$$

Despite the roughness of the scaling argument, when combined with the above data establishing self-similarity of Σ, these results suggest that it does make sense to use λ_ϕ to scale iso-surface area density in the presence of turbulence.

This finding is somewhat contrary to established viewpoints in the literature. For example, studies on the fractal nature of turbulent iso-surfaces [87] suggest that the cutoff scale (i.e., smallest scale associated with an iso-surface) is proportional to the Kolmogorov scale η. In the well-known review article on turbulent mixing by

Dimotakis [27, pg. 340], it is stated that the surface area density should scale as $\Sigma \sim \eta^{-1}$. While there is not enough scale separation between λ_ϕ and η in the present results to conclusively demonstrate that Σ does *not* scale with η, it seems plausible from the data above and the rough scaling argument to reasonably suggest some dependence on λ_ϕ.

4.3 Implications of self-similarity and the Taylor scale

Although a thorough knowledge of $\Sigma(y,t)$ is necessary to understand the fundamental behavior of an iso-surface in a turbulent flow, the desired output in many engineering applications is the surface area $A(t)$. Based on (4.5) and using the self-similarity of Σ, the scaling argument discussed above can be extended to include the normalized iso-surface area.

Consider that the normalized iso-surface area is equivalent to the integral of the mean iso-surface area density in the cross-stream direction (see equations (2.41) and (2.42)),

$$\frac{A_{\text{iso}}}{A_0} = \int_{\mathcal{V}} \Sigma' d\mathcal{V} = \int_{-L_y/2}^{L_y/2} \Sigma(y,t) dy, \tag{4.6}$$

where $A_0 = L_x L_z$ is the initial area of a planar iso-surface. Substituting the self-similar form of Σ, defined in equation (4.1), into the above equation and changing variables of the integral yields

$$\frac{A_{\text{iso}}}{A_0} = \int_{-L_y/2}^{L_y/2} \Sigma_0(t)\hat{\Sigma}(\xi) dy \propto \frac{h}{\lambda_\phi} \int_{-L_y/2h}^{L_y/2h} \hat{\Sigma}(\xi) d\xi. \tag{4.7}$$

Because the shape of $\hat{\Sigma}(\xi)$ does not vary, the integral over ξ results in a constant value. Hence, based on the present results, the normalized surface area is expected to scale as

$$\frac{A_{\text{iso}}}{A_0} \sim \frac{h}{\lambda_\phi}. \tag{4.8}$$

Furthermore, turbulence theory [74] suggests that

$$\frac{A_{\text{iso}}}{A_0} \sim \frac{h}{\lambda_\phi} \sim (ReSc)^{1/2}. \tag{4.9}$$

The scaling suggested by (4.8) can be directly tested using simulation data by scaling A/A_0 with λ_ϕ/h. If the scaling is correct, the resulting curve should tend towards a constant value in the self-similar region. In figure 4.6 is plotted the scaled area ratio, $A/A_0(\lambda_\phi/h)$, for the same values of Φ_{iso} as in figure 4.1. During the self-similar period, the scaled area ratio appears to asymptote towards a constant value, although the curves continue to decline slightly. The difference in the scaled area ratio between the beginning and end of the self-similar period is found to be $\leq 10\%$ for iso-surfaces in the range $0.2 \leq \Phi_{\text{iso}} \leq 0.8$.

The variations observed in the scaled area ratio (e.g., the downturn in the area for $\Phi_{\text{iso}} = 0.5$) may be due to a lack of statistical convergence of large-scale flow features at late times in the DNS, as the sample size of eddies on the integral scale naturally decrease during the flow field evolution. The decrease in the scaled area ratio could also be due to finite Reynolds number effects, considering the moderate Re_λ in the present DNS. Finally, any deviations from self-similar behavior would affect the observed scaling.

It is interesting to note that A/A_0 exhibits a smaller decline when scaled by the longitudinal Taylor scale, λ_1/h; the decrease over the self-similar period is $\leq 5\%$ for iso-surfaces in the range $0.2 \leq \Phi_{\text{iso}} \leq 0.8$. In contrast, the decrease in both the unscaled area ratio and when scaled by the Kolmogorov scale (η/h) is $\geq 20\%$ over the same range of Φ_{iso}. Overall, this suggests that, for the DNS presented here, A/A_0 scales approximately with the ratio of lengthscales h/λ_ϕ.

The proper scaling of the iso-surface area in turbulent flows remains an open question in the literature. Recent results from reference [83] of a passive scalar in forced, stationary, homogeneous, isotropic turbulence at very high Reynolds numbers ($Re_\lambda \approx 400$) suggested that $A/A_0 \sim (Re_\lambda Sc)^{1/2}$, although the circumstances of their flow are much different from the present temporally evolving shear layer. In contrast, results from several recent studies of premixed flame surface area have discovered a dependence on the Taylor scale, which lend confidence to the results presented

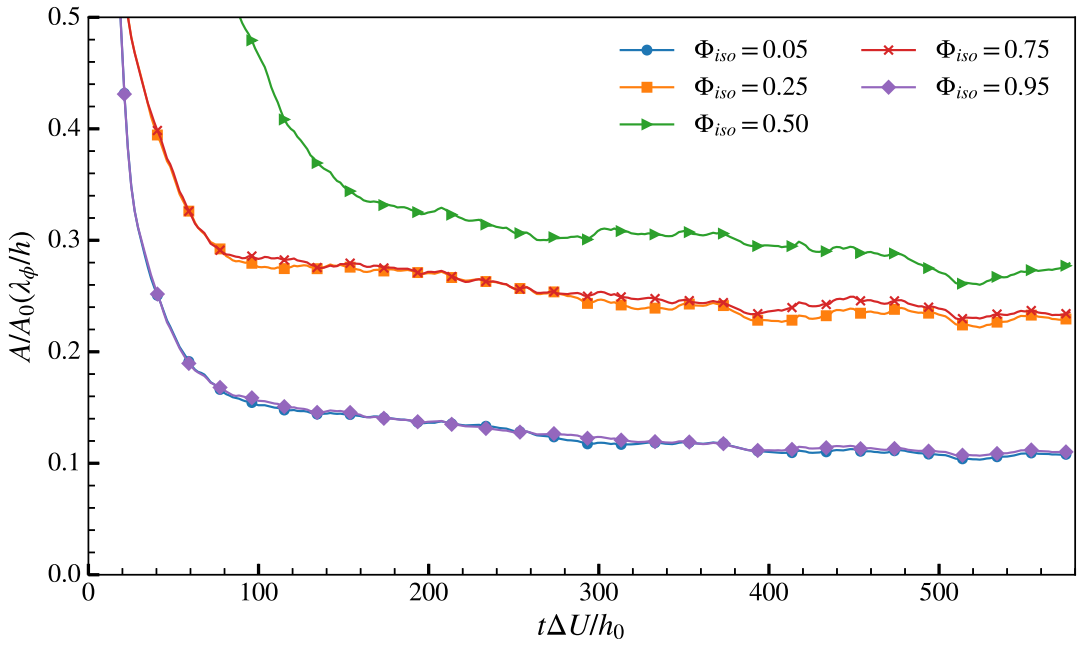

Figure 4.6: Temporal evolution of normalized iso-surface area, A_{iso}/A_0, scaled with the ratio of the Taylor to integral scales, λ_ϕ/h, for several values of Φ_{iso} as in figure 4.1.

here. Driscoll *et al.* [30] found that the use of a Reynolds number based on the Taylor scale was a better marker of regime changes in flamelet behavior than the established criterion involving the Kolmogorov scale. Kulkarni *et al.* [48] studied the development of Σ in spherically expanding flames and found that $\Sigma\ell \sim Re_\lambda^{1.11}$, where ℓ is an integral scale of the flow. Despite significant differences between the two flows, such as variable density and chemical heat release, this scaling is comparable to the present results (recalling that $Re_\lambda \sim Re^{1/2}$ as $Re \to \infty$). These studies, coupled with the present results, suggest that the Taylor length scale may be a key component in determining iso-surface area.

4.3.1 Parameterization of iso-surface area density

Although the normalized profiles of the mean iso-surface area density, $\hat{\Sigma}(\xi)$, have been shown to be approximately constant throughout the self-similar period, the characteristics of the profiles exhibit a strong dependence on the iso-value Φ_{iso}. In particular, the peak value, $\hat{\Sigma}_m$, peak location, ξ_m, and width, $\hat{\sigma}$, are found to be functions of Φ_{iso}. The value of these characteristics are plotted in figure 4.7 for a total of 21 iso-surfaces for a range of values $0.01 \leq \Phi_{\text{iso}} \leq 0.99$.

A simple algebraic model can be constructed for these characteristic features. The peak location, ξ_m, is well-approximated by a linear curve across almost all values of Φ_{iso}, while $\hat{\Sigma}_m$ and $\hat{\sigma}$ appear to have a quadratic dependence on Φ_{iso}, centered around $\Phi_{\text{iso}} = 0.5$. The variation of each of the three terms are estimated with the following equations, which are determined using a least-squares polynomial fit:

$$\hat{\Sigma}_m = -1.05\Phi_{\text{iso}}^2 + 1.05\Phi_{\text{iso}} + 0.21, \tag{4.10}$$

$$\xi_m = 1.2\Phi_{\text{iso}} - 0.59, \tag{4.11}$$

$$\hat{\sigma} = -0.41\Phi_{\text{iso}}^2 + 0.42\Phi_{\text{iso}} + 0.15. \tag{4.12}$$

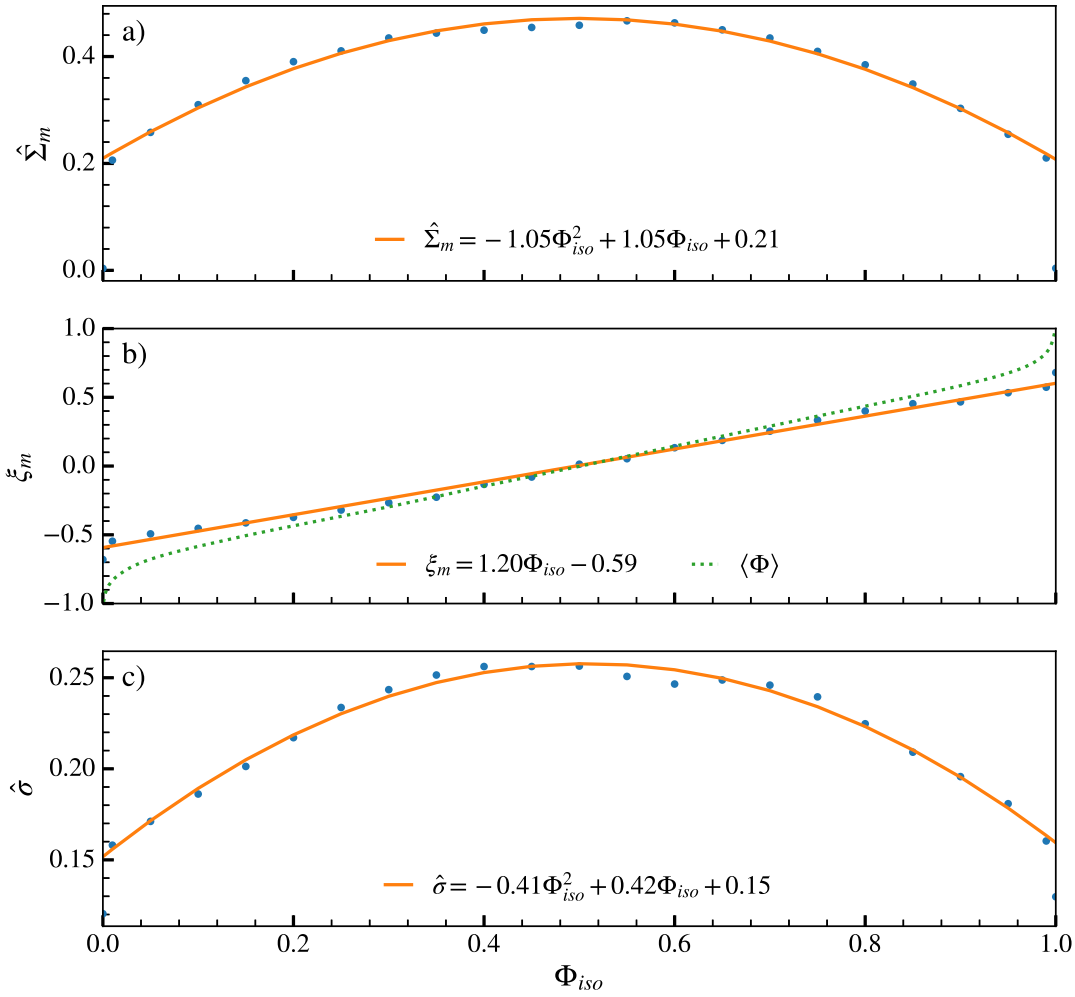

Figure 4.7: Plots of the relevant features of the self-similar profiles of $\hat{\Sigma}(\xi)$, as a function of the isovalue Φ_{iso}: a) peak value $\hat{\Sigma}_m$, b) offset location ξ_m, and c) characteristic width $\hat{\sigma}$. Circles represent data collected from the DNS during the self-simliar region of flow, and solid lines are best-fit approximations using the *polyfit* routine in numpy. The dotted line in b) is the self-similar profile of the mean scalar, $\langle\Phi\rangle(\xi)$.

From inspection, it seems reasonable to assume that the profiles of $\hat{\Sigma}(\xi)$ are approximately Gaussian. Under this assumption, $\hat{\Sigma}$ takes the following form,

$$\hat{\Sigma}(\xi;\Phi_{\text{iso}}) = \hat{\Sigma}_m \exp\left(-\frac{(\xi-\xi_m)^2}{2\hat{\sigma}^2}\right), \tag{4.13}$$

where $\hat{\Sigma}_m$, ξ_m, and $\hat{\sigma}$ depend on the particular value of Φ_{iso}.

Using these modeled parameters, a family of curves for $\hat{\Sigma}(\xi)$ were constructed for a range of iso-values and plotted in figure 4.8, along with the measured profiles calculated from the DNS data. For clarity, only five profiles of $\hat{\Sigma}$ are displayed, although the model given by (4.13) gives similar agreement for any iso-surface chosen.

There is clear agreement between the solid and dashed curves in Figure 4.8, indicating agreement between the measured and approximated profiles of $\hat{\Sigma}$ and suggesting that the Gaussian profile is a good approximation for the self-similar form of the mean iso-surface area density. Iso-surfaces near the boundaries ($\Phi_{\text{iso}} \to 0, 1$) exhibit some skewness that is not accounted for by the modeled parameters. Interestingly, the profiles are skewed towards the center of the shear layer. This is probably due to the fact that the majority of surface area is produced in the middle of the shear layer (where u' and $|\nabla\Phi|$ are greatest), which causes the peaks to skew in that direction.

It is not immediately obvious why the peak location, ξ_m, varies linearly across the range of Φ_{iso}. It might be expected for the location of peak iso-surface area density to correspond with the mean scalar profile, that is, $\xi_m(\Phi_{\text{iso}}) = (y/h)|_{\Phi_{\text{iso}}}$. Indeed, this assumption is approximately correct for the range of iso-values $0.2 \leq \Phi_{\text{iso}} \leq 0.8$, as shown in figure 4.7b. The dotted line represents the mean scalar profile and is shown to agree with ξ_m in the interior portion of the mixing layer. However, the values of ξ_m deviate from the profile of $\langle\Phi\rangle$ near the outer boundaries. This deviation can be explained by the same phenomena that explains the non-Gaussian behavior in $\hat{\Sigma}$, which is that the production of iso-surface area is greatest in the center of the shear layer and could cause the peak location to skew towards $y = 0$. This may also help to explain the quadratic dependence of $\hat{\Sigma}_m$ and $\hat{\sigma}$, which peak at the centerline of the

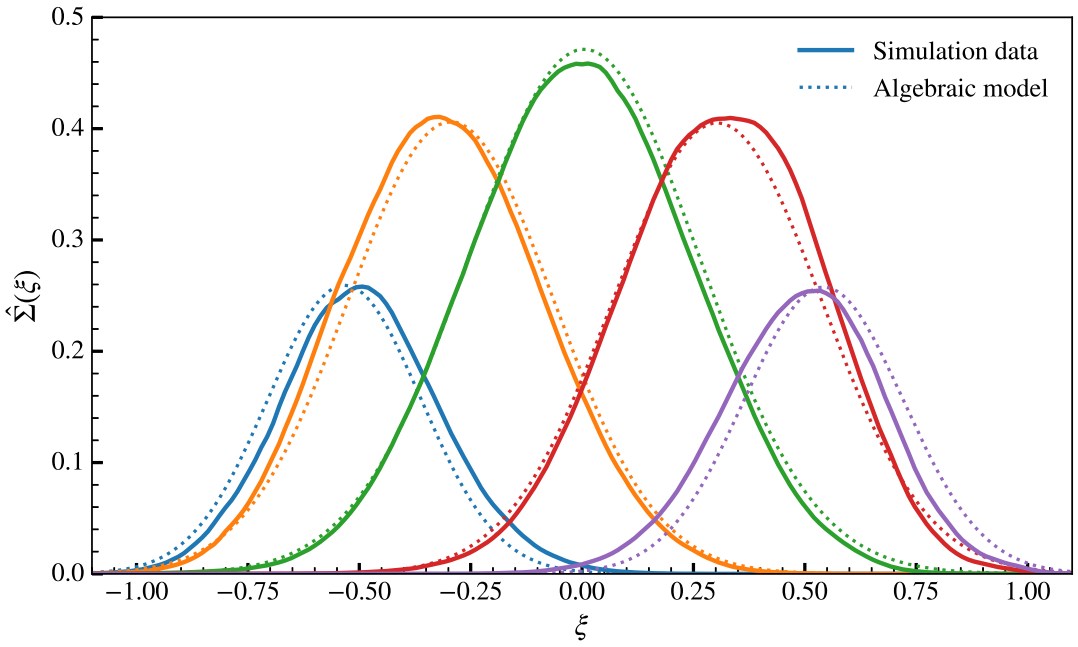

Figure 4.8: Profiles of $\hat{\Sigma}$ from the DNS (solid lines) compared to the Gaussian model given by (4.13) (dashed lines) for $\Phi_{\text{iso}} = 0.05, 0.25, 0.5, 0.75$, and 0.95 (from left to right).

mixing layer where the strongest turbulent fluctuations occur.

Chapter 5

ON THE TRANSPORT AND EVOLUTION OF ISO-SURFACE AREA DENSITY IN A TEMPORAL MIXING LAYER

This chapter is an extension of the analysis performed in the previous chapter, focusing on the evolution equation for Σ and examining the self-similar behavior of each term in the equation. As in the previous chapter, the simulation used for this study is a temporally developing mixing layer, the details of which are described in § 2.2. In S 5.1, the numerical methods used to evaluate surface averages are evaluated by demonstrating good agreement between the direct measurement of $\partial\Sigma/\partial t$ and the sum of the terms in its evolution equation. Self-similar scalings for each term in the evolution equation are presented in § 5.2 along with physical arguments that may explain the observed self-similar scaling. Finally, § 5.3 summarizes the key results and discusses possible implications of the scalings observed for modeling the rate of change of Σ.

Note that this chapter uses distinct notation for the terms in the iso-surface evolution equation, in part to distinguish the present results from those from the homogeneous turbulence in Chapter 3, as well as for additional clarity over the numbering system.

5.1 Balancing the iso-surface transport equation

In the following section, the evolution of iso-surface area, A_{iso}, and iso-surface area density, Σ, will be examined. In particular, it will be demonstrated that direct measurements of dA_{iso}/dt and $\partial\Sigma/\partial t$ are in close agreement with the rates of change

implied from the transport equations.

5.1.1 Iso-surface area

Consider the integral of equation (1.9) over the cross-stream direction,

$$\frac{\partial}{\partial t}\int_{-Ly/2}^{Ly/2}\Sigma\ dy = -\int_{-Ly/2}^{Ly/2}\langle n_i n_j S_{ij}\rangle_s\,\Sigma\ dy + \int_{-Ly/2}^{Ly/2}\left\langle w_{\rm iso}\frac{\partial n_i}{\partial x_i}\right\rangle_s\Sigma\ dy, \qquad (5.1)$$

where the convective and diffusive transport terms ($\mathcal{T}_U$ and $\mathcal{T}_D$) are identically zero due to the zero flux boundary conditions, the production term ($\mathcal{P}$) has been simplified for constant density flow, and the time derivative in $\partial\Sigma/\partial t$ has been moved outside the integral. From (2.44), it can be shown, by integrating over the entire domain in y, that the above equation describes the rate of change of iso-surface area, $dA_{\rm iso}/dt$, normalized by the surface area of a plane in the x, z direction, $A_0 = L_x L_z$. According to (5.1), the rate of change of iso-surface area is determined by the difference between the production term, $\mathcal{P}$, which is given by the flow strain-rate, and the destruction term, $\mathcal{D}$, which is a combination of molecular diffusion and curvature effects, i.e., $dA_{\rm iso}/dt = A_0(\mathcal{P}-\mathcal{D})$.

The temporal evolution of $dA_{\rm iso}/dt$, $\mathcal{P}$, and $\mathcal{D}$ in (5.1) are plotted in figure 5.1 for $\Phi_{\rm iso} = 0.5$ and 0.95 in panels a and b, respectively. $dA_{\rm iso}/dt$ is estimated directly from DNS data by taking a time derivative of $A_{\rm iso}$. This estimate agrees well with the rate of change implied from the sum of terms $\mathcal{P}$ and $\mathcal{D}$ (c.f., blue circles to red dotted line) during the self-similar period for both of the iso-surfaces shown. Despite the fact that $\Delta x/\eta < 2.1$ throughout the DNS, there is some discrepancy between the left- and right-hand sides of the transport equation during the transition to turbulence, when the smallest lengthscales are present in the flow. For the present DNS, the best agreement between the predicted and measured value of $dA_{\rm iso}/dt$ is found to be for $\Delta x/\eta < 1.5$.

The steep growth of $A_{\rm iso}$ during the transition to turbulence can be identified in figure 5.1 as a small peak in the evolution of $dA_{\rm iso}/dt$ when $t\Delta U/h_0 < 100$, but

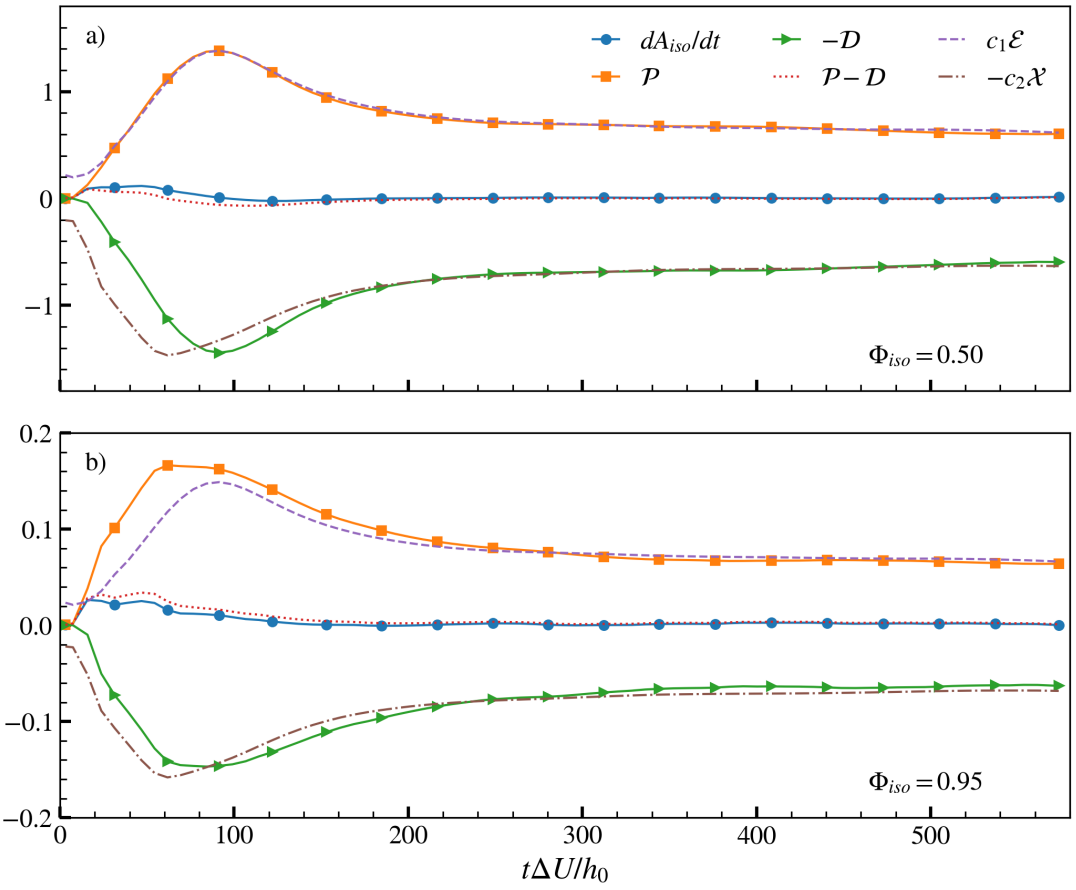

Figure 5.1: Temporal evolution of terms in the iso-surface area transport equation, equation (5.1), for a) $\Phi_{\text{iso}} = 0.5$ and b) $\Phi_{\text{iso}} = 0.95$. dA_{iso}/dt is given by circles, term $\mathcal{P}$ by squares, term $\mathcal{D}$ by triangles, and the sum of terms $\mathcal{P}$ and $\mathcal{D}$ is given by the dotted line. Additionally, the integral dissipation-rates of kinetic energy and scalar variance, $\mathcal{E}$ and $\mathcal{X}$, have been scaled by constant values to approximately match the production and destruction terms and are plotted as dash and dash-dot lines, respectively. Note the difference in scales between panels a) and b).

more clearly as a steep increase in the magnitude of both terms $\mathcal{P}$ and $\mathcal{D}$. In this transitional period, the magnitude of term $\mathcal{D}$ lags slightly behind term $\mathcal{P}$, resulting in the initial growth of surface area.

Notably, the evolution of terms $\mathcal{P}$ and $\mathcal{D}$ are approximately proportional to the integrated dissipation-rates of turbulent kinetic energy and scalar variance, defined as

$$\mathcal{E} = \frac{1}{\Delta U^3} \int_{-L_y/2}^{L_y/2} \varepsilon \, dy \tag{5.2}$$

and

$$\mathcal{X} = \frac{1}{\Delta \Phi^2 \Delta U} \int_{-L_y/2}^{L_y/2} \chi \, dy, \tag{5.3}$$

respectively [79, 4].The integrated dissipation rates, $\mathcal{E}$ and $\mathcal{X}$, multiplied by constants c_1 and $-c_2$, respectively, are displayed in figure 5.1 as dash and dash-dot lines. The constant values are chosen empirically to highlight the similarity between the temporal evolution of the integrated dissipation-rates and the rates of production and destruction of iso-surface area and range from values of ≈ 5 to 50.

The similarity between $\mathcal{P}$ and $\mathcal{E}$ is expected from previous models of flame surface area, which typically assume that $\mathcal{P} \sim (\varepsilon/\nu)^{1/2}$ or $\mathcal{P} \sim \varepsilon/k$ (see [71] for an overview). Due to the near-symmetric behavior of the production $\mathcal{P}$ and destruction $\mathcal{D}$, it would suggest that the destruction is also linked to the kinetic energy dissipation-rate, $\mathcal{E}$. The agreement between $\mathcal{P}$ and $\mathcal{E}$ for the iso-surface $\Phi_{\text{iso}} = 0.5$ is almost uncanny, and demonstrates just how good this approximation can be. In the present DNS, it appears that there is a strong relationship between the scalar dissipation-rate $\mathcal{X}$ and both the production and destruction of iso-surface area. Interestingly, for $\Phi_{\text{iso}} = 0.95$, there is better qualitative agreement between $\mathcal{D}$ (and therefore, $\mathcal{P}$) and the scalar dissipation-rate $\mathcal{X}$, particularly for $t\Delta U/h_0 < 100$ during the transition to turbulence.

During the self-similar period ($t\Delta U/h_0 > 250$), the production and destruction terms are significantly larger than their difference, which is consistent with previous studies of iso-surface area transport [36, 8, 46]. In the present study, the difference is so

significant that $dA_{\rm iso}/dt$ appears to go to near zero during the self-similar development. This result presents something of a paradox; if $\mathcal{P}$ and $\mathcal{D}$ are approximately in balance, then there should be no increase in $A_{\rm iso}$ during the self-similar period as suggested by figure 4.1. This discrepancy between the magnitudes of terms $\mathcal{P}$ and $\mathcal{D}$ compared to the remaining terms in (1.9) will be discussed in more detail in the following sections.

5.1.2 Iso-surface area density

Consider now the iso-surface transport equation, equation (1.9), subject to the iso-surface averaging methods discussed in § 2.4. The rate of change of iso-surface area density is determined by convective and diffusive transport as well as the production and destruction of Σ, i.e., $\partial\Sigma(y,t)/\partial t = \mathcal{T}_U + \mathcal{P} + \mathcal{T}_D - \mathcal{D}$. As in the previous section, an estimate of $\partial\Sigma/\partial t$ can be obtained explicitly via a time derivative of Σ, which is compared to the predicted value of $\partial\Sigma/\partial t$ from the sum of the terms on the right-hand side of (1.9). Cross-stream profiles of each term are displayed in figures 5.2a and c at $t\Delta U/h_0 = 462$ for $\Phi_{\rm iso} = 0.5$ and 0.95, respectively. The terms have been non-dimensionalized by the local mixing layer width and the velocity difference across the shear layer ($\Delta U/h^2$). It can be seen that, similar to the results of figure 5.1, $\mathcal{P}$ and $\mathcal{D}$ are significantly larger than the remaining terms in the balance equation. For $\Phi_{\rm iso} = 0.5$, $\mathcal{P}$ and $\mathcal{D}$ are a full order of magnitude larger than $\partial\Sigma/\partial t$.

Rather than plotting $\mathcal{P}$ and $\mathcal{D}$ separately, consider instead the net effect of the production and destruction terms,

$$K = \mathcal{P} - \mathcal{D} = -\left\langle n_i n_j S_{ij} \right\rangle_s \Sigma + \left\langle w_{\rm iso} \frac{\partial n_i}{\partial x_i} \right\rangle_s \Sigma, \tag{5.4}$$

where K has been described in the literature as the 'net surface stretch' [11, 48]. In figures 5.2b and d are plotted the terms in the iso-surface transport equation, but with K in place of $\mathcal{P}$ and $\mathcal{D}$, for the same time and iso-values as in panels a and c. This comparison demonstrates that the difference between the production and destruction terms is on the same order of magnitude as $\partial\Sigma/\partial t$ and the convective

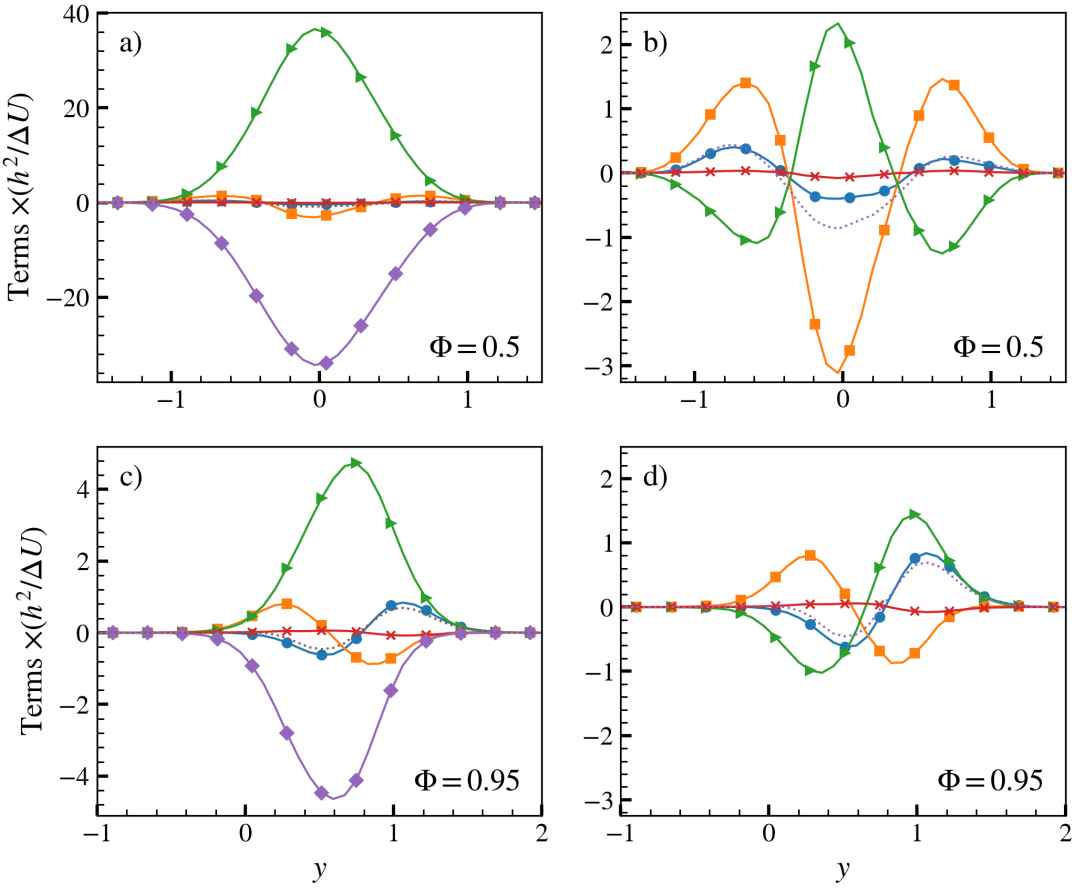

Figure 5.2: Cross-stream profiles of all terms in the iso-surface area density transport equation, equation (1.9), at $t\Delta U/h_0 = 462$ conditioned on a), b) $\Phi_{\text{iso}} = 0.5$, and c), d) $\Phi_{\text{iso}} = 0.95$. In panels a) and c), all terms are plotted separately, with the circles, squares, triangles, diamonds, and x's corresponding to $\partial\Sigma/\partial t$, $\mathcal{T}_U$, $\mathcal{P}$, $\mathcal{T}_\mathcal{D}$, and $\mathcal{D}$, respectively. In panels b) and d), the net effect of production and destruction, $K = \mathcal{P} - \mathcal{D}$ is plotted instead, which is represented as triangles. The dotted line represents the sum of terms $\mathcal{T}_U$, $\mathcal{P}$, $\mathcal{T}_D$, and $\mathcal{D}$, which should approximately match the direct measurement of $\partial\Sigma/\partial t$. Note the difference in scales between panels a) and b) and between c) and d).

transport $\mathcal{T}_U$; the diffusive transport term, $\mathcal{T}_D$, is an order of magnitude smaller still. This has significant implications when estimating the self-similar evolution of each term, as described in the following sections.

Overall, from figures 5.2b and d, there is good agreement between the left- and right-hand sides of equation (1.9) (c.f. circles and dotted line), though the values differ somewhat near $y = 0$ (especially for $\Phi_{\text{iso}} = 0.5$ in panel b). Demonstrating this balance between the measured and predicted values of $\partial\Sigma/\partial t$ lends confidence to both the simulation results and surface integration methodology. Following sections will examine the self-similar scaling and physical interpretation of each of the terms plotted in figure 5.2.

5.2 Self-similarity of transport terms

Based on the robust self-similar behavior of Σ in the present DNS (see figure 4.1), it is expected that the terms in the transport equation for Σ, equation (1.9), will also exhibit self-similarity. Self-similar forms for each of the terms are proposed in this section, based on a combination of physical arguments and empirical observations from the DNS data (i.e., how well the instantaneous profiles collapse onto a single curve). Specifically, a number of different combinations of variables are tested for each term, and the standard deviation between the instantaneous profiles and the average over the entire self-similar region is calculated. For brevity, only the scalings that result in the lowest relative deviation from the self-similar average are presented below.

The proposed self-similar forms should be taken with some skepticism; this is the first time (to the authors' knowledge) that the self-similar forms of these terms have been examined in detail, and further refinements of the arguments proposed here are both welcome and expected. The self-similar scalings observed in the present study will be compared to proposed scalings from previous studies when applicable.

5.2.1 Rate of change of iso-surface area density

The self-similar behavior of $\partial\Sigma/\partial t$ should be examined in the context of the self-similar behavior of Σ, which was recently suggested by [7] to be

$$\Sigma(y,t) = \frac{1}{\lambda_\phi(t)}\widehat{\Sigma}(\xi) \tag{5.5}$$

Therefore, the time derivative of Σ can be expressed as

$$\frac{\partial\Sigma}{\partial t} = -\frac{1}{h\lambda_\phi}\frac{dh}{dt}\frac{d\widehat{\Sigma}}{d\xi}\xi - \frac{1}{\lambda_\phi^2}\frac{d\lambda_\phi}{dt}\widehat{\Sigma}. \tag{5.6}$$

From the dimensional coefficient of the first term, the following self-similar scaling is proposed,

$$\frac{\partial\Sigma}{\partial t} = \frac{\Delta U}{h\lambda_\phi}\frac{\partial\widehat{\Sigma}}{\partial\hat{t}}, \tag{5.7}$$

where the velocity difference, ΔU, has been substituted in the place of dh/dt because it of its previous use in self-similar arguments. In practice, the derivative of the mixing layer width, dh/dt, makes more sense as a velocity scale in the transverse direction, as there is no mean convective velocity in the y direction [4]. Regardless, it is expected that ΔU should always be proportional to dh/dt in the self-similar region.

In figure 5.3 is plotted several instantaneous profiles of $\partial\Sigma/\partial t$, non-dimensionalized by $h\lambda_\phi/\Delta U$, compared to the average value over the entire self-similar period. For $\Phi_{\text{iso}} = 0.95$, the self-similar collapse is fairly good. For an iso-value $\Phi_{\text{iso}} = 0.5$, however, the self-similar collapse is not as good, with significant fluctuations observed around the mean profile. Note that, from the symmetry in the problem initial conditions, these curves should be symmetric about $y/h = 0$; this lack of symmetry gives an idea of the statistical error in the measurement in this particular case. This error is likely because the averaging calculations performed in the present study made use of restart files, written to disk every 200 physical timesteps, which significantly reduces the temporal resolution available for estimating time derivatives. It should be noted that all of the remaining terms, which do not contain time derivatives, exhibit significantly greater statistical convergence.

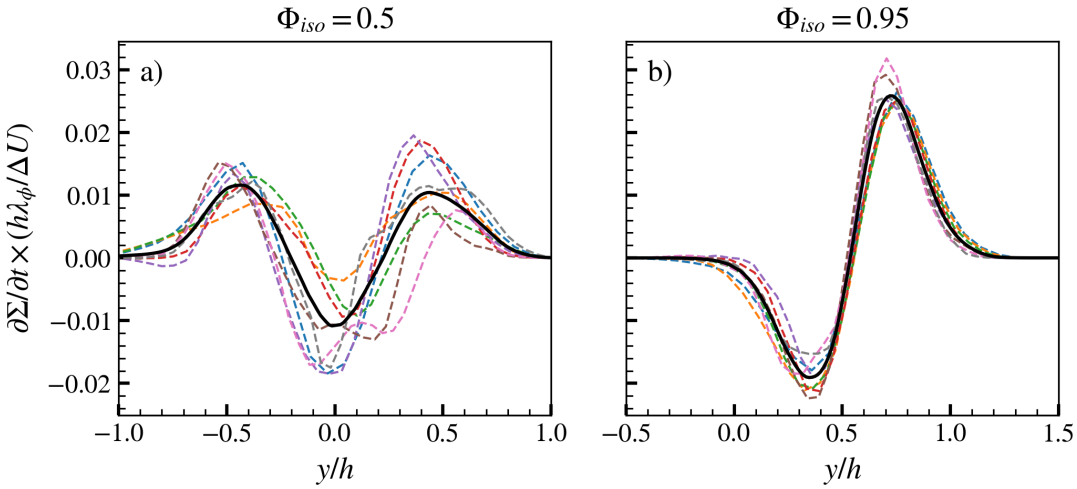

Figure 5.3: Proposed self-similar scaling of $\partial\Sigma/\partial t$ from (1.9), conditioned on a) $\Phi_{\text{iso}} = 0.5$ and b) $\Phi_{\text{iso}} = 0.95$, as a function of the similarity variable $\xi = y/h$. The solid line refers to the time-average over the entire self-similar period, and dashed lines refer to instantaneous profiles.

As a way to confirm that the self-similar profile of $\partial\Sigma/\partial t$ is qualitatively correct, it is compared to the right-hand side of equation (1.9), normalized by $h\lambda_\phi/\Delta U$, in figure 5.4. The self-similar profiles of the right-hand side of (1.9) (dotted line) demonstrate qualitatively similar behavior for both iso-values plotted, although there are significant differences near the peaks of the curves.

Additionally, it was found that $\widehat{\Sigma}$ can be approximated reasonably well with a Gaussian profile (as discussed in Chapter 4, Equation 4.13) in the form

$$\widehat{\Sigma}(\xi;\Phi_{\text{iso}}) = \hat{\Sigma}_m \exp\left(-\frac{(\xi-\xi_m)^2}{2\hat{\sigma}^2}\right), \tag{5.8}$$

where $\hat{\Sigma}_m$, ξ_m, and $\hat{\sigma}$ are the peak value, location of peak value, and standard deviation of $\widehat{\Sigma}$ in the self-similar coordinates [7]. Substituting the above expression for $\widehat{\Sigma}(\xi)$ into equation (5.6) and using the values of h, dh/dt, λ_ϕ, and $d\lambda_\phi/dt$ from the present DNS yields the dashed line in figure 5.4. As indicated by the similarity between the dashed and solid curves, there is good agreement between the result using this modeled curve

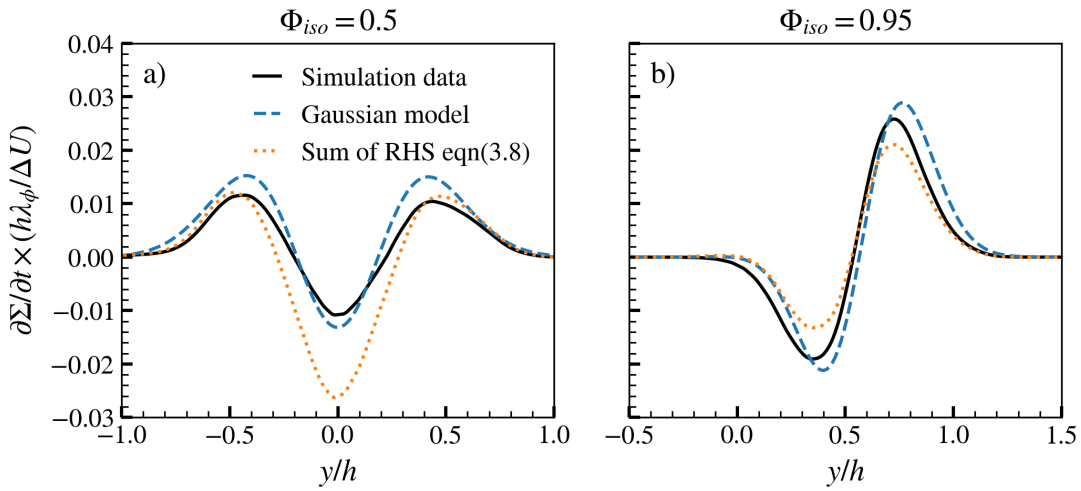

Figure 5.4: Self-similar profile of $\partial\Sigma/\partial t$ normalized by $h\lambda_\phi/\Delta U$ compared to the predicted self-similar profile assuming that Σ is Gaussian (dashed line) and the sum of terms on the right-hand side of equation (1.9) (dotted line), for a) $\Phi_{\text{iso}} = 0.5$ and b) $\Phi_{\text{iso}} = 0.95$.

and the self-similar form for the time derivative of Σ.

5.2.2 Convective transport

Next, consider $\mathcal{T}_U = -\partial/\partial x_i(\langle U_i \rangle_s \Sigma)$, which describes the transport of Σ due to the velocity field. This can be decomposed into mean and fluctuating components $\mathcal{T}_m$ and $\mathcal{T}_t$,

$$\frac{\partial}{\partial x_i}\left(\langle U_i \rangle_s \Sigma\right) = \underbrace{\frac{\partial}{\partial x_i}\left(\langle U_i \rangle \Sigma\right)}_{\mathcal{T}_m} + \underbrace{\frac{\partial}{\partial x_i}\left(\langle u_i \rangle_s \Sigma\right)}_{\mathcal{T}_t}, \tag{5.9}$$

where $\langle u_i \rangle_s$ is the surface average of the fluctuating component of velocity u_i. Due to the geometry of the mixing layer, only the cross-stream velocity, V, will contribute to $\mathcal{T}_U$. Furthermore, it can be shown from conservation of mass and the free slip boundary condition that the mean cross-stream velocity, $\langle V \rangle$, must be zero for all values of y. Thus, the effect of the velocity field on the rate of change of Σ is due

entirely to the turbulent fluctuations of the cross-stream velocity, v, and hence the turbulent flux, $\mathcal{T}_t$.

To estimate how $\mathcal{T}_t$ will evolve in the self-similar region, it is reasonable to assume that the surface-averaged velocity fluctuations, $\langle u_i \rangle_s$, will scale similar to the rms velocity, $\langle u_i u_i \rangle^{1/2}$, which is known to scale with the velocity difference ΔU [79]. By noting that $\Sigma \sim \lambda_\phi$ (see figure 4.5) and assuming the cross-stream derivative will scale with the mixing width, i.e., $\partial/\partial y \sim 1/h$, then the self-similar form of $\mathcal{T}_t$ should be

$$\mathcal{T}_t = \frac{\Delta U}{h\lambda_\phi}\widehat{\mathcal{T}}_t. \tag{5.10}$$

Notably, this proposed scaling for $\mathcal{T}_t$ agrees with the self-similar form for $\partial\Sigma/\partial t$ in (5.7).

In figure 5.5 is plotted the self-similar profiles of $\mathcal{T}_t$. Apart from small fluctuations around the peaks of the curves, the instantaneous profiles collapse onto a single curve for the assumed self-similar form, suggesting that (5.10) is the appropriate scaling for $\mathcal{T}_t$ for this temporal turbulent mixing layer.

These data also suggest that the turbulent transport for the iso-surface corresponding to $\Phi_{\text{iso}} = 0.5$ acts in a traditional gradient-diffusive manner [99], acting to remove Σ from the peak and diffuse it outwards. In fact, for a constant, non-dimensional turbulent diffusivity $\widehat{D}_t = 0.015$, it can be shown that the assumption

$$\widehat{\langle v\Sigma' \rangle}_s = -\widehat{D}_t \frac{\partial \widehat{\Sigma}}{\partial \xi} \tag{5.11}$$

gives an excellent match when $\Phi_{\text{iso}} = 0.5$, as shown in figure 5.6a. For iso-surfaces far from the centerline, e.g., $\Phi_{\text{iso}} = 0.95$, the turbulent transport is still diffusive in nature by removing Σ from the local peak, but the diffusion is preferentially towards the center of the mixing layer, rather than away from the centerline as might be expected. In this case, the assumption of a constant turbulent diffusivity is clearly incorrect, as demonstrated by the significant discrepancy between the two curves in figure 5.6b. It is possible that the preferential diffusion towards the centerline is

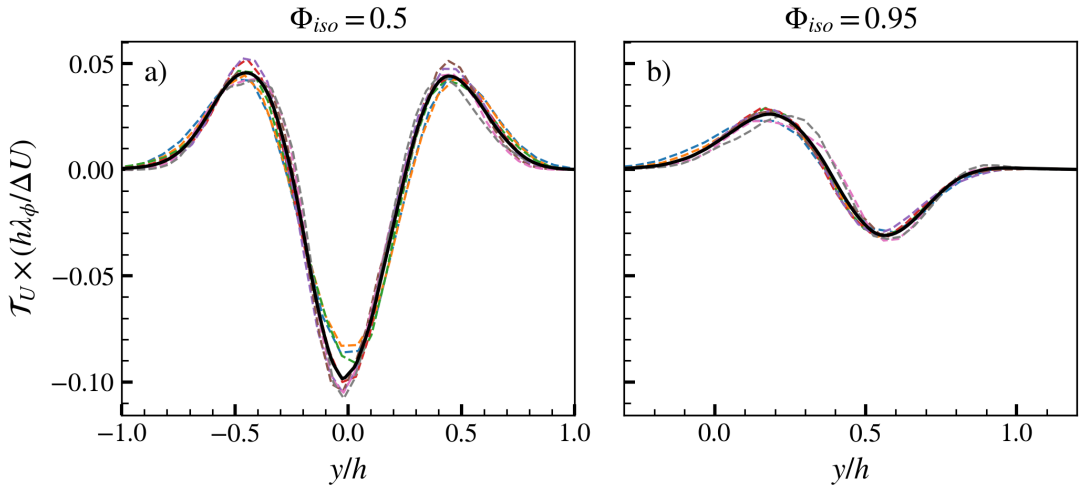

Figure 5.5: Proposed self-similar scaling of term $\mathcal{T}_U = \partial/\partial x_i(\langle U_i \rangle_s \Sigma)$ from (5.10), conditioned on a) $\Phi_{\text{iso}} = 0.5$ and b) $\Phi_{\text{iso}} = 0.95$, as a function of the similarity variable $\xi = y/h$. Solid and dashed lines as in figure 5.3.

due to the fact that the turbulent fluctuations are greatest near $y/h = 0$ (see, e.g., figure 2.7a) and decay quickly to zero near the edge of the mixing layer. This could, perhaps, be accounted for in the turbulent diffusivity, by choosing the standard form $D_t = \alpha u' \ell$, where α is a constant, u' is the rms of the velocity fluctuations, and ℓ is a characteristic length [74], or by a two-equation model that better approximates the inhomogeneous nature of the turbulent fluctuations. Although this will not be investigated further in the present study, it should be emphasized that care should be taken in modeling the turbulent flux of an iso-surface, as the behavior of $\mathcal{T}_t$ exhibits a strong dependence on the iso-value chosen in the present configuration.

5.2.3 Production

Consider now the production term, $\mathcal{P} = -\langle n_i n_j S_{ij} \rangle_s \Sigma$. Self-similar scaling for this term can be deduced by considering that the rate of production of Σ has been found by previous studies to be proportional to the mean turbulent strain-rate, i.e., $\langle n_i n_j S_{ij} \rangle_s \sim$

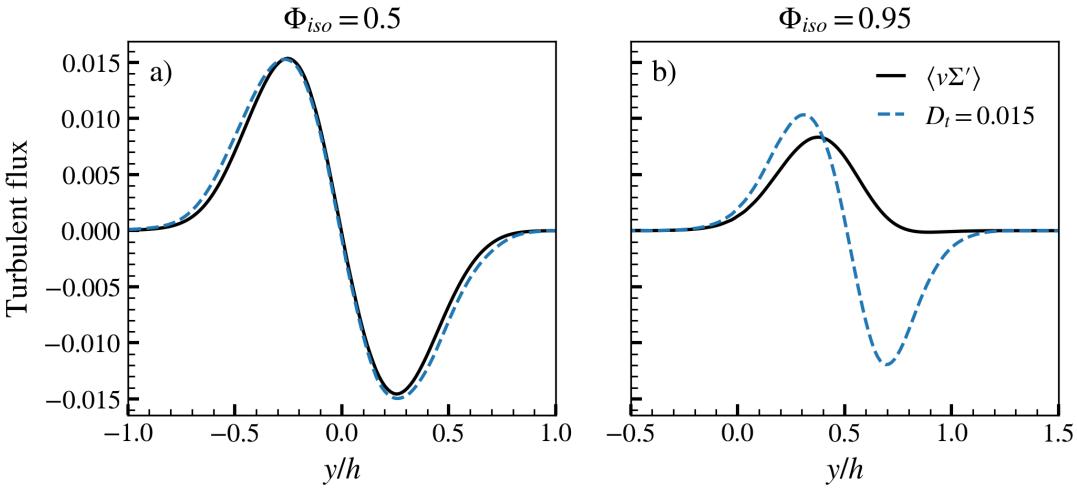

Figure 5.6: Cross-stream profile of the surface weighted velocity, $\langle v\Sigma' \rangle$ in the self-similar period, compared to the gradient-diffusion hypothesis (assuming constant turbulent diffusivity, $\widehat{D}_t = 0.015$) for a) $\Phi_{\text{iso}} = 0.5$ and b) $\Phi_{\text{iso}} = 0.95$.

$(\varepsilon/\nu)^{1/2}$ [71]. For the present temporal mixing layer, the transverse Taylor length scale, defined in equation (2.31), is expected to scale proportionally to the mean strain-rate, $\lambda_g/\Delta U \sim (\varepsilon/\nu)^{-1/2}$, which implies that $\langle n_i n_j S_{ij} \rangle_s \sim \lambda_g/\Delta U$. Recalling that $\Sigma \sim 1/\lambda_\phi$ and that $\lambda_g \sim \lambda_\phi$ in the present study, it is suggested that the production term scales according to

$$\mathcal{P} = \frac{\Delta U}{\lambda_\phi^2} \widehat{\mathcal{P}}. \tag{5.12}$$

The self-similar profiles for $\mathcal{P}$ are displayed in figure 5.7, which demonstrates excellent collapse of the self-similar profiles.

5.2.4 Diffusive transport

Before analyzing the diffusive transport term, $\mathcal{T}_D = -\partial(\langle w_{\text{iso}} n_i \rangle_s \Sigma)/\partial x_i$, it is helpful to first consider the self-similar behavior of the diffusive flux, i.e. $\langle w_{\text{iso}} n_i \Sigma' \rangle = \langle w_{\text{iso}} n_i \rangle_s \Sigma$. To begin, a characteristic velocity scale for w_{iso} is formed by consider-

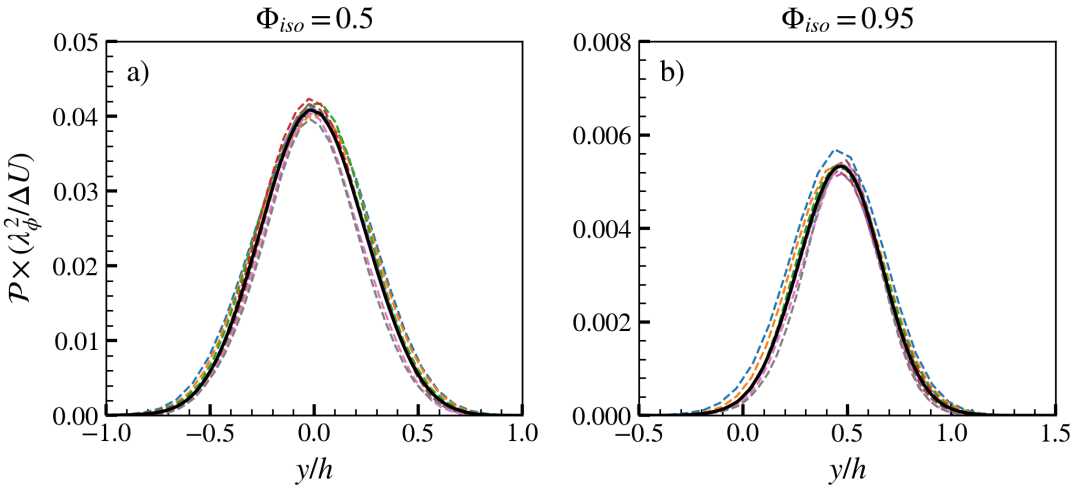

Figure 5.7: Proposed self-similar scaling of $\mathcal{P} = -\langle n_i n_j S_{ij} \rangle_s \Sigma$ from (5.12), conditioned on a) $\Phi_{\text{iso}} = 0.5$ and b) $\Phi_{\text{iso}} = 0.95$, as a function of the similarity variable $\xi = y/h$. Solid and dashed lines as in figure 5.3. Note that the magnitude of the peak value of $\mathcal{P}$ is significantly smaller near the edge of the mixing layer ($\Phi_{\text{iso}} = 0.95$) than it is near the centerline ($\Phi_{\text{iso}} = 0.5$.)

ing the rate at which a scalar with diffusivity D will diffuse over a length ℓ, such that $w_{\text{iso}} \sim D/\ell$. It was determined empirically that choosing $\ell = \lambda_\phi$ results in the least error between instantaneous and self-similar profiles, which suggests that $\langle w_{\text{iso}} \rangle_s \Sigma \sim D/\lambda_\phi^2$. Because $0 \leq n_i \leq 1$, it is not expected that the normal vector will affect the self-similar scaling of this term (although it will affect the direction of propagation). As shown in figure 5.8, there is close agreement between the instantaneous and mean profiles of the $y-$component of the surface averaged diffusive flux, $\langle w_{\text{iso}} n_y \rangle_s \Sigma$, for the proposed scaling. Note that only the $y-$component of the diffusive flux is shown here because it is the only component that contributes to $\mathcal{T}_D$.

The behavior of the diffusive flux in figure 5.8 can be somewhat counterintuitive. For $\Phi_{\text{iso}} = 0.95$ (figure 5.8b), the positive value of the diffusive flux indicates movement of the iso-surface in the $+y$ direction, causing Σ to diffuse away from the centerline

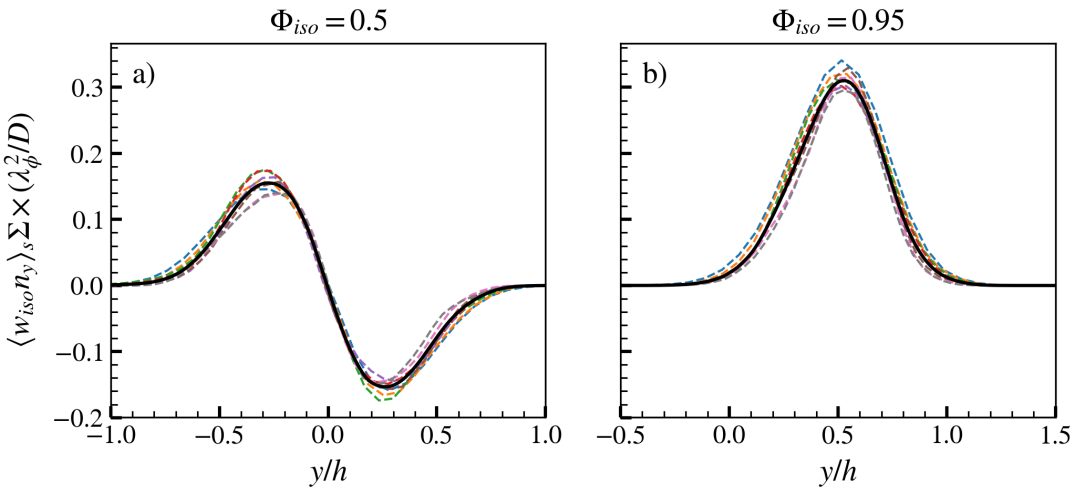

Figure 5.8: Proposed self-similar scaling of $\langle w_{\text{iso}} n_y \rangle_s \Sigma$, conditioned on a) $\Phi_{\text{iso}} = 0.5$ and b) $\Phi_{\text{iso}} = 0.95$, as a function of the similarity variable $\xi = y/h$. Solid and dashed lines as in figure 5.3.

with time in a manner consistent with the behavior of a purely diffusive scenario (i.e., for $U_i = 0$). The behavior of the diffusive flux for $\Phi_{\text{iso}} = 0.5$ (figure 5.8a) is not as straightforward. Interestingly, it appears that the diffusion velocity of the $\Phi_{\text{iso}} = 0.5$ iso-surface is oriented towards the centerline, rather than away from it. This is contrary to the observed behavior of Σ, shown in figure 4.3a, which diffuses away from the centerline and increases in width over time. Note that the symmetry of $\langle w_{\text{iso}} n_y \rangle_s \Sigma$ around $y/h = 0$ ensures that the net movement of the $\Phi_{\text{iso}} = 0.5$ iso-surface in any direction is in fact, zero, which is consistent with the observed behavior of Σ remaining symmetric about $y/h = 0$.

To scale the diffusion term, $\mathcal{T}_D$ in equation (1.9), it is assumed that the derivative in the cross-stream direction introduces a factor of $1/h$ to the scaling (similar to the argument for the convective flux, $\mathcal{T}_U$, above). Based on this assumption and the above

scaling proposed for $\langle w_{\text{iso}} n_i \rangle_s \Sigma$, the self-similar form of $\mathcal{T}_D$ is given by

$$\mathcal{T}_D = \frac{D}{h\lambda_\phi^2} \widehat{\mathcal{T}}_D. \tag{5.13}$$

In figure 5.9 is displayed the results for $\mathcal{T}_D$ using the above self-similar scaling, which again demonstrates good agreement between the instantaneous and averaged profiles.

Similar to the results of the diffusive flux above, the behavior of $\mathcal{T}_D$ is somewhat counterintuitive. For an iso-surface corresponding to $\Phi_{\text{iso}} = 0.95$ (figure 5.9b), the effect of $\mathcal{T}_D$ is to remove Σ near the centerline and redistribute it to the outside of the layer, which is consistent with the behavior of a purely diffusive layer, i.e., in the case that $U_i = 0$. In contrast, for an iso-surface $\Phi_{\text{iso}} = 0.5$, it appears that Σ diffuses towards the centerline. In this case, the molecular diffusion seems to be *concentrating* Σ near $y/h = 0$, rather than diffusing it away, as expected in this scenario. It is not immediately evident why the observed behavior of the scalar iso-surface differs from the simplified example of a purely diffusive scalar.

For the present DNS, the magnitude of $\mathcal{T}_D$ is negligible compared to the other terms (see § 5.3); as such, the effect of molecular diffusion on $\partial\Sigma/\partial t$ is small and will not be investigated further. It should be noted that this term is not expected to be negligible for highly diffusive surfaces (i.e., $Sc \ll 1$), or active surfaces such as premixed flames, and will therefore require further study.

5.2.5 Destruction

The self-similar development of $\mathcal{D} = -\langle w_{\text{iso}} \partial n_i/\partial x_i \rangle_s \Sigma$ can be understood by invoking a well-known identity that decomposes w_{iso} into two terms, one related to diffusion in the direction normal to the iso-surface, w_N, and one related to the curvature of the iso-surface, w_C [94]:

$$w_{\text{iso}} = \underbrace{-\frac{D}{|\nabla\Phi|}\frac{\partial|\nabla\Phi|}{\partial x_i} n_i}_{w_N} \underbrace{-\frac{\partial n_i}{\partial x_i}}_{w_C}. \tag{5.14}$$

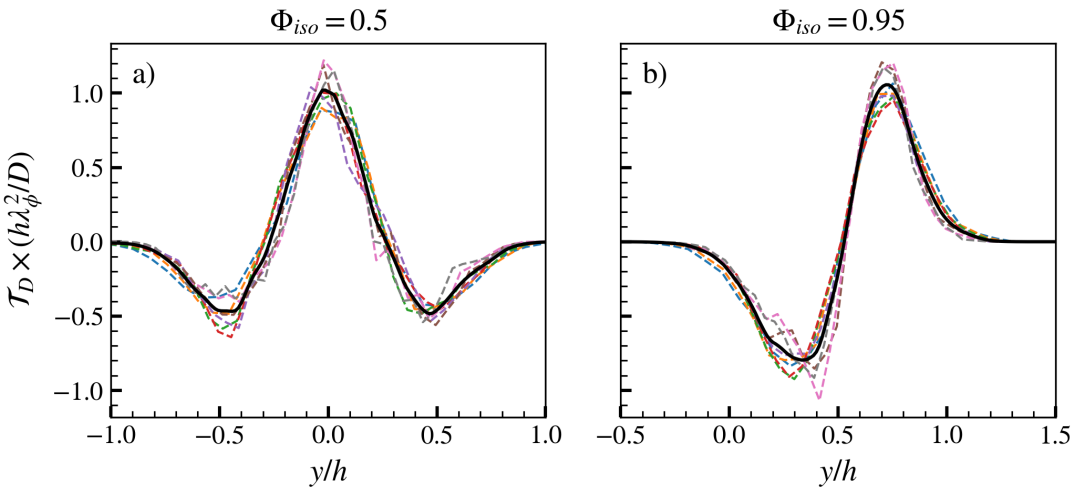

Figure 5.9: Proposed self-similar scaling of term $\mathcal{T}_D = -\partial(\langle w_{\text{iso}} n_i \rangle_s \Sigma)/\partial x_i$ from (5.13), conditioned on a) $\Phi_{\text{iso}} = 0.5$ and b) $\Phi_{\text{iso}} = 0.95$, as a function of the similarity variable $\xi = y/h$. Solid and dashed lines as in figure 5.3.

This decomposition can be used to split term $\mathcal{D}$ into two separate components,

$$\mathcal{D} = \underbrace{\left\langle w_N \frac{\partial n_i}{\partial x_i} \right\rangle_s \Sigma}_{\mathcal{D}_a} + \underbrace{D \left\langle \left(\frac{\partial n_i}{\partial x_i} \right)^2 \right\rangle_s \Sigma}_{\mathcal{D}_b}, \tag{5.15}$$

where $\mathcal{D}_b$ is notable because, when substituted into equation (1.9), it must always take on a negative value in a manner analogous to the dissipation-rates ε and χ. In contrast, $\mathcal{D}_a$ may take on either positive or negative values; in the present DNS, $\mathcal{D}_a$ predominantly acts to destroy iso-surface area density (except for a very slight region on the far outside of the mixing layer). Although some studies have suggested that $\mathcal{D}_a$ is negligible compared to $\mathcal{D}_b$ [94], the terms are found to be of comparable magnitude in the present study, as shown in figure 5.10. Because the two terms are of comparable magnitude over a wide range of iso-values, it is postulated that $\mathcal{D}_a$ and $\mathcal{D}_b$ will evolve together during the self-similar period. This assumption will be used to simplify the scaling argument below for the destruction term.

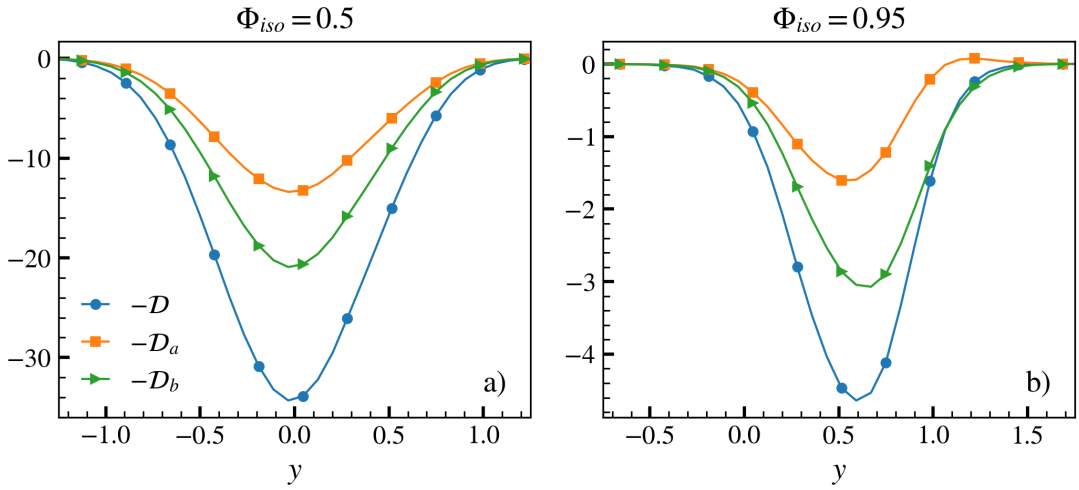

Figure 5.10: Decomposition of term $\mathcal{D}$ into components related to normal diffusion (V_a) and curvature (V_b) at $t\Delta U/h_0 = 462$, conditioned on a) $\Phi_{\text{iso}} = 0.5$ and b) $\Phi_{\text{iso}} = 0.95$. Terms are normalized by the mixing layer width at $t\Delta U/h = 462$ and the velocity difference, $h^2/\Delta U$. Note the difference in scales between panels a) and b).

As something of an aside, consider briefly the self-similar behavior of the surface-averaged mean curvature, $\langle \partial n_i/\partial x_i \rangle_s \, \Sigma$. The mean curvature is typically interpreted as the characteristic size of 'wrinkles' in the iso-surface. The appropriate scaling of this wrinkling length is somewhat controversial; previous studies have suggested that it scales with an integral scale of the flow [94], while others imply that it scales with the smallest features in the flow, i.e., the Kolmogorov scale η [48]. It has also been postulated that the mean curvature is proportional to the peak value of Σ [39], although the derivation relies on the 'generalized' flame surface density [9] rather than the fine grained iso-surface area density used here. Despite the differences, results from the current study are consistent with the peak value of Σ, wherein the mean curvature is shown in figure 5.11a and b to evolve at the same rate as the peak value of Σ, i.e., $\langle \partial n_i/\partial x_i \rangle_s \sim \Sigma_{\max} \sim 1/\lambda_\phi$. It can be seen that the proposed scaling

results in a convincing collapse of the instantaneous profiles on the average over the self-similar period, for both of the iso-surfaces shown here.

One might expect, if the mean curvature scales like $1/\lambda_\phi$, for the mean square curvature to scale with $1/\lambda_\phi^2$. However, according to the present DNS, the best collapse of the instantaneous profiles of $\langle(\partial n_i/\partial x_i)^2\rangle_s$ occurs when scaled with $1/\eta^2$. The instantaneous and self-similar profiles are displayed in figure 5.11c and d for $\Phi_{\text{iso}} = 0.5$ and $\Phi_{\text{iso}} = 0.95$, respectively, and demonstrate excellent agreement. From a physical standpoint, this can be understood by considering that the mean curvature is proportional to $\langle 1/r_1 + 2/r_2\rangle_s$, where r_1 and r_2 are the radii of curvature of the iso-surface, and the mean square curvature is proportional to $\langle(1/r_1 + 1/r_2)^2\rangle_s$. Clearly, the effect of the smallest lengthscales of the surface will dominate the mean square curvature, which are expected to be on the order of the Kolmogorov scale [87].

These results may be further justified by analogy to canonical scaling arguments involving velocity derivatives. For example, the mean velocity gradient in a shear layer is typically scaled by the mixing layer width h, $\langle\partial U_i/\partial x_j\rangle \sim \Delta U/h$, but the mean square velocity gradient is scaled with the Taylor scale, λ, $\langle(\partial U_i/\partial x_j)^2\rangle \sim \Delta U^2/\lambda^2$ [90]. Therefore, it is not unreasonable to imagine that the mean curvature and mean square curvature scale separately from each other.

Returning now to the the destruction term, $\mathcal{D}$, based on the above discussion it is assumed that 1.) $\mathcal{D} \sim \mathcal{D}_b$, and 2.) that $\langle(\partial n_i/\partial x_i)^2\rangle_s \sim \eta^{-2}$. This suggests the following self-similar scaling for the destruction,

$$\mathcal{D} = \frac{D}{\lambda_\phi \eta^2}\widehat{\mathcal{D}}, \tag{5.16}$$

which yields good agreement between instantaneous and time-averaged profiles as displayed in figure 5.12.

Now, it was demonstrated in figure 5.2 that the production and destruction terms are significantly larger than the remaining terms in equation (1.9), but of a similar magnitude to each other, suggesting that the production and destruction should scale

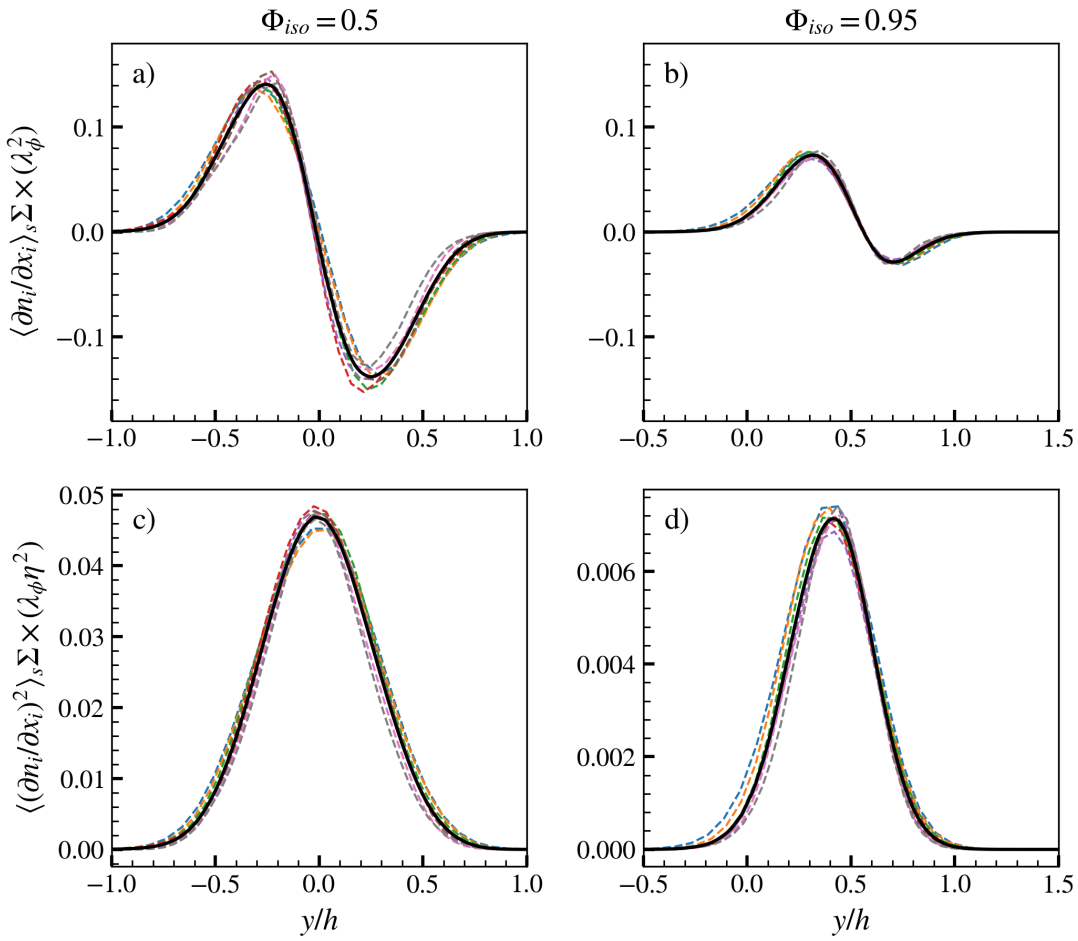

Figure 5.11: Proposed self-similar scaling of $\langle \partial n_i/\partial x_i \rangle_s$, conditioned on a) $\Phi_{\text{iso}} = 0.5$ and b) $\Phi_{\text{iso}} = 0.95$, and $\langle (\partial n_i/\partial x_i)^2 \rangle_s$, conditioned on c) $\Phi_{\text{iso}} = 0.5$ and d) $\Phi_{\text{iso}} = 0.95$. Profiles are plotted as a function of the similarity variable $\xi = y/h$. Solid and dashed lines as in figure 5.3. Note the difference in scales between the various curves.

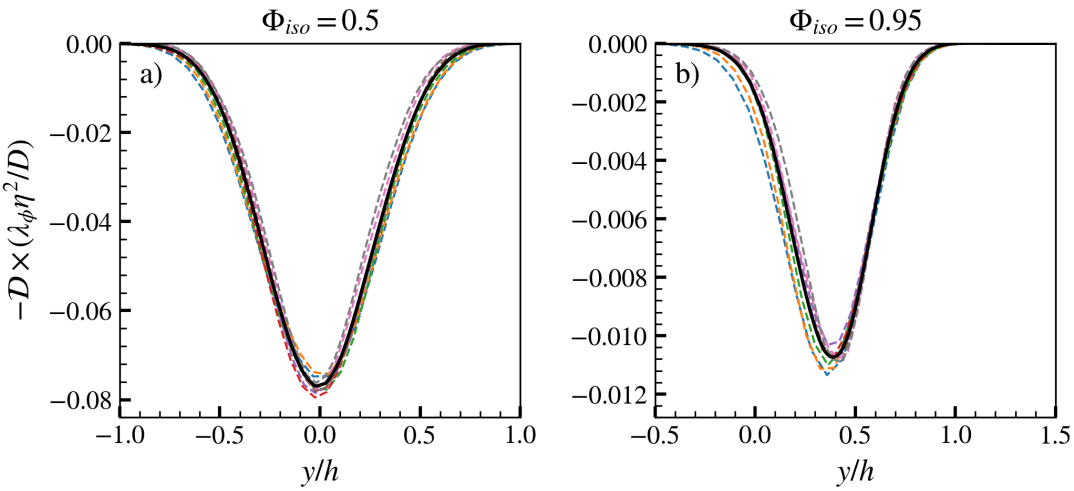

Figure 5.12: Proposed self-similar scaling of the destruction term, $\mathcal{D} = \langle w_{\text{iso}} \partial n_i / \partial x_i \rangle_s \, \Sigma$ from (1.9), conditioned on a) $\Phi_{\text{iso}} = 0.5$ and b) $\Phi_{\text{iso}} = 0.95$, as a function of the similarity variable $\xi = y/h$. Solid and dashed lines as in figure 5.3.

similarly. However, from the current discussion, it is proposed that $\mathcal{D} \sim D/\lambda_\phi \eta^2$, whereas $\mathcal{P} \sim \Delta U / \lambda_\phi^2$. This discrepancy can be resolved by noting that, in the present DNS with constant Schmidt number equal to 0.7, the Kolmogorov and Batchelor scales are directly proportional, where the Batchelor scale is defined as $\eta_B = \eta Sc^{-1/2}$. From this definition, and the definition of the Kolmogorov scale in equation (2.30), it can be shown that

$$\eta_B^2 = D \left(\frac{\varepsilon}{\nu} \right)^{1/2}. \tag{5.17}$$

Noting that the Taylor scale, defined in equation (2.31), is proportional to $(\varepsilon/\nu)^{1/2}$ and that $\lambda_g \sim \lambda_\phi$ in the present DNS, it can be shown that

$$\eta^2 \sim \eta_B^2 \sim \frac{D \lambda_\phi}{\Delta U}. \tag{5.18}$$

Substituting this expression for η^2 into the self-similar form given above for $\mathcal{D}$ yields

$$\mathcal{D} \sim \frac{\Delta U}{\lambda_\phi^2} \widehat{\mathcal{D}}, \tag{5.19}$$

which is the same scaling observed for the production term. Note that, although the Schmidt number dependence is included where possible, the present results assume a Schmidt number of order $O(1)$ and may not be valid for flows with Schmidt numbers significantly different from unity, such as Hydrogen diffusing in air or diluents such as salt in water. Furthermore, the diffusivity in the present simulations is constant and may not apply for flows with significant temperature or density gradients such as premixed flames or highly stratified flows.

5.2.6 Net effect of production and destruction terms

The final term to analyze is the net effect of production and destruction, $K = \mathcal{P} - \mathcal{D}$. As discussed briefly in § 5.1.2, terms $\mathcal{P}$ and $\mathcal{D}$ are both an order of magnitude larger than $\partial\Sigma/\partial t$ and $\mathcal{T}_U$. Despite this discrepancy in magnitudes, it is clear that $\partial\Sigma/\partial t$ and $\mathcal{T}_U$ cannot be neglected. For example, the location of an iso-surface in the present mixing layer, say $\Phi_{\text{iso}} > 0.5$, *must* translate in the $+y$ direction for the mixing layer width to increase with time. Thus, a non-trivial value of $\partial\Sigma/\partial t$ is required. As displayed in figure 5.2b, computing the net effect of the production and destruction, K, yields a term that is the same order of magnitude as $\partial\Sigma/\partial t$ and $\mathcal{T}_U$.

Assuming that K will develop proportionally to $\partial\Sigma/\partial t$ and $\mathcal{T}_U$ yields the following self-similar form,

$$K = \frac{\Delta U}{h\lambda_\phi}\widehat{K}. \tag{5.20}$$

The normalized cross-stream profiles are displayed in figure 5.13, which once again demonstrates agreement between the instantaneous and time-averaged profiles, aside from some fluctuations around $y/h = 0$. Importantly, the fluctuations observed here are non-monotonic in time, i.e., the error is likely statistical in nature, and not systematic.

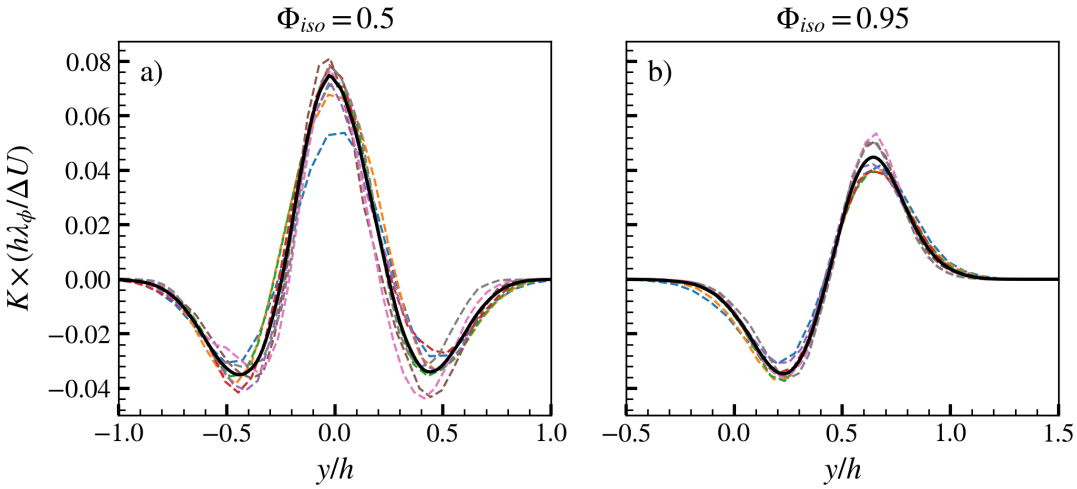

Figure 5.13: Proposed self-similar scaling of K from (5.20), conditioned on a) $\Phi_{\text{iso}} = 0.5$ and b) $\Phi_{\text{iso}} = 0.95$, as a function of the similarity variable $\xi = y/h$. Solid and dashed lines as in figure 5.3.

5.3 Discussion

According to the above analysis, the terms in the Σ evolution equation, equation (1.9), evolve in a self-similar manner, according to:

$$\frac{\partial \Sigma}{\partial t} = \frac{\Delta U}{h\lambda_\phi}\frac{d\widehat{\Sigma}}{d\hat{t}}, \qquad \mathcal{T}_t = \frac{\Delta U}{h\lambda_\phi}\widehat{\mathcal{T}}_t, \qquad \mathcal{P} = \frac{\Delta U}{\lambda_\phi^2}\widehat{\mathcal{P}},$$
$$\mathcal{T}_D = \frac{D}{h\lambda_\phi^2}\widehat{\mathcal{T}}_D, \qquad \text{and} \qquad \mathcal{D} = \frac{\Delta U}{\lambda_\phi^2}\widehat{\mathcal{D}},$$

where the lengthscales h, λ_ϕ, and η are understood to be functions of time, t. Furthermore, the net effect of production and destruction, i.e., $K = \mathcal{P} - \mathcal{D}$, is found to evolve according to

$$K = \frac{\Delta U}{h\lambda_\phi}\widehat{K}.$$

Substituting these self-similar forms into (1.9) and multiplying by $h\lambda_\phi/\Delta U$ yields the following equation for the self-similar iso-surface transport equation,

$$\frac{\partial \widehat{\Sigma}}{\partial \hat{t}} = \widehat{\mathcal{T}}_t + \frac{h}{\lambda_\phi}\widehat{\mathcal{P}} + \frac{D}{\lambda_\phi \Delta U}\widehat{\mathcal{T}}_D - \frac{h}{\lambda_\phi}\widehat{\mathcal{D}}. \tag{5.21}$$

There are a couple of important conclusions that can be drawn from this expression. First, note that the production and destruction, terms $\mathcal{P}$ and $\mathcal{D}$, are multiplied by the ratio of the mixing layer width to the Taylor lengthscale. By taking the mixing layer width to be the integral scale of the flow and invoking well-known scaling arguments [90, 74], this ratio is expected to scale like $h/\lambda_\phi \sim (ReSc)^{1/2}$. This, in turn, suggests that the coefficient multiplying these terms will become large compared to $\partial\Sigma/\partial t$ and $\mathcal{T}_t$ for highly turbulent flows, i.e., $ReSc \gg 1$. This suggested scaling agrees well with the behavior observed in the present study. Second, the coefficient of the diffusion term, $\mathcal{T}_D$, can also be interpreted according to the Reynolds and Schmidt numbers. By invoking similar scaling arguments above, it can be shown that $D/\lambda_\phi \Delta U \sim (ReSc)^{-1/2}$ [90, 74]. In contrast to the production and destruction terms, it can be seen that the coefficient of the diffusion term becomes small compared to $\partial\Sigma/\partial t$ for $ReSc \gg 1$. Again, this suggested scaling agrees well with the observed behavior in the present shear layer.

A simplified expression for $\partial\Sigma/\partial t$ in the present study can be obtained by combining the production and destruction terms into their net effect and neglecting the molecular diffusion term, which yields

$$\frac{\partial\widehat{\Sigma}}{\partial\hat{t}} = \widehat{\mathcal{T}}_t + \widehat{K}. \tag{5.22}$$

According to the above equation, the rate of change of Σ at any location in the flow is due to the net growth or decay of the surface due to the combined effects of production and destruction, which is then transported throughout the mixing layer by turbulent diffusion. Self-similar profiles of this simplified balance equation for Σ are plotted in figure 5.14. In addition, the sum of the terms on the right-hand side of (5.22) are plotted as a dotted line, which agrees well with the explicit time derivative of Σ, although there is some error between the two curves for $\Phi_{\text{iso}} = 0.5$, particularly near the centerline.

From figure 5.14a, it can be seen that, for the iso-value $\Phi_{\text{iso}} = 0.5$, there is a net

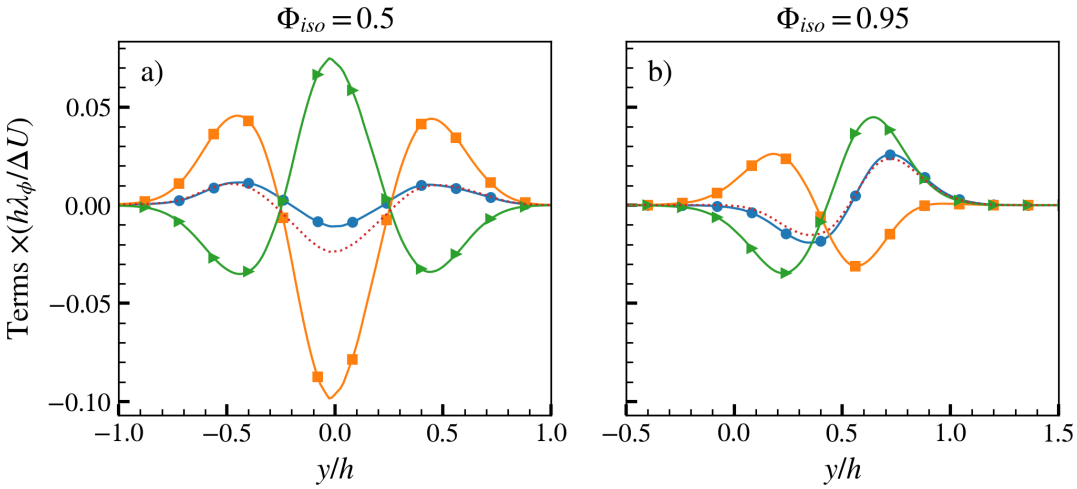

Figure 5.14: Self-similar profiles of the terms in (5.22) for a) $\Phi_{\text{iso}} = 0.5$ and b) $\Phi_{\text{iso}} = 0.95$. Circles refer to $\partial\widehat{\Sigma}/\partial\hat{t}$, squares to $\widehat{\mathcal{T}}_U$, triangles to $\widehat{K}$, and the dotted line is the sum of $\widehat{\mathcal{T}}_U + \widehat{K}$. Terms have been normalized by $h\lambda_\phi/\Delta U$ and averaged over the self-similar period.

positive effect of $\mathcal{P} - \mathcal{D}$ near the center of the mixing layer, but this falls steeply and becomes a net decrease in Σ toward the outer edges. This is offset by the turbulent flux term, $\mathcal{T}_t$, which acts in a diffusive manner by decreasing the concentration of Σ at the centerline and redistributing it to the outer edge of the mixing layer. The end result is that Σ is shown to decrease in magnitude near $y/h = 0$, but increase away from the center, with a local peak near $y/h \approx \pm 0.4$. This rate of change is consistent with the observed temporal evolution of Σ, which tends to diffuse outward, as discussed in Chapter 4.

For the iso-value $\Phi_{\text{iso}} = 0.95$, the self-similar profiles are displayed in figure 5.14b. Here, the net effect of $\mathcal{P} - \mathcal{D}$ is positive towards the far outside of the mixing layer, with a maximum occurring around $y/h \approx 0.65$, which decreases and becomes a net destruction of Σ closer to the centerline, with a minimum occurring near $y/h \approx 0.2$. This is rather counterintuitive, as ε and χ are greatest around $y/h = 0$, which are

expected to increase Σ. The turbulent flux is found to promote iso-surface movement of Σ toward the center of the mixing layer, rather than toward the edges as might be expected for a diffusive term. This could be due to the fact that the turbulent fluctuations are concentrated near $y/h = 0$ (as shown in figure 2.7), causing the iso-surface to skew in that direction. Overall, the behavior of $\partial\Sigma/\partial t$ is consistent with the results discussed in Chapter 4, which is to translate Σ in the $+y$ direction. It is interesting to note that the translation in the $+y$ direction is actually driven by the production and destruction terms, and is impeded by the turbulent flux. This is opposite of the behavior observed for $\Phi_{\text{iso}} = 0.5$, in which Σ was produced in the region of greatest turbulent fluctuations and diffused outward. It is unclear why the behavior appears to change as a function of Φ_{iso}; additional investigation into these kinematics may prove enlightening.

Chapter 6

CONCLUSIONS

The primary focus of the present work is toward a fundamental understanding of the spatial and temporal evolution of the iso-surface area density of a passive scalar interacting with a turbulent flow field. Though this dissertation represents but a small contribution to the current literature, the main objective is to lay down a solid foundation of understanding from which future studies can flourish. Based upon recent literature reviewed in Chapter 1, it is this author's opinion that a return to the fundamentals is warranted, in this case, by eschewing complex physical phenomena, e.g., variable density effects due to heat released by chemical reactions. Instead, the focus is on numerical experimentation, in the form of direct numerical simulation, of passive scalars advected by a turbulent velocity field. Studies were carried out with the use of two distinct computer programs, described in some detail in Chapter 2; the first was written in-house and simulated with the use of Amazon Web Services Elastic Cloud Computing resources; the second, named Miranda, was modified to work with graphics processing units and was simulated with the use of the Lassen supercomputer at Lawrence Livermore National Laboratory. The following discussion will attempt to summarize the studies presented in Chapters 3, 4 and 5, concluding with a perspective on the potential impact of the present work on the field, as well as recommendations for future work on this topic.

6.1 Summary

Iso-surfaces in H.I.T.

This initial study is a first look at the tools and methodologies used in this dissertation, with a focus on studying the evolution of passive scalar iso-surfaces in homogeneous, isotropic turbulence. In an attempt to better understand how the scalar and velocity fields interact, two different initial distributions of the passive scalar field were simulated, one that is homogeneously distributed throughout the domain (Case A) and one that has an initially planar configuration (Case B). This distinction yielded interesting results, demonstrating that, despite interacting with an identical velocity field, the behavior of the iso-surface area varied considerably between the two cases.

From this analysis, it was showed that the production term, Term III, demonstrates a slight dependence on the value of Z_{iso} for both the initially planar and initially isotropic scalar fields. Decomposing Term III based on the principal axes of the stress tensor demonstrated that iso-surface production is due to compressive strain-rates, and that the alignment between the iso-surface normal vectors and the principal strain-rates is consistent with previous studies. In addition, it was found that iso-surfaces far from Z_{iso} are associated with smaller magnitudes of the principal strain-rates.

The destruction term, Term V, was also analyzed in detail. This term is of particular interest because iso-surface behavior depends on the initial scalar field. Although the $Z_{\text{iso}} = 0.5$ iso-surfaces were found to behave similarly between the isotropic and planar initial conditions, the $Z_{\text{iso}} = 0.05$ and 0.95 iso-surfaces did not. The diffusion velocity was found to be similar in both cases, but the mean curvature was significantly larger for Case A than Case B. It it thought that this effect is due to molecular diffusion having a more dominant role in the formation of curvature in Case A, although this needs additional exploration.

Self-similarity of iso-surface area density

In this chapter, data from a direct numerical simulation of a temporally developing mixing layer were shown to exhibit a robust period of self-similar behavior for both the velocity and scalar fields that is consistent with analytical results and with data from previous simulations [5, 79, 1, 4]. A novel methodology described in appendix A was used to compute the iso-surface area, A_{iso}, and iso-surface area density, $\Sigma(y,t)$, in a manner that is consistent with formal definitions in the literature [72, 97]. The temporal development of A_{iso} and Σ were examined in detail in §§ 4.1 and 4.2, and it was demonstrated that Σ develops in a self-similar manner, corresponding to the self-similar evolution of the velocity and scalar fields. For a given Φ_{iso}, cross-stream profiles of Σ collapse onto a single curve when normalized by the Taylor length scale, λ_ϕ, and plotted against the normalized coordinate y/h. This finding suggests that the iso-surface area could be scaled in a similar fashion, and it was found that, for the mixing layer, the normalized iso-surface area is expected to scale as $A_{\text{iso}}/A_0 \sim (ReSc)^{1/2}$. Finally, a simple mathematical model of the self-similar iso-surface area density, $\hat{\Sigma}$, was developed for the range of iso-values studied here. $\hat{\Sigma}$ demonstrated good agreement with a Gaussian profile, although some skewness is observed towards the outer boundaries of the mixing layer, which is thought to be caused by reduced levels of turbulence intensity away from the centerline.

Iso-surface evolution equation

This chapter is a direct continuation of the work described in Chapter 4, which examined the self-similar evolution of iso-surface area density, Σ, of a passive scalar field in a turbulent, temporal mixing layer for a wide range of iso-values. Here, the transport equation for Σ is considered in detail for the same turbulent flow and same iso-values of the passive scalar field. It was first demonstrated that the terms in the iso-surface area and the iso-surface area density transport equations could be esti-

mated accurately, such that the left- and right-hand sides of the transport equation were balanced. Next, the self-similar behavior of each of the five terms in the iso-surface area density equation (1.9) was examined in detail, and self-similar forms were proposed for each term based upon scaling arguments and the behavior of the data. Based on these self-similar forms, a scaling analysis of (1.9) suggests that, separately, terms $\mathcal{P}$ and $\mathcal{D}$, relating to the production and destruction of iso-surface area density, are significantly larger in magnitude than $\partial\Sigma/\partial t$. However, the net effect of the production and destruction, $K = \mathcal{P} - \mathcal{D}$, is the same order of magnitude as $\partial\Sigma/\partial t$. Finally, the self-similar transport of iso-surface area density in a temporal mixing layer was identified, and physical interpretations of each term is discussed in detail.

6.2 Conclusions and future directions

As discussed above, the present work is focused on gaining a deeper fundamental understanding of iso-surface transport in turbulent flows, in order to serve as a baseline comparison to future studies. As such, the problem setup considered here is the most 'simple' free shear flow with a passive scalar field. While the studies discussed herein do not contain some notable physical properties present in, e.g., turbulent combustion (effects of dilatation due to heat release or surface propagation due to a chemical source term), it is nonetheless useful in giving insight into how iso-surfaces grow and decay. Furthermore, the results may, in fact, be applicable to certain regimes of turbulent combustion such as the broken reactions zone (high Karlovitz number flames) where the effects of the dilatation rate are small [81, 101], as well as other mixing problems including the turbulent/non-turbulent interface or pollutants mixing in the atmosphere, among others.

There is potential for the present results to have significant implications on open questions in the current literature. For example, the 'flame bending' phenomenon, in which the flame surface area appears to have a square-root dependence on the turbulence intensity u' rather than the linear dependence predicted by theory [62],

has been receiving significant attention lately. Further research into the cause of the bending effect found that significant deviation from the linear trend occurs after a critical value of the Taylor Reynolds number, suggesting that the Taylor length scale may control surface behavior [30] (in contrast to the Kolmogorov scale, as previously predicted).

Similarly, a recent study by Kulkarni and Bisetti [47] examined the fractal scaling of a spherically expanding, premixed flame in homogeneous, isotropic turbulence. Contrary to the established understanding of fractal scaling by Sreenivasan *et al.*, the results of this study suggested that the surface area of the flame deviates from the expected fractal scaling when the surface features are on the order of the Taylor length scale (rather than the Kolmogorov scale). In combination with the above discussion on flame bending, and the scaling found for the iso-surface area density in Chapter 4, there is mounting evidence to suggest that the Taylor length scale has a significant effect on the iso-surface area density.

Furthermore, the proper scaling of iso-surface area in a turbulent flow is an open question in the literature. Based on the premixed flames discussed above, Kulkarni and Bisetti suggest that the surface area scales with the Taylor Reynolds number to the power of 1.11, or $Re_\lambda^{1.11}$ [47]. A study by Shete and de BruynKops of passive scalar iso-surfaces in homogeneous, isotropic turbulence found that the iso-surface area scales like the square root of the Taylor Reynolds number, $(Re_\lambda Sc)^{0.5}$ [83]. The present work, as discussed in Chapter 4, suggests that iso-surface area should scale with the square root of the turbulence Reynolds number, $(ReSc)^{0.5}$. Assuming that the flow is fully turbulent, this can be written in terms of the Taylor Reynolds number as $A/A_0 \sim (Re_\lambda Sc)$, which is similar to the result by Kulkarni and Bisetti. There does not yet appear to be a consensus in the literature, although as mentioned above, there is a trend towards identifying the Taylor length scale as a governing quantity of iso-surface behavior.

Future work

Future research efforts should obviously focus on increasing the complexity of the problem, whether that is by increasing the complexity of the flow geometry or by increasing the complexity of the physics, e.g., chemical reactions. However, care should be taken before undertaking the most complex problem possible; hopefully this dissertation has demonstrated that even the most 'simple' case contains significant nuance.

The first extension to the present work should be to examine a temporally developing jet with a passive scalar field. Although similar to the temporal mixing layer in many ways, the temporal jet features additional complications regarding the iso-surface area that will need to be addressed. In particular, consider a jet with scalar concentration $\Phi = 1$ issuing into an quiescent environment with $\Phi = 0$. As the jet mixes into the surrounding fluid, the centerline concentration will decrease, such that the iso-surface area associated with values of Φ_{iso} near $\Phi = 1$ will go to zero. In this case, it is unclear how $\partial\Sigma/\partial t$ and the relevant terms will scale; preliminary results suggest that the magnitude of $\partial\Sigma/\partial t$ could become comparable to the production and destruction terms, despite $ReSc \gg 1$ [8]. This creates an additional factor to include when considering the temporal development of iso-surface area density, without including any additional physics into the problem.

Future work should focus on including additional physics into the direct numerical simulations, which causes the number of terms retained in the iso-surface transport equation to increase. An obvious extension of this work will be to simulate more realistic examples of turbulent combustion by including chemical reactions and dilatation effects due to heat release. Other researchers have demonstrated that the scalar gradient tends to align with the most extensive strain-rate in the presence of heat release [16, 15, 55], as opposed to the most compressive strain-rate as shown above for a passive scalar. This effect may reverse or dampen the effect of iso-surface

production. Furthermore, the transport equation for the progress variable that characterizes premixed combustion includes a chemical source term, which will enter the iso-surface transport equation through the propagation velocity. Understanding the effect of the chemical source term on the propagation velocity will be an important part of understanding the evolution of the iso-surface curvature and its effects on the flame surface area.

Other problems that are particularly well-suited for this analysis are the surface of a non-premixed flame and the turbulent/non-turbulent interface. To the authors' knowledge, there have not been any recent studies that have used the iso-surface area density formulation to examine either of these cases, despite the clear applicability. These problems are particularly interesting from a physical standpoint; the non-premixed flame retains the complex physics associated with variable density from chemical heat release that is prominent in premixed flames, but the surface is passive, i.e., the propagation is entirely due to molecular diffusion. The turbulent/non-turbulent interface, on the other hand, is of particular interest because it is not a passive iso-surface. The propagation velocity of the turbulent/non-turbulent interface depends not only on molecular diffusion, but may also be influenced by the production and destruction of enstrophy in the flow [38, 105]. Clearly, these problems are well-suited to the methodology established in the present dissertation.

There are likely many more physical scenarios, described by an interface separating two regions of flow, that have not been addressed here. The hope is that this work can be utilized not only by those studying the problems explicitly discussed above (i.e., flame surface and the turbulent/non-turbulent interface), but also those studying other phenomena, from the formation of clouds in the atmosphere to the mixing of fresh and salt water in the ocean, or even the mixing of gases in a supernova explosion [27].

BIBLIOGRAPHY

[1] A. Almagro, M. García-Villalba, and O. Flores. A numerical study of a variable-density low-speed turbulent mixing layer. *J. Fluid Mech.*, 830:569–601, 2017.

[2] Wm. T. Ashurst, A. R. Kerstein, R.M. Kerr, and C. H. Gibson. Alignment of vorticity and scalar gradient with strain rate in simulated Navier–Stokes turbulence. *Phys. Fluids*, 30(8):2343–2353, 1987.

[3] G. Balamurugan, A. Rodda, J. Philip, and A. C. Mandal. Characteristics of the turbulent non-turbulent interface in a spatially evolving turbulent mixing layer. *J. Fluid Mech.*, 894, 2020.

[4] J. R. Baltzer and D. Livescu. Variable-density effects in incompressible non-buoyant shear-driven turbulent mixing layers. *J. Fluid Mech.*, 900, 2020.

[5] J. H. Bell and R. D. Mehta. Development of a two-stream mixing layer from tripped and untripped boundary layers. *AIAA journal*, 28(12):2034–2042, 1990.

[6] D. K. Bisset, J. C. R. Hunt, and M. M. Rogers. The turbulent/non-turbulent interface bounding a far wake. *J. Fluid Mech.*, 451:383–410, 2002.

[7] B. C. Blakeley, B. J. Olson, and J. J. Riley. Self-similarity of scalar iso-surface area density in a temporal mixing layer. *J. Fluid Mech.*, submitted, 2022.

[8] B. C. Blakeley, W. Wang, and J. J. Riley. On the kinematics of scalar iso-surfaces in decaying homogeneous, isotropic turbulence. *J. Turbul.*, 20(10):661–680, 2019.

[9] M. Boger, D. Veynante, H. Boughanem, and A. Trouvé. Direct numerical simulation analysis of flame surface density concept for large eddy simulation of turbulent premixed combustion. *Proc. Comb. Inst.*, 27(1):917–925, 1998.

[10] K. N. C. Bray, P. A. Libby, and J. B. Moss. Unified modeling approach for premixed turbulent combustion—Part I: General formulation. *Comb. Flame*, 61(1):87–102, 1985.

[11] S. Candel and T. Poinsot. Flame stretch and the balance equation for the flame area. *Combust. Sci. Technol.*, 70(1-3):1–15, 1990.

[12] C. Canuto, M. Y. Hussaini, A. Quarteroni, and T. A. Zang. *Spectral methods.* Springer, 2006.

[13] N. Chakraborty and R. S. Cant. Effects of strain rate and curvature on surface density function transport in turbulent premixed flames in the thin reaction zones regime. *Phys. Fluids*, 17(6):065108, 2005.

[14] N. Chakraborty and R. S. Cant. Turbulent Reynolds number dependence of flame surface density transport in the context of Reynolds averaged Navier–Stokes simulations. *Proc. Combust. Inst.*, 34(1):1347–1356, 2013.

[15] N. Chakraborty, M. Klein, and N. Swaminathan. Effects of Lewis number on the reactive scalar gradient alignment with local strain rate in turbulent premixed flames. *Proc. Combust. Inst.*, 32(1):1409–1417, 2009.

[16] N. Chakraborty and N. Swaminathan. Influence of the Damköhler number on turbulence-scalar interaction in premixed flames. I. Physical insight. *Phys. Fluids*, 19(4):045103, 2007.

[17] M. P. Clay, D. Buaria, P. K. Yeung, and T. Gotoh. Gpu acceleration of a petascale application for turbulent mixing at high schmidt number using OpenMP 4.5. *Computer Physics Communications*, 228:100–114, 2018.

[18] A. W. Cook. Artificial fluid properties for large-eddy simulation of compressible turbulent mixing. *Phys. Fluids*, 19(5):055103, 2007.

[19] A. W. Cook. Enthalpy diffusion in multicomponent flows. *Phys. Fluids*, 21(5):055109, 2009.

[20] A. W. Cook, W. Cabot, and P. L. Miller. The mixing transition in Rayleigh–Taylor instability. *J. Fluid Mech.*, 511:333–362, 2004.

[21] S. Corrsin. Investigation of flow in an axially symmetrical heated jet of air. *NACA Wartime Report W-94*, 1943.

[22] S. Corrsin and A. L. Kistler. Free–stream boundaries of turbulent flows. *NACA Technical Report 1244*, 1955.

[23] C. B. da Silva, J. C. R. Hunt, I. Eames, and J. Westerweel. Interfacial layers between regions of different turbulence intensity. *Annu. Rev. Fluid Mech.*, 46:567–590, 2014.

[24] C. B. da Silva and J. C. F. Pereira. Invariants of the velocity-gradient, rate-of-strain, and rate-of-rotation tensors across the turbulent/nonturbulent interface in jets. *Phys. Fluids*, 20(5):055101, 2008.

[25] S. M. de Bruyn Kops and J. J. Riley. Direct numerical simulation of laboratory experiments in isotropic turbulence. *Phys. Fluids*, 10(9):2125–2127, 1998.

[26] C. M. de Silva, J. Philip, K. Chauhan, C. Meneveau, and I. Marusic. Multiscale geometry and scaling of the turbulent-nonturbulent interface in high reynolds number boundary layers. *Physical review letters*, 111(4):044501, 2013.

[27] P. E. Dimotakis. Turbulent mixing. *Annu. Rev. Fluid Mech.*, 37:329–356, 2005.

[28] C. Dopazo, J. Martin, L. Cifuentes, and J. Hierro. Strain, rotation and curvature of non-material propagating iso-scalar surfaces in homogeneous turbulence. *Flow, Turbul. and Combust.*, 101(1):1–32, 2018.

[29] C. Dopazo, J. Martín, and J. Hierro. Local geometry of isoscalar surfaces. *Phys. Rev. E*, 76(5):056316, 2007.

[30] J. F. Driscoll, J. H. Chen, A. W. Skiba, C. D. Carter, E. R. Hawkes, and H. Wang. Premixed flames subjected to extreme turbulence: Some questions and recent answers. *Prog. Energy Combust. Sci.*, 76:100802, 2020.

[31] V. Eswaran and S. B. Pope. Direct numerical simulations of the turbulent mixing of a passive scalar. *Phys. Fluids*, 31(3):506–520, 1988.

[32] V. Eswaran and S. B. Pope. An examination of forcing in direct numerical simulations of turbulence. *Comput. Fluids*, 16(3):257–278, 1988.

[33] F. Fichot, B. Delhaye, D. Veynante, and S. M. Candel. Strain rate modelling for a flame surface density equation with application to non-premixed turbulent combustion. In *Proc. Combust. Inst.*, volume 25, pages 1273–1281. Elsevier, 1994.

[34] C. H. Gibson. Fine structure of scalar fields mixed by turbulence. I. Zero–gradient points and minimal gradient surfaces. *Phys. Fluids*, 11(11):2305–2315, 1968.

[35] S. Ha, J. Park, and D. You. A GPU-accelerated semi-implicit fractional-step method for numerical solutions of incompressible Navier–Stokes equations. *J. Comput. Phys.*, 352:246–264, 2018.

[36] I. Han and K. Y. Huh. Roles of displacement speed on evolution of flame surface density for different turbulent intensities and Lewis numbers in turbulent premixed combustion. *Combust. Flame*, 152(1-2):194–205, 2008.

[37] M. Holzner, A. Liberzon, N. Nikitin, B. Lüthi, W. Kinzelbach, and A. Tsinober. A Lagrangian investigation of the small-scale features of turbulent entrainment through particle tracking and direct numerical simulation. *J.Fluid Mech.*, 598:465–475, 2008.

[38] M. Holzner and B. Lüthi. Laminar superlayer at the turbulence boundary. *Phys. Rev. Lett.*, 106(13):134503, 2011.

[39] K. Y. Huh, J. Kwon, and D. Lee. Relationships for maximum flame surface density and brush thickness through conditional analysis in turbulent premixed combustion. *Phys. Fluids*, 25(7):075108, 2013.

[40] R. Jahanbakhshi and C. K. Madnia. Viscous superlayer in a reacting compressible turbulent mixing layer. *J. Fluid Mech.*, 848:743–755, 2018.

[41] Y. Kenmochi and R. Klette. Surface area estimation for digitized regular solids. *Vision Geometry IX*, 4117:100–111, 2000.

[42] C. A. Kennedy, M. H. Carpenter, and R. M. Lewis. Low-storage, explicit Runge–Kutta schemes for the compressible Navier–Stokes equations. *Appl. Numer. Math.*, 35(3):177–219, 2000.

[43] S. H. Kim and H. Pitsch. Scalar gradient and small-scale structure in turbulent premixed combustion. *Phys. Fluids*, 19(11):115104, 2007.

[44] M. Klein, A. Herbert, H. Kosaka, B. Böhm, A. Dreizler, N. Chakraborty, V. Papapostolou, H. G. Im, and J. Hasslberger. Evaluation of flame area based on detailed chemistry DNS of premixed turbulent hydrogen-air flames in different regimes of combustion. *Flow, Turbul. Combust.*, 104(2):403–419, 2020.

[45] W. Kollmann and J. H. Chen. Dynamics of the flame surface area in turbulent non-premixed combustion. In *Proc. Combust. Inst.*, volume 25, pages 1091–1098. Elsevier, 1994.

[46] T. Kulkarni and F. Bisetti. Evolution and scaling of the peak flame surface density in spherical turbulent premixed flames subjected to decaying isotropic turbulence. *Proc. Combust. Inst.*, 38(2):2817–2824, 2021.

[47] T. Kulkarni and F. Bisetti. Surface morphology and inner fractal cutoff scale of spherical turbulent premixed flames in decaying isotropic turbulence. *Proc. Combust. Inst.*, 38(2):2861–2868, 2021.

[48] T. Kulkarni, R. Buttay, M. H. Kasbaoui, A. Attili, and F. Bisetti. Reynolds number scaling of burning rates in spherical turbulent premixed flames. *J. Fluid Mech.*, 906, 2021.

[49] P. K. Kundu and I. M. Cohen. *Fluid mechanics*. Academic Press, 2002.

[50] Y. T. Lee and A. A. G. Requicha. Algorithms for computing the volume and other integral properties of solids. 1. Known methods and open issues. *Communications of the ACM*, 25(9):635–641, 1982.

[51] S. K. Lele. Compact finite difference schemes with spectral-like resolution. *J. Comput. Phys.*, 103(1):16–42, 1992.

[52] Y. S. Liu, J. Yi, H. Zhang, G. Q. Zheng, and J. C. Paul. Surface area estimation of digitized 3D objects using quasi-Monte Carlo methods. *Pattern Recognition*, 43(11):3900–3909, 2010.

[53] W. E. Lorensen and H. E. Cline. Marching cubes: A high resolution 3D surface construction algorithm. *ACM SIGGRAPH Computer Graphics*, 21(4):163–169, 1987.

[54] S. Luca, A. Attili, E. L. Schiavo, F. Creta, and F. Bisetti. On the statistics of flame stretch in turbulent premixed jet flames in the thin reaction zone regime at varying Reynolds number. *Proc. Combust. Inst.*, 37(2):2451–2459, 2019.

[55] S. P. Malkeson and N. Chakraborty. Alignment statistics of active and passive scalar gradients in turbulent stratified flames. *Phys. Rev. E*, 83(4):046308, 2011.

[56] F. E. Marble and J. E. Broadwell. The coherent flame model for turbulent chemical reactions. Technical report, DTIC Document, 1977.

[57] W. E. Mell, V. Nilsen, G. Kosály, and J. J. Riley. Investigation of closure models for nonpremixed turbulent reacting flows. *Phys. Fluids*, 6(3):1331–1356, 1994.

[58] O. Mesnard and L. A. Barba. Three-dimensional flow simulation of the flying snake using Microsoft Azure. The 30th International Conference on Parallel Computational Fluid Dynamics, 2018.

[59] D. Mistry, J. Philip, J. R. Dawson, and I. Marusic. Entrainment at multi-scales across the turbulent/non-turbulent interface in an axisymmetric jet. *J. Fluid Mech.*, 802:690–725, 2016.

[60] M. M. Neamtu-Halic, D. Krug, J. P. Mollicone, M. Van Reeuwijk, G. Haller, and M. Holzner. Connecting the time evolution of the turbulence interface to coherent structures. *J. Fluid Mech.*, 898, 2020.

[61] T. S. Newman and H. Yi. A survey of the marching cubes algorithm. *Computers & Graphics*, 30(5):854–879, 2006.

[62] G. Nivarti and S. Cant. Direct numerical simulation of the bending effect in turbulent premixed flames. *Proc. Combust. Inst.*, 36(2):1903–1910, 2017.

[63] B. J. Olson, J. Larsson, S. K. Lele, and A. W. Cook. Nonlinear effects in the combined Rayleigh-Taylor/Kelvin-Helmholtz instability. *Phys. Fluids*, 23(11):114107, 2011.

[64] P. O'Neill and J. Soria. The relationship between the topological structures in turbulent flow and the distribution of a passive scalar with an imposed mean gradient. *Fluid dynamics research*, 36(3):107, 2005.

[65] C. Pantano and S. Sarkar. A study of compressibility effects in the high-speed turbulent shear layer using direct simulation. *J. Fluid Mech.*, 451:329–371, 2002.

[66] J. Patera and V. Skala. A comparison of fundamental methods for iso-surface extraction. *Mach. Graph. Vis.*, 13(4):329–344, 2004.

[67] G. S. Patterson and S. A. Orszag. Spectral calculations of isotropic turbulence: Efficient removal of aliasing interactions. *Phys. Fluids*, 14(11):2538–2541, 1971.

[68] F. E. H. Pérez, N. Mukhadiyev, X. Xu, A. Sow, B. J. Lee, R. Sankaran, and H. G. Im. Direct numerical simulations of reacting flows with detailed chemistry using many-core/GPU acceleration. *Comput. & Fluids*, 173:73–79, 2018.

[69] B. Perfect, N. Kumar, and J. J. Riley. Vortex structures in the wake of an idealized seamount in rotating, stratified flow. *Geophys. Res. Lett.*, 45(17):9098–9105, 2018.

[70] N. Peters. Laminar flamelet concepts in turbulent combustion. *Proc. Combust. Inst.*, 21(1):1231–1250, 1988.

[71] T. Poinsot and D. Veynante. *Theoretical and numerical combustion*. RT Edwards, Inc., 2005.

[72] S. B. Pope. The evolution of surfaces in turbulence. *International Journal of Engineering Science*, 26(5):445–469, 1988.

[73] S. B. Pope. Computations of turbulent combustion: progress and challenges. *Proc. Combust. Inst.*, 23(1):591–612, 1991.

[74] S. B. Pope. *Turbulent flows*. Cambridge university press, 2000.

[75] R. R. Prasad and K. R. Sreenivasan. Scalar interfaces in digital images of turbulent flows. *Experiments in fluids*, 7(4):259–264, 1989.

[76] R. R. Prasad and K. R. Sreenivasan. Quantitative three-dimensional imaging and the structure of passive scalar fields in fully turbulent flows. *J. Fluid Mech.*, 216:1–34, 1990.

[77] B.A. Remington, L. J. Atherton, L. R. Benedetti, L. Berzak-Hopkins, D. K. Bradley, D. A. Callahan, D. T. Casey, P.M. Celliers, C. J. Cerjan, D. S. Clark, et al. Hydrodynamic instabilities and mix studies on nif: predictions, observations, and a path forward. In *J. Phys.: Conference Series*, volume 688, page 012090. IOP Publishing, 2016.

[78] H. L. Resnikoff and O. Raymond Jr. *Wavelet Analysis*. Springer, New York, NY, 1998.

[79] M. M. Rogers and R. D. Moser. Direct simulation of a self-similar turbulent mixing layer. *Phys. Fluids*, 6(2):903–923, 1994.

[80] R. Sankaran, E. R. Hawkes, C. S. Yoo, and J. H. Chen. Response of flame thickness and propagation speed under intense turbulence in spatially developing lean premixed methane–air jet flames. *Combust. Flame*, 162(9):3294–3306, 2015.

[81] B. Savard and G. Blanquart. Broken reaction zone and differential diffusion effects in high Karlovitz n-C_7H_{16} premixed turbulent flames. *Combust. Flame*, 162(5):2020–2033, 2015.

[82] J. Schumacher and K. R. Sreenivasan. Statistics and geometry of passive scalars in turbulence. *Phys. Fluids*, 17(12):125107, 2005.

[83] K. P. Shete and S. M. de Bruyn Kops. Area of scalar isosurfaces in homogeneous isotropic turbulence as a function of Reynolds and Schmidt numbers. *J. Fluid Mech.*, 883, 2020.

[84] T. S. Silva, M. Zecchetto, and C. B. da Silva. The scaling of the turbulent/non-turbulent interface at high Reynolds numbers. *J. Fluid Mech.*, 843:156–179, 2018.

[85] A. W. Skiba, T. M. Wabel, C. D. Carter, S. D. Hammack, J. E. Temme, and J. F. Driscoll. Premixed flames subjected to extreme levels of turbulence Part I: Flame structure and a new measured regime diagram. *Combust. Flame*, 189:407–432, 2018.

[86] K. R. Sreenivasan and C. Meneveau. The fractal facets of turbulence. *J. Fluid Mech.*, 173:357–386, 1986.

[87] K. R. Sreenivasan, R. Ramshankar, and C. Meneveau. Mixing, entrainment and fractal dimensions of surfaces in turbulent flows. *Proc. R. Soc. of Lond.*, 421(1860):79–108, 1989.

[88] D. Storti. Using lattice data to compute surface integral properties of digitized objects. *Proc. IDMME*, 2010.

[89] R. R. Taveira and C. B. da Silva. Characteristics of the viscous superlayer in shear free turbulence and in planar turbulent jets. *Phys.Fluids*, 26(2):021702, 2014.

[90] H. Tennekes and J. L. Lumley. *A first course in turbulence*. MIT press, 1972.

[91] V. K. Tritschler, B. J. Olson, S. K. Lele, S. Hickel, X. Hu, and N. A. Adams. On the Richtmyer–Meshkov instability evolving from a deterministic multimode planar interface. *J. Fluid Mech.*, 755:429–462, 2014.

[92] A. Trouvé. The production of premixed flame surface area in turbulent shear flow. *Combust. Flame*, 99(3-4):687–696, 1994.

[93] A. Trouvé and T. Poinsot. The evolution equation for the flame surface density in turbulent premixed combustion. *J. Fluid Mech.*, 278:1–31, 1994.

[94] E. van Kalmthout and D. Veynante. Direct numerical simulations analysis of flame surface density models for nonpremixed turbulent combustion. *Phys. Fluids*, 10(9):2347–2368, 1998.

[95] E. van Kalmthout, D. Veynante, and S. Candel. Direct numerical simulation analysis of flame surface density equation in non-premixed turbulent combustion. *Proc. Comb. Inst.*, 26(1):35–42, 1996.

[96] M. van Reeuwijk and M. Holzner. The turbulence boundary of a temporal jet. *J.Fluid Mech.*, 739:254–275, 2014.

[97] L. Vervisch, E. Bidaux, K. N. C. Bray, and W. Kollmann. Surface density function in premixed turbulent combustion modeling, similarities between probability density function and flame surface approaches. *Phys. Fluids*, 7(10):2496–2503, 1995.

[98] L. Vervisch and T. Poinsot. Direct numerical simulation of non-premixed turbulent flames. *Ann. Rev. Fluid Mech.*, 30(1):655–691, 1998.

[99] D. Veynante, A. Trouvé, K. N. C. Bray, and T. Mantel. Gradient and countergradient scalar transport in turbulent premixed flames. *J. Fluid Mech.*, 332:263–293, 1997.

[100] E. Villermaux and C. Innocenti. On the geometry of turbulent mixing. *J. Fluid Mech.*, 393:123–147, 1999.

[101] Daniel H Wacks, Nilanjan Chakraborty, Markus Klein, Paul G Arias, and Hong G Im. Flow topologies in different regimes of premixed turbulent combustion: A direct numerical simulation analysis. *Phys. Rev. Fluids*, 1(8):083401, 2016.

[102] H. Wang, E. R. Hawkes, J. H. Chen, B. Zhou, Z. Li, and M. Aldén. Direct numerical simulations of a high Karlovitz number laboratory premixed jet flame–an analysis of flame stretch and flame thickening. *J. Fluid Mech.*, 815:511–536, 2017.

[103] W. Wang. *Kinematic study of the evolution and properties of flame surfaces in turbulent nonpremixed combustion with local extinction and reignition.* PhD thesis, University of Washington, 2013.

[104] T. Watanabe, J. J. Riley, S. M. de Bruyn Kops, P. J. Diamessis, and Q. Zhou. Turbulent/non-turbulent interfaces in wakes in stably stratified fluids. *J. Fluid Mech.*, 797, 2016.

[105] T. Watanabe, Y. Sakai, K. Nagata, Y. Ito, and T. Hayase. Reactive scalar field near the turbulent/non-turbulent interface in a planar jet with a second-order chemical reaction. *Phys. Fluids*, 26(10):105111, 2014.

[106] J. Westerweel, C. Fukushima, J. M. Pedersen, and J. C. R. Hunt. Momentum and scalar transport at the turbulent/non-turbulent interface of a jet. *J. Fluid Mech.*, 631:199–230, 2009.

[107] M. Wolf, B. Lüthi, M. Holzner, D. Krug, W. Kinzelbach, and A. Tsinober. Investigations on the local entrainment velocity in a turbulent jet. *Phys. Fluids*, 24(10):105110, 2012.

[108] P. K. Yeung, S. S. Girimaji, and S. B. Pope. Straining and scalar dissipation on material surfaces in turbulence: implications for flamelets. *Combust. Flame*, 79(3-4):340–365, 1990.

[109] M. Yurtoglu, M. Carton, and D. Storti. Treat all integrals as volume integrals: A unified, parallel, grid-based method for evaluation of volume, surface, and path integrals on implicitly defined domains. *J. Comput. Inf. Sci. Eng.*, 18(2):021013, 2018.

[110] F. Zames. Surface area and the cylinder area paradox. *The Two-Year College Mathematics Journal*, 8(4):207–211, 1977.

[111] P. Zaspel and M. Griebel. Massively parallel fluid simulations on Amazon's HPC cloud. In *First International Symposium on Network Cloud Computing and Applications*, pages 73–78. IEEE, 2011.

[112] X. Zhang, T. Watanabe, and K. Nagata. Turbulent/nonturbulent interfaces in high-resolution direct numerical simulation of temporally evolving compressible turbulent boundary layers. *Phys. Rev. Fluids*, 3(9):094605, 2018.

[113] X. Zhu, E. Phillips, V. Spandan, J. Donners, G. Ruetsch, J. Romero, R. Ostilla-Mónico, Y. Yang, D. Lohse, R. Verzicco, et al. AFiD–GPU: a versatile Navier–Stokes solver for wall-bounded turbulent flows on GPU clusters. *Computer physics communications*, 229:199–210, 2018.

Appendix A

COMPUTING ISO-SURFACE INTEGRALS

Computing the area of an implicitly defined iso-surface is a challenging problem that has been addressed by numerous researchers over many years. The most common methodology for estimating iso-surface area is to apply algorithms, e.g., marching cubes [53], which identify the location of the surface and then use patches (commonly triangular) to recreate the surface. While generally effective, these methods are not guaranteed to converge to the true area [110, 41], and can be computationally burdensome [61]. Another method of computing iso-surface area is a stochastic Monte Carlo method using surface crossing, as demonstrated by [52] and [83]. While these methods are able to achieve extremely accurate answers, they are often slow to converge and require extensive computing resources.

An alternative algorithm for computing iso-surface area of implicitly defined surfaces on a discretized domain was proposed by [88] and detailed by [109], which is utilized to compute iso-surface areas in this study. In brief, the algorithm computes surface integrals as a sum of contributions from a stencil computation applied to the discrete data set without requiring interpolation to, or reconstruction of, the surface. This method can also be shown to converge to the true surface area based on a wavelet analysis, provided the implicit surface is continuous [78]. Not only does this provide an accurate estimation of the surface area, the derivatives can be calculated efficiently on highly parallel systems using standard finite-difference techniques. A brief discussion will be included here; for further details regarding implementation and convergence, readers are encouraged to consult [109].

To compute the area of an implicit iso-surface, the occupancy function, X, is

defined as

$$X(\Phi) = \begin{cases} 1, & \Phi - \Phi_{\text{iso}} \leq 0 \\ 0, & \Phi - \Phi_{\text{iso}} > 0 \end{cases} . \tag{A.1}$$

From the divergence theorem and properties of the surface normal vector defined in (1.2), the surface integral of the quantity Q over the boundary $\partial\Omega$ defined by $\Phi = \Phi_{\text{iso}}$ can be converted to an integral over the volume contained in bounding box $\mathcal{V}$ [88],

$$\int_{\partial\Omega} Q d\text{s} = -\int_{\mathcal{V}} \frac{Q}{|\nabla\Phi|} \frac{\partial X}{\partial x_i} \frac{\partial \Phi}{\partial x_i} d\text{v}, \tag{A.2}$$

where ds and dv are surface and volume elements, respectively. Note that for $Q = 1$, this quantity reduces to the iso-surface area A_{iso}, but any fluid quantity Q can be integrated over the surface using the above expression. Discretizing (A.2) yields the following expression for A_{iso},

$$A_{\text{iso}} = -\sum_{i,j,k} \frac{\nabla X_{i,j,k} \cdot \nabla \Phi_{i,j,k}}{\sqrt{\nabla\Phi_{i,j,k} \cdot \nabla\Phi_{i,j,k}}} \Delta x \Delta y \Delta z, \tag{A.3}$$

where i, j, k represent indices of the discretized domain and the gradients are evaluated numerically using Daubechies wavelet connection coefficients at each grid point (which coincide with second- and fourth-order central finite difference coefficients for genus 1 and 2 wavelets). Because the area computations require only stencil computations, the calculations are highly parallelizable and efficient for large, distributed domains.

Another reason to employ this particular algorithm is due to its similarity to the definition of iso-surface area density. For an arbitrary bounding volume $\mathcal{V}$ and letting $Q = 1$, the integrands of (2.41) and (A.2) can be equated, such that

$$|\nabla\Phi|\delta(\Phi - \Phi_{\text{iso}}) = -\frac{1}{|\nabla\Phi|} \frac{\partial X}{\partial x_i} \frac{\partial \Phi}{\partial x_i}. \tag{A.4}$$

The relationship between the definitions becomes apparent by noting that the characteristic occupancy function, X, can be re-written in terms of the Heaviside function, H, such that $X(\Phi) = H[-(\Phi - \Phi_{\text{iso}})]$. Using the chain rule and the properties of the

delta function [74], it can be shown that

$$\frac{\partial X(\Phi)}{\partial x_i} = \frac{\partial}{\partial \Phi}\Big(H[-(\Phi - \Phi_{\text{iso}})]\Big)\frac{\partial \Phi}{\partial x_i} = -\delta(\Phi - \Phi_{\text{iso}})\frac{\partial \Phi}{\partial x_i}. \tag{A.5}$$

Substituting this result for $\partial X/\partial x_i$ into (A.4) above, it can be established that the algorithm from [88] and [109] is consistent with the formal definition of iso-surface area density as discussed by [73], [93] and [97].